

Alma Mater Studiorum · Università di Bologna

**Scuola di Scienze
Corso di Laurea Magistrale in Fisica**

Magnesium based nanoparticles for hydrogen storage

Relatore:

Dott. Luca Pasquini

Presentata da:

Federico D'Amico

Sessione II

Anno Accademico 2013/2014

Contents

Abstract	6
CHAPTER I. Hydrogen economy: perspectives and problems	7
An alarming situation	7
A new hope: hydrogen	8
How to store hydrogen: different paths	10
Lolland: the future has become reality	12
CHAPTER II. Hydrogen and metals	13
Introduction	13
Phase diagrams	13
Solid solution at low hydrogen concentration	14
Solid solution at high hydrogen concentration	16
Hydrides structure	18
Hydride formation thermodynamics	19
Terminal solubility	22
Destabilization of Mg-H system	23
CHAPTER III. Hydrogen	29
General features	29
Hydrogen molecule according to quantum mechanics	31
CHAPTER IV. Materials	35
Magnesium	35
Magnesium oxide	36
Palladium	38
CHAPTER V. Inert Gas Condensation	41
General features	41
Experimental setup	41
CHAPTER VI. Nucleation theories	45
Classical nucleation theory	45
Beyond classical theory	46
Kinetic nucleation theory	47
Coalescence	48
CHAPTER VII. Devices used	51
SEM	51

History	51
General features	51
Experimental setup	54
TEM	54
History	54
General features	55
Experimental setup	57
XRD	57
History	57
General features	58
Experimental setup	62
CHAPTER VIII. Samples morphologic characterization	63
From pure Mg nanoparticles to Mg/MgO systems	63
MgO_87	63
MgO_88	66
MgO_Pd_89	68
MgOPd_98	69
MgO_95	71
MgO_Pd_97	73
XRD analysis	76
MgO_95	77
MgO_93	78
TEM analysis	79
CHAPTER IX. Samples subjected to hydrogenography	84
MgPd_51	84
MgPd_101	84
MgOPd_99	85
MgOPd_100	86
CHAPTER X. Hydrogenography	87
General features	87
Substrate presence effects	88
Hysteresis phenomenon	89
Experimental setup	90
Results	92

MgOPd_99 2 minutes.....	92
MgOPd_99 5 minutes.....	94
MgPd_101 2 minutes	95
MgPd_101 1 minute.....	100
MgOPd_100 2 minutes.....	103
MgOPd_100 1 minute	106
MgPd_51	109
CHAPTER XI. Conclusions	114
References	120
Acknowledgments	123

Abstract

Questo lavoro riguarda la sintesi e caratterizzazione di nanoparticelle basate sul magnesio per l'immagazzinamento di idrogeno. Le nanoparticelle sono state cresciute mediante Inert Gas Condensation, una tecnica aerosol in cui il materiale viene sublimato e diretto verso i substrati tramite un flusso di gas inerte, e caratterizzate attraverso microscopia elettronica e diffrazione di raggi X. Queste operazioni sono state eseguite presso il Dipartimento di Fisica e Astronomia dell'Università di Bologna. Sono stati sintetizzati due tipi di particelle: nel primo il magnesio viene depositato direttamente sul substrato, nel secondo esso incontra un flusso di ossigeno prima di depositarsi sulla superficie. In questo modo si formano delle particelle con struttura core-shell in cui la parte interna è formata da magnesio e quella esterna dal suo ossido. La presenza di una shell consistente dovrebbe permettere, secondo il modello di deformazioni elastiche, di diminuire il valore assoluto dell'entropia di formazione dell'idruro di magnesio, condizione necessaria affinché il desorbimento di idrogeno possa avvenire in maniera più agevole rispetto a quanto non accada col materiale bulk. Tutti i campioni sono stati ricoperti di palladio, il quale favorisce la dissociazione della molecola di idrogeno. La capacità di assorbimento dell'idrogeno da parte dei campioni è stata studiata mediante idrogenografia, una tecnica ottica recentemente sviluppata in cui la quantità di gas assorbita dal materiale è legata alla variazione di trasmittanza ottica dello stesso. Le misure sono state eseguite presso l'Università Tecnica di Delft. I risultati ottenuti evidenziano che le nanoparticelle di solo magnesio mostrano dei chiari plateau di pressione corrispondenti all'assorbimento di idrogeno, tramite cui sono stati stimati i valori di entalpia di formazione. Al contrario, i campioni con struttura core-shell, la cui crescita rappresenta di per sé un risultato interessante, non presentano tale comportamento.

CHAPTER I. Hydrogen economy: perspectives and problems.

An alarming situation

The need for more and more energy and the dramatic necessity of respecting Earth environmental limits force mankind to find new or improve clean and renewable sources of energy.

According to US Energy Information Administration [1] in 2010 just 5,3% of the whole energy production came from clean sources and global power requirement was of about 17000 TW h per year, but experts say that it will grow up to 28000 TW h per year in 2030, especially due to the economic growth of the so called BRICS (Figures 1-1 and 1-2).

The conversion from British Thermal Units and kWh is that 1 Btu stands for 0.000293 kWh.

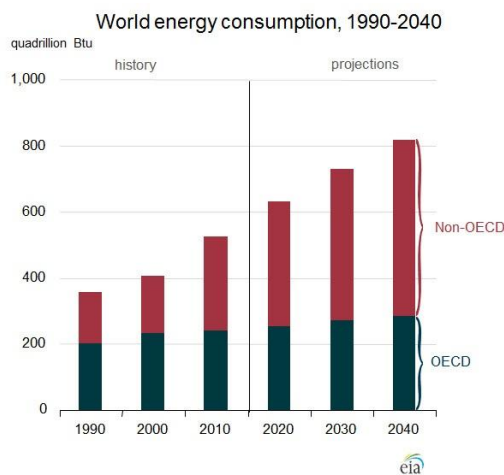


Figure 1-1

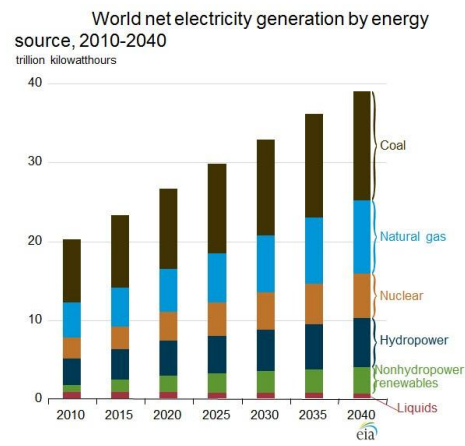


Figure 1-2

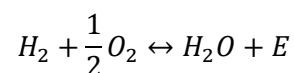
Today's situation is alarming since most of the exploited energy comes from hydrocarbon resources: a solution that creates geopolitical tensions, a degree of pollution so critical that if we do not change our energy supplying system climate changes will cancel out mankind soon and that is forced to end, since it takes million of years to create new fossil deposits.

Being the situation so dangerous, the birth and the affirmation of an economically sustainable system based upon renewable sources appears a priority.

A new hope: hydrogen

Hydrogen was thought to be a fuel that could substitute gasoline for the first time in the Seventies. In 1970, during a talk at General Motors Technical Centre, J. Bockris launched the idea of a hydrogen economy [2]: a system where this gas should have replaced petroleum derivatives as fuel. Actually, this simple change would not solve the environmental problem: hydrogen does not occur naturally in quantity, but it must be generated and the way this is done is a central point of the discussion.

Proponents of a world-scale hydrogen economy affirm that this solution would be cleaner, particularly in transport applications, being free from the release of pollutants. Moreover, a significant reduction in carbon dioxide emissions would be possible if carbon capture methods were utilized at the site of hydrogen production. In fact, hydrogen is just a carrier of energy. The simplest way to store and release energy is through the following reaction:



It takes place in fuel cells (Figure 1-3), systems with very high values of efficiency (till 80%-85% for devices that are able to use heat produced by the reaction, without this skill efficiency drops to about 60%-70%) and produces just water. When working at very high temperatures some polluting gasses could be released, but this inconvenient can be eliminated by specific methods.

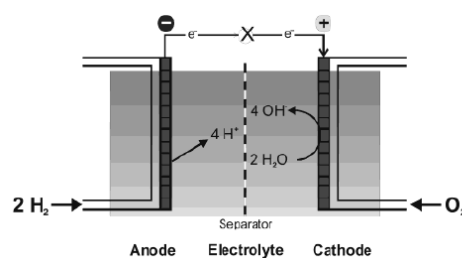


Figure 1-3

Nowadays molecular hydrogen is mainly created from fossil sources [3] and so carbon dioxide is produced: 48% from natural gas, 30% from oil and 18% from coal. Just the 4% comes from electrolysis of water, a method that can be CO₂ free. Decomposing water, since most hydrogen on Earth is bonded to oxygen in H₂O, requires an external (electrical or heat) input and it would be positive if it came from clean source such as solar energy.

Hydrogen production is a large and growing industry with rates of growth of around 10% per year [4]. Two are the primary uses of hydrogen: the synthesis of ammonia, that is widely diffused in fertilizers, and the so called hydrocracking, that is a process converting heavy petroleum sources into lighter fractions.

Hydrogen is industrially produced from steam reforming, which uses fossil fuels such as natural gas, oil or coal: greenhouse gasses are so generated. The most widely diffused method is named Kvaerner process, from the Norwegian company that developed it in the 1980s [5]. It is also possible to use biological agents to create hydrogen, like algae or some bacteria: the former, if deprived of sulphur, creates hydrogen instead of oxygen through the normal photosynthesis, the latter extract it from hydrocarbons, together with CO₂.

The process by which molecular hydrogen is split from water is named electrolysis and it has been found that it can be developed by aquatic plants too. These systems are not widely diffused due to their low efficiencies.

Current best processes have an efficiency that varies from 50% to 80% [6]: 1 kg of hydrogen requires 50 to 79 kWh of electricity that means about 3 €/kg, which is 3 up to 10 times the cost of hydrogen made from steam reformation of natural gas. Electrolysis can become cheaper using systems working at high pressure or at high temperature.

Using electricity produced by photovoltaic systems represents the cleanest way to produce hydrogen: water is broken into hydrogen and oxygen by a photoelectrochemical cell (PEC) process which is called artificial photosynthesis. In 1983 direct water splitting was demonstrated with a low cost thin film of amorphous silicon multi-junction sheet immersed in water itself [7]. This pathway is very interesting and research goes on developing higher and higher efficiency multi-junction cell technology.

Sun energy can be exploited in another way too. It was said that high temperatures are required to split hydrogen from water: it can be done exploiting concentrating solar plants, capable to heat water up to 1200°C.

Production is just the first step toward a hydrogen economy: storing the gas is a critical point and will be the core of this work.

In 2009 the US Department of Energy set the performances that any hydrogen storage system should have in order to develop an economically sustainable fuel distribution. Data are shown in Table 1 [2].

Table 1

	Unit	2010	2015	Final
Gravimetric capacity	wt%	4.5	5.5	7.5
	kWh/kg	1.5	1.8	2.5
Volumetric capacity	kg/m ³	28	40	70
	kWh/m ³	900	1300	2300

Minimal/maximal working temperature	°C	-30/50	-40/60	-40/60
Purity	% (dry)	99.97	99.97	99.97
Supply time (for 5 kg of hydrogen)	minutes	4.2	3.3	2.5

How to store hydrogen: different paths

Nowadays there are several methods pointed as solution to this problem, each of one exploiting different physical phenomena:

- Physical containment;
- Physical adsorption;
- Chemical bound.

Molecular hydrogen has very high energy density on mass basis, but at ambient conditions it has very low energy density by volume, so the first solution tries to improve this ratio by pressurization or liquefaction. Achieving high pressures needs a great use of external energy for the compression. Liquid hydrogen is formed cooling the gas down to 20.28 K. Cryogenic storage requires large energies and very complex technologies and presents the problem of the boil off. Moreover, ice may develop in the device used to contain hydrogen, corroding it.

The second approach is to absorb molecular hydrogen on the surface of a solid storage material, without hydrogen dissociation. In this way, the system does not suffer from limitations of gas kinetics. The very central problem of this solution is the low quantity of hydrogen stored and the low temperature. In order to improve physisorption, materials should have a good density of H₂ per surface unit and a large active surface. The best candidates to develop this approach are Metal Organic Frameworks (Figure 1-4), activated carbon, hydrogen clathrate hydrate (Figure 1-5) and nanostructured carbons (Figure 1-6 shows graphite nanotubes) [8].

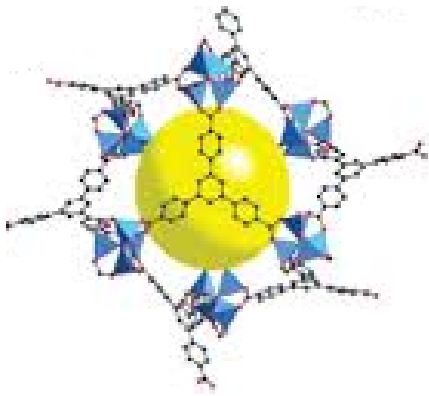


Figure 1-4

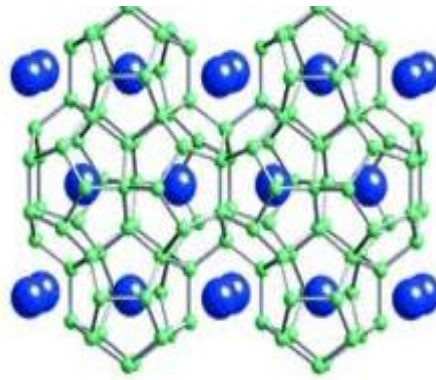


Figure 1-5

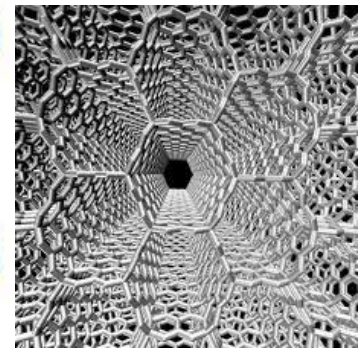


Figure 1-6

The last one is what will be investigated in this work: hydrogen stored as a chemical hydride in some compounds. This solution is thought to be efficient for matters as safety, easiness of transport and mass and volume density problems. Storing and ejecting H_2 molecules can be controlled by kinetics and heat control. Current barriers to practical and spread use are the values of pressure and temperature that must be reached in order to release or accumulate hydrogen, even if several compounds able to satisfy the US Department of Energy objectives are already known. Research goals are to lower pressure and temperature needed, make reactions faster and better volume and energy densities, keeping attention on costs.

A large scale hydrogen economy cannot become reality without an efficient infrastructure system. It would be made up of pipelines and filling stations. If these are far from the pipeline network, they must be supplied by trucks which carry hydrogen (liquid, compressed or stored in hydrides). Since hydrogen corrodes steel, pipelines must be covered internally by special coatings that are already known. Even if they are expensive and still not competitive with petroleum or natural gas networks, pipelines represent the cheapest way to make hydrogen move from a point to another.

Pipelines are essential in a scheme that expects a few hydrogen producing plants, but they could be in principle much less important if small and diffuse producing sites were adopted. In any case, it is reasonable that both approaches would be adopted, if hydrogen took the place of gasoline: centralized primary energy plants would have higher hydrogen production efficiency but they would require long range transportation networks, with the linked problems of hydrogen damage to and leak from the lines of distribution. On the contrary, small local plants would have lower production efficiency, but the reduced use of pipelines could result in a more efficient scheme in terms of primary energy used.

Hydrogen has one of the widest explosive and ignition mix range with air of all the gasses, so safety is a central concern. Whatever the mix between air and hydrogen, an explosion is very probable. Moreover,

pure hydrogen-oxygen flames burn in the region of the ultraviolet, so a flame detector is necessary and hydrogen is also odourless, a feature that makes harder the gas detection. The European Commission launched the first higher educational program in hydrogen safety engineering at the University of Ulster.

Lolland: the future has become reality

European Union is cutting edge about hydrogen economy: Lolland Hydrogen Community is the first full-scale Hydrogen Community Demonstration facility for residential Fuel Cell Combined Heat and Power (CHP) [9]. Lolland is an island in Denmark where wind is abundant. This factor makes possible a large production of energy from wind mills, so copious that more than the 50% of the energy produced is in excess. For this reason it is stored in the form of hydrogen and used for residential and industrial facilities. Hydrogen is produced by electrolysis of water together with oxygen. The oxygen is used in the municipal water treatment plant nearby to speed up the biological process. Hydrogen is stored in low-pressure storage tanks at six bars and fuels two PEM Fuel Cell Micro Combined Heat and Power (CHP) stations.

CHAPTER II. Hydrogen and metals

Introduction

Hydrogen is a very reactive molecule and it forms a wide range of different chemical bonds. It is possible to classify different compounds from the kind of interaction with hydrogen:

- Saline hydrides: they are made up of hydrogen and alkali and alkali-earth elements, having low values of electronegativity, so that hydrogen forms ionic compounds (LiH, NaH, MgH₂, BeH₂, etc.);
- Hydrogen-bonded molecular crystals: hydrogen reacts with atoms or radicals with high electronegativity values (2,5-dihydroxybenzoquinone (DpH), 2,5-dichloro-3,6-dihydroxybenzoquinone (DpC1), etc.);
- Covalent molecules and crystals: they are formed by hydrogen and an element that has got a similar electronegativity value (CH₄, NH₃, SiH₄, HF, etc.);
- Metallic hydrides: they are made up of hydrogen interstitial atoms in transition metals, lanthanides and actinides (NiH_x, VH, VH₂, CrH, CeH₂, etc.).

Note that heavy simple metals do not form any kind of compound with hydrogen. Moreover, metallic hydrides exist over large ranges of non-stoichiometric compositions, since hydrogen occupies interstitial sites and the quantity of gas included into the metal changes as the thermodynamic conditions do. In many cases the host material changes its structure in order to accommodate hydrogen.

Phase diagrams

Phase diagrams are a very useful instrument to study binary systems, such as those in which H atoms bond with M (metallic) ones. It is useful to define the variable x as the ratio of H concentration over the one of M. In other words:

$$C = \frac{[H]}{[M]}$$

When T is on the abscissa, it is possible to speak of TC diagrams. Changes in temperature involve changes in the thermodynamic equilibrium between the sample and the surrounding atmosphere. For this reason, to draw correct phase diagrams, it is more useful to study PC phase diagrams at different temperatures, kept constant during a measurement. The result is the so called pressure-concentration-isotherms (PCI) in which the phase boundary is determined by the inflection points of the diagram.

At each temperature under some critical one there is a plateau between the two inflection points. It means that two different phases coexist at the same time. Sometimes it is possible to observe a hysteresis, during a heating-cooling cycle. In this case, desorption branches are commonly taken as representative of the equilibrium condition. Moreover, it is only over some specific temperatures that the hydrogen diffusion process through the bulk is activated: it is a common practice to make the sample undergo heating-cooling cycles, in order to make it permeable.

Figure 2-1 shows a *TC* diagram (system of H and Pd) and Figure 2-2 a *PCI* one at different temperatures (D and Pd).

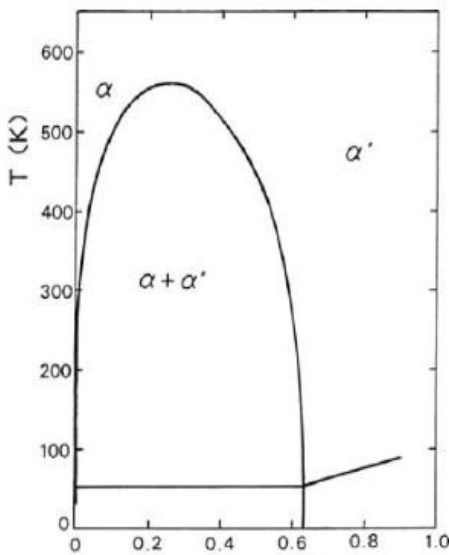


Figure 2-1

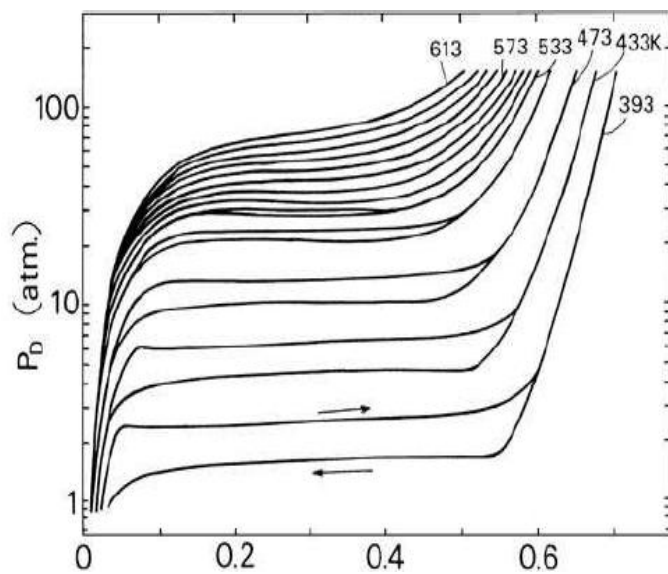


Figure 2-2

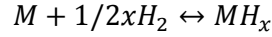
Solid solution at low hydrogen concentration

At low hydrogen concentrations, all *PCI* have a common slope, proportional to the pressure square root. This relation is known as Sievert's law and it can be explained intuitively considering that hydrogen molecules are dissociated into two atoms entering the host metal. Hydrogen solubility is a thermally activated phenomenon, so the expression for the solubility is

$$C = \sqrt{\frac{p}{p_0}} * e^{\Delta S_s/k} e^{-\Delta H_s/kT}$$

Where ΔS_s is the entropy of solution referred to T and p_0 and ΔH_s the enthalpy of solution and stands for the change of entropy or enthalpy of hydrogen when it enters the host material.

When thermodynamic equilibrium is achieved, the further expression stands:



Calling μ^g the chemical potential of the gas phase and μ^α the one in the solid phase, it is equivalent to say

$$\frac{1}{2}\mu^g = \mu^\alpha$$

For solid solution containing n hydrogen atoms, it is possible to distinguish the configurational (labelled by c) and non-configurational (nc) terms of the Gibbs free energy:

$$G^\alpha = G^{nc} + G^c = H^\alpha - TS^c - TS^{nc} = H^\alpha - TS^{nc} - Tk * \ln \frac{N!}{n!(N-n)!}$$

It is easy to derive the chemical potential, once defined $r=N/N_0$ as the number of interstitial sites per metallic atom (h and s stand for enthalpy and entropy per atom):

$$\mu^\alpha = \frac{\delta G}{\delta n} = h^\alpha - Ts^{nc} + kT * \ln \frac{C}{r-C}$$

Writing for $C \ll r$, that is the regime considered, the following expressions take place

$$\Delta h_s = h^\alpha - \frac{1}{2}h^g$$

$$\Delta S_s = s^{nc} + k * \ln r - \frac{1}{2}s^g$$

$$\Delta H_s - T\Delta S_s = \mu^{nc} - \frac{1}{2}\mu^{g0} - kT \ln r$$

One can think that in this way it is possible to derive entropy and enthalpy by an Arrhenius plot of $R \ln (P_{eq}/P_0)$ versus $1/T$, but the intercept is not ΔH_s and ΔS_s is not represented by the slope of the linear relation, because, if it stands, it is impossible to distinguish both the contributes. For this reason, it is necessary to determine the variation of enthalpy and entropy per atom, which can be deduced by this kind of graphic.

$$\Delta h_s = -\left(\frac{\partial \ln C}{\partial (1/kT)}\right) \quad \Delta S_s = \Delta h_s + k \ln C$$

Solid solution at high hydrogen concentration

Observing the dependence of ΔH_s from hydrogen concentration, it is possible to grasp that in all materials, it decreases initially and then it rises. The reason for this behaviour lies in the different kind of interaction between H atoms in the host material.

Interstitial atoms produce on the average a lattice deformation that makes easier entering the host material for the incoming hydrogen. The result is a lowering of the heat of solution, an effect independent from H atoms disposition, being connected just to their concentration, and that can be understood as a mean-field contribution.

In order to explain this phenomenon, let us suppose that the volume per M atom increases linearly with the H concentration, as

$$v = v_0 + C v_H$$

Where v_0 is the pure host metal volume per atom and v_H is derived from

$$v_H = \frac{\partial h^\alpha}{\partial p} + T \frac{\partial v_H}{\partial T} \approx \frac{\partial \Delta H_s}{\partial p}$$

The ΔH_s dependence from H concentration can be calculated as

$$\frac{d\Delta H_s}{dC} = \left(\frac{\partial \Delta H_s}{\partial V}\right)_c \frac{\partial V}{\partial C} + \left(\frac{\partial \Delta H_s}{\partial C}\right)_V$$

The first term is called the elastic contribution:

$$\left(\frac{\partial \Delta H_s}{\partial V}\right)_c \frac{\partial V}{\partial C} = \left(\frac{\partial \Delta H_s}{\partial p} \frac{\partial p}{\partial V}\right)_c \frac{\partial V}{\partial C} = -\gamma K_0 \frac{v_H^2}{v_0} = \gamma u_{els}$$

So the elastic contribution to ΔH_s can be written as the product between u_{els} and H concentration. γ is a correction factor, whose estimate is difficult, being linked to the Poisson's ratio, and varies between 0.5 and 1. The second term, the explicit derivative of the solution heat change respect to H concentration, represents the excess of electrons brought by the presence of interstitial atoms. In order to demonstrate the attracting interaction between H atoms at low concentration, it can be written

$$\Delta H_s - \Delta H_s^0 = -(u_{elastic} + u_{electronic})C = -uC$$

where u assumes only positive values.

This relation stands just for small values of H concentration: as mentioned before, for large C values ΔH_s rises. It is reasonable to explain that supposing that when H atoms are at short distances, their interaction becomes repulsive and there are at least three reasons.

The first one is an empirical rule, verified in many M-H systems, according to which the minimum distance between H atoms is 2.1 Å. Secondly, it is observed a reduction of the configurationally entropy, since the higher number of H atoms increases the mutual blocking: r decreases as C becomes larger. Finally, the formation of ordered structures explain the fact that interaction between H atoms is not attractive. If it had been true, at low temperatures phases rich in hydrogen would have formed.

The presence of attractive long-range interactions between H atoms determines the spinodal composition, present in the part of the phase diagram where two different phases coexist. The critical point, over which in temperature there is just one phase, can be determined imposing that

$$\frac{\partial \mu}{\partial C} = \frac{\partial^2 \mu}{\partial C^2} = 0$$

So, if $\mu = h_0 - uC + kT \ln \frac{C}{r-C}$, it is easy to derive that

$$C_c = r/2 \text{ and } T_c = ru/4k.$$

The spinodal decomposition can be also dependent on the sample shape. When two phases coexist, some stresses are created.

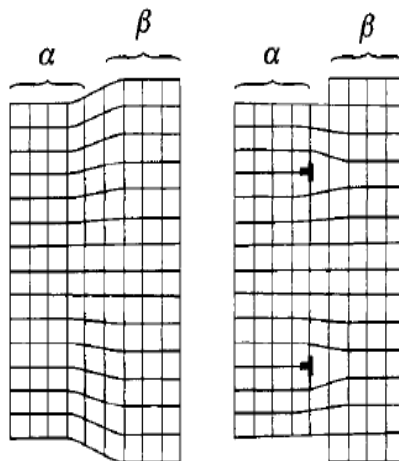


Figure 2-3

If the phase boundary is coherent (left side of Figure 2-3), certain modes of stress and concentration waves stand so that the free surface condition is respected and the spinodal composition is linked to the material

arrangement. On the contrary, this dependence vanishes if it is present an incoherent state (right side) where each stress relaxes at the grain boundaries.

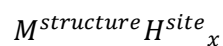
Hydrides structure

The term hydride can be addressed both to systems that changes their structure due to the presence of H atoms and to cases in which the distribution of hydrogen becomes ordered just at low temperatures. Generally, it is possible to speak of hydride when a phase metal-hydrogen has not a random structure of H interstitials.

Considering face centered cubic, base centered cubic or hexagonal closed packed metallic structures, hydrogen occupies just two types of interstitials: tetrahedral (T) and octahedral (O). More precisely:

- in the fcc lattice, T and O sites are surrounded by tetrahedral and octahedral M atoms, respectively;
- in the hcp structure, the polyhedron formed by the nearest M atoms is distorted when the axial ratio is different from the ideal value, in which the height over the hexagonal basis is $\sqrt{3}$;
- in the bcc lattice, each O site is surrounded by a strongly distorted octahedron, having two M atoms closer than the others. In this way it is possible to distinguish O_x , O_y , O_z sites and, similarly, T_x , T_y , T_z ones.

An useful notation to classify hydride uses the formula



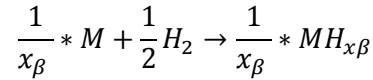
where x is a rational number that inform about the ratio of H atoms over M ones, structure has to be substituted by b (bcc), h (hcp) or f (fcc) and $site$ by t (tetrahedral) or o (octahedral).

It is useful to distinguish how hydrogen links itself to metal, according to the kind of metal considered:

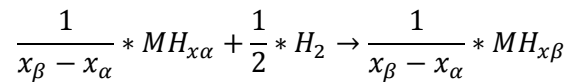
- fcc and hcp metals absorb hydrogen in O sites and form solid solutions until the value of x reaches the unity. In some cases, substoichiometric hydrates are formed by ordering vacancies in the hydrogen sublattice;
- bcc metals organize H atoms at low concentrations so that they occupy T sites randomly, but at high concentrations their disposition forms a sublattice that causes an overall crystal distortion;
- T sites are univocally occupied in hcp Ti and Zr solid solutions and when hydrogen links to rare-earth metals.

Hydride formation thermodynamics

The stability of a reaction can be described by the enthalpy change per H atom. So, the heat of formation of a hydrate $MH_{x\beta}$, Δh^β , is defined for a hypothetical reaction:



Actually, a hydride is formed by hydrogenation of an α -solid solution by a reaction like



In equilibrium condition the same reaction can be written using the thermodynamic quantity of chemical potential μ :

$$2(\mu_\alpha^M + C_\alpha \mu_\alpha^H) + (C_\beta - C_\alpha) \mu_{H_2} = 2(\mu_\beta^M + C_\beta \mu_\beta^H)$$

where C indicates the concentration, M stands for metal and H for hydrogen. The chemical potential can also be written as

$$\mu = \left(\frac{\partial G}{\partial n} \right) = \left(\frac{\partial H}{\partial n} \right) - T \left(\frac{\partial S}{\partial n} \right) = \bar{H} - T \bar{S}$$

where \bar{H} and \bar{S} are molar enthalpy and entropy. Defining:

$$\Delta H_{\alpha\beta} = 2 \frac{H_\beta - H_\alpha}{C_\beta - C_\alpha} - \bar{H}_{H_2}$$

$$\Delta S_{\alpha\beta} = 2 \frac{S_\beta - S_\alpha}{C_\beta - C_\alpha} - \bar{S}_{H_2}$$

where, if with x the two phases α and β are indicated:

$$H_x = \bar{H}_x^M + C_x \bar{H}_x^H \quad S_x = \bar{S}_x^M + C_x \bar{S}_x^H$$

Exploiting gas thermodynamics, it is possible to link partial molar entropy to the pressure with the following formula, where the apices 0 stands for the thermodynamic quantities at standard conditions ($p = 1 \text{ atm}, T = 298 \text{ K}$):

$$\bar{S}_{H_2} = -R * \ln \left(\frac{p}{p^0} \right) + S_{H_2}^0$$

Thus, rearranging the previous expressions, it is possible to write what follows

$$\ln\left(\frac{p}{p_0}\right) = \frac{\Delta H_{\alpha\beta}}{RT} - \frac{1}{R} \left(2 \frac{S_\beta - S_\alpha}{C_\beta - C_\alpha} - S_{H_2}^0 \right)$$

where p is the plateau equilibrium pressure that can be determined knowing the other parameters.

Experimentally, it is by far easier to measure equilibrium pressure in a phase diagram. Doing this operation at different temperatures let draw an Arrhenius plot, where the entropy and the enthalpy of formation can be derived fitting the line that is created putting the pressure logarithm on the y-axis and the inverse of temperature on the abscissa.

The enthalpy of formation and of phase change have very similar values and vary homogeneously across the periodic table, so it is possible to grasp that the electronic structure is more important than the crystalline structure or the hydrogen content in determining these values. Moreover, this behaviour is present also observing the values of entropy of formation and $\Delta S^{\alpha\beta}$, justifying the thesis according to which these parameters depend on the vanishing entropy of the hydrogen gas.

In order to demonstrate the similarity of the two enthalpies, let consider a crystal with N_0 metal atoms (chemical potential μ_0) and n hydrogen atoms (chemical potential μ), so that the system global Gibbs free energy is

$$G = N_0\mu_0 + n\mu$$

It is better to use

$$g = \frac{G}{N_0} = \mu_0 + C * \mu$$

In a Cg diagram the hydrogen chemical potential is the slope of the tangent to the $g(x)$ function and the metal lattice one is the intercept at x equal to zero.

The equilibrium conditions are written in terms of chemical potential as

$$\mu_0^\alpha(p, T, C_\alpha) = \mu_0^\beta(p, T, C_\beta) \quad \mu^\alpha(p, T, C_\alpha) = \mu^\beta(p, T, C_\beta) = \frac{1}{2} * \mu^g(p, T)$$

In the phase diagram the condition of the two phases coexistence is described by the common tangent rule

$$\mu(C_\alpha) = \mu(C_\beta) = \frac{g(C_\beta) - g(C_\alpha)}{C_\beta - C_\alpha}$$

The expression above is used when considering CT diagrams; when PCI ones are in use, it is better to write equilibrium conditions as

$$\frac{1}{2} * \ln \frac{p_{eq}}{p_0} = \frac{1}{kT} * \left(\mu^\beta - \frac{1}{2} \mu^{g0} \right) = \frac{1}{kT} * \left(\mu^\alpha - \frac{1}{2} \mu^{g0} \right)$$

This leads to the fact that enthalpy and entropy changes that determine the pressure plateau are equal to the enthalpy and entropy of formation of the coexisting phases. In symbols

$$\Delta h^{\alpha\beta} = \Delta h^\alpha(C_\alpha) = \Delta h^\beta(C_\beta) \qquad \Delta s^{\alpha\beta} = \Delta s^\alpha(C_\alpha) = \Delta s^\beta(C_\beta)$$

Enthalpy of formation is a central parameter to study a reaction: it determines the equilibrium pressure at a certain temperature and show the heat exchanged by the system with the environment. In the case in which the reaction is strongly exothermic, such as when hydrogen combines with magnesium to form magnesium hydride, it is easy to form the reaction product, but it results complicated to form the reagents again. It can be easily understood that the best configuration in order to use hydrogen like an energy vector is the one in which formation enthalpy is negative, so the reaction exothermic, but its modulus small, in the sense that it values just a few tens kJ/mol.

Equilibrium thermodynamics gives information weather a reaction happens or not, but it does not say how long it takes to happen. This fact, fundamental in order to exploit a determined material as hydrogen tank, is studied by kinetics.

Modelling a reaction from an initial state to a final one, it is possible to determine different free energy values: G_i of the initial metastable state, G_f of the final stable state and G_A of the activated state. This one is the situation by which the system must go through (Figure 2-4), going from the initial to the final state. So, while the driving force is given by the difference between G_i and G_f (in red), it is necessary to overcome the energy barrier formed by the gap between the energy of the activated state and the one of the initial one (in blue).

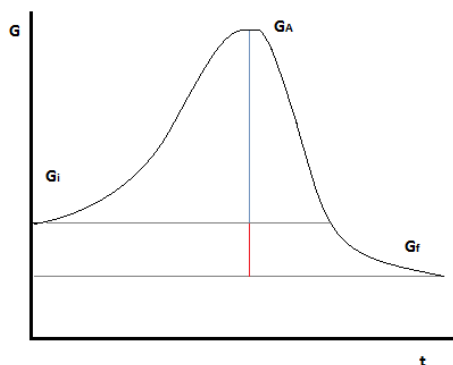


Figure 2-4

Energies showed in the graph are the averages over a large number of atoms that form the system. It may happen, of course, that some of them have a thermal energy able to make the atom pass the energy barrier without an external aid.

Terminal solubility

Terminal solubility stands for the maximum concentration of the solid solution (α -phase) in equilibrium with the coexisting hydride β -phase. The phase boundary is called solvus line.

There are three methods used to determine the terminal solubility:

- electrical resistivity: it increases as temperature rises, as hydride phase dissolution goes on, since resistivity is in general higher in disordered systems;
- specific heat: when the hydride dissolves a positive anomaly in specific heat is measured, for the change of enthalpy between the two phases;
- internal friction: performing internal friction measurements, while passing from a phase to the other, an extra energy loss is revealed. It is usually observed a hysteresis and the point of dissolution is higher during the heating than in the cooling down. It is a common practice to consider the points obtained during the heating run as the real dissolution points.

These operations are believed to be realistic since the equilibrium between the two phases is reached much faster than the one between solid and gas phases, due to the rapid diffusion of hydrogen in the solid phase. Now, the equilibrium condition is given by the equality between the two solid phases chemical potentials. Considering just small deviations of stoichiometry between α - and β -phases:

$$h^\alpha - Ts^{\alpha nc} + kT * \ln Z_\alpha = h^\beta - Ts^\beta$$

Where $Z_\alpha = x_\alpha / (r - x_\alpha)$. It implies

$$kT \ln Z_\alpha = -(h^\alpha - h^\beta) + T(s^{\alpha nc} - s^\beta) = -\Delta H_{solvus} + T\Delta S_{solvus}$$

If the right-hand terms had been temperature independent, it would have been possible to derivate enthalpy and entropy from an Arrhenius plot. Actually, they both are linked to the optical vibrational modes of hydrogen, even if this behaviour vanishes when H atoms occupy boundary sites. This dependence appears in the Arrhenius plots which show a curvature for high temperatures (Figure 2-5). However, the operational definition of ΔH_{solvus} and ΔS_{solvus} as slope and intercept of the tangent to Arrhenius plot leads to unreasonable results: high temperatures values are too large respect to the ones calculated from low temperatures data. If ΔS_{solvus} is considered independent from temperature, the bend at high

temperatures can be attributed to a decrease of ΔH_{solvus} whose behavior can be explained in terms of the attractive interaction between H atoms.

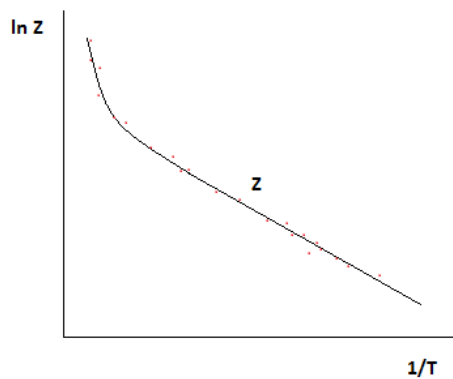


Figure 2-5

Destabilization of Mg-H system

In order to have technological application, a metal-hydrogen system should have an equilibrium pressure at room temperature around 10^5 Pa. For magnesium, this pressure is reached at 573 K, so it is necessary to change the system thermodynamic properties.

As said before the hydride is energetically favoured respect to the situation in which the gas and the metal do not interact. Anyway, there is an energetic barrier to overcome, determined by the energy needed to divide the hydrogen molecule (Figure 2-6). Once the hydride is formed, it is very hard to go back to the starting situation, due to the presence of an even higher energetic barrier, which limits the use of this solution for storage applications.

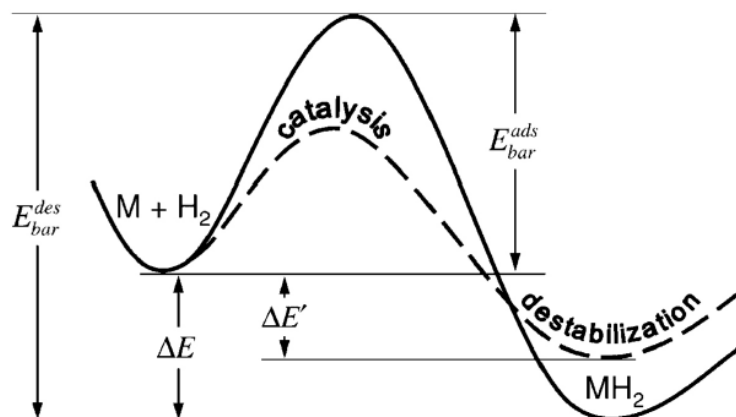


Figure 2-6

In general it is possible to lower the energetic barrier through two methods. One is called catalysis and it consists in adding some special materials to the system whose thermodynamic properties are so modified. The other one is the reduction of the hydride formation enthalpy by physical methods, as the introduction of elastic constraints. This solution is what is defined as destabilization.

During the absorption, the entering hydrogen enlarge the host metal volume. If something limits this expansion, an elastic energetic term is created and it changes de facto the hydride enthalpy of formation, modifying the equilibrium pressure respect to the one of the free expansion case. The net effect of this term is a growth of the equilibrium pressure. In this way, it is possible to obtain systems capable of releasing hydrogen at pressure values similar to the standard one.

Blocking systems can be obtained both in two and in three dimensions. 2-D systems, linked to thin films, were studied by the TU Delft group led by R. Griessen. They found that:

$$\ln\left(\frac{p^*}{p^{free}}\right) = \frac{E_{Mg}}{\hat{E}}(1 - \nu_{Mg}) + (1 - \nu_{cap})\frac{E_{Mg}d_{Mg}}{E_{cap}d_{cap}}$$

Where E_{Mg} and E_{cap} are the Young modules of magnesium and of the constraint, ν the Poisson's ratio, d the thickness and $\hat{E} = \frac{9}{4} * RT \frac{V_{Mg}}{V_H^2}$, with V as molar volume. Their results, summarized by the Figure 2-7, show that the best performances are achieved with palladium and nickel.

The experiments were performed at 333 K with samples of Ti (10nm), Mg (20 nm), X (10 nm), Pd (10 nm), where X can be Ni, Ti, Pd, V, Nb. The dashed line stands for the bulk results.

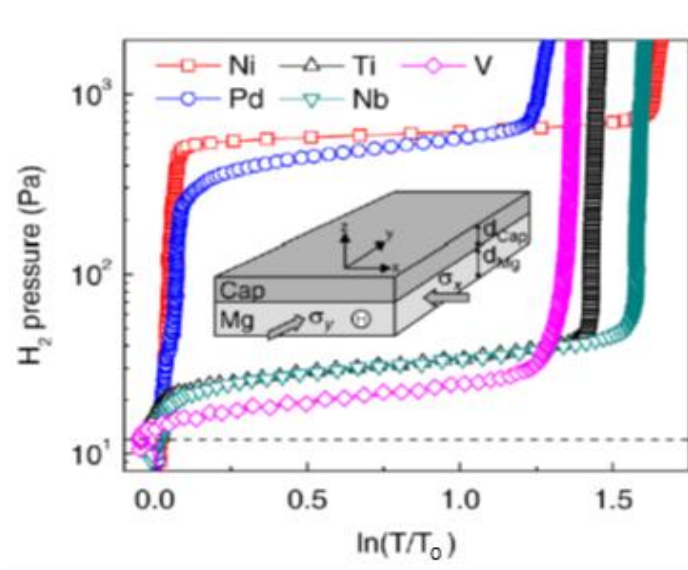


Figure 2-7

Figure 2-8 shows that varying the magnesium thickness makes clear that as it grows, it becomes more and more similar to the bulk equilibrium pressure. These experiments were performed at 333 K too, with samples of Ti (10 nm), Mg (z nm), Pd (40 nm).

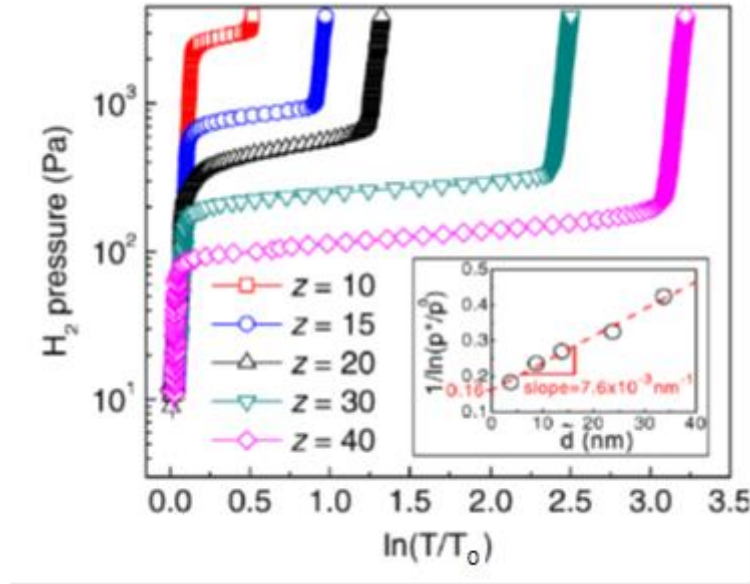


Figure 2-8

The systems studied in this work are not thin films but nanoparticles, whose 3-D limit should be another material shell which lowers the expansion.

Hydride formation enthalpy is volume depending by the bulk module B :

$$B = -V \left(\frac{\partial p}{\partial V} \right) = - \left(\frac{\partial p}{\partial \ln V} \right) = - \left(\frac{\partial p}{\partial \bar{H}} \frac{\partial \bar{H}}{\partial \ln V} \right) = - \frac{1}{\bar{V}} \left(\frac{\partial \bar{H}}{\partial \ln V} \right)$$

Where partial molar enthalpy and partial molar volume can be written as

$$\bar{H} = \frac{\partial H}{\partial n}$$

$$\bar{V} = \frac{\partial \bar{H}}{\partial p}$$

Using these results in the previous model formula, the ratio between the equilibrium pressures of the constrained nanoparticle and of the free one is, considering that the enthalpies for a hydrogen mole:

$$\frac{p^*}{p^{free}} = \exp \left(\frac{2 \left(\Delta H_{\alpha\beta}^* - \Delta H_{\alpha\beta}^{free} \right)}{RT} \right)$$

The difference between the enthalpies of the free and of the constrained case can be approximated with the difference between the hydrogen enthalpies inside the metal:

$$\Delta H_{\alpha\beta}^* - \Delta H_{\alpha\beta}^{free} = \Delta \bar{H}_H^\beta$$

After some mathematics it is obtained that:

$$\frac{p^*}{p^{free}} = \exp\left(-\frac{2B\bar{V}_H}{RT} \frac{dV}{V}\right)$$

$\frac{dV}{V}$ is an unknown term. In the core-shell geometry the nanoparticles are considered as spheres of radius R , surrounded by a layer whose thickness is called d (Figure 2-9). At the interface, the boundary conditions are:

$$\sigma_{rr}^s = -p$$

$$\sigma_{rr}^c = p$$

In the free case, if the particle has a relative expansion of $\frac{\varphi}{R}$, its volume variation is

$$\left(\frac{dV}{V}\right)^{free} = 3\frac{\varphi}{R} = 2\frac{\bar{V}_H}{V_{Mg}}$$

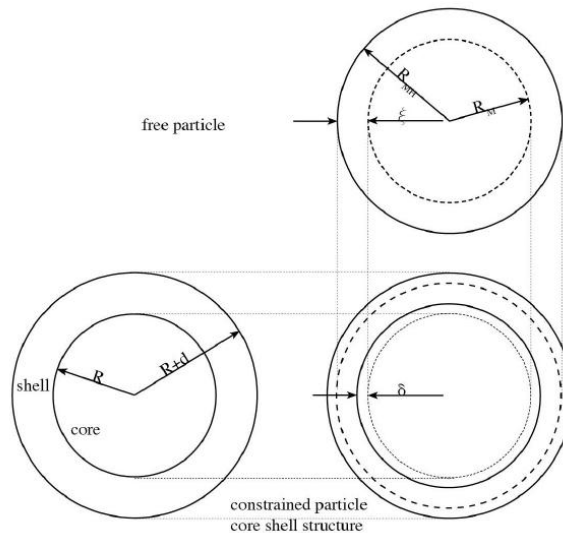


Figure 2-9

When the constraint is introduced, the expansion is reduced to the value δ with $0 < \delta < \varphi$. For $\delta = 0$ the expansion is blocked, for $\delta = \varphi$ there is the free case. Moreover, the volume variation results:

$$\frac{dV}{V} = -3\frac{\varphi - \delta}{R}$$

Using the definition of compression module K , the relation of the pressure at the interface is calculated

$$K = -V \left(\frac{\partial p}{\partial V} \right)$$

$$dp = -K \frac{dV}{V}$$

Being $K = \frac{E}{3(1-2\nu)}$ it is possible to obtain

$$p = -\frac{E}{3(1-2\nu_c)} \frac{dV}{V} = \frac{E}{(1-2\nu_c)} \frac{\varphi - \delta}{R}$$

Where the subscript c stands for core.

For what concern the shell, it can be pictured as a circular crown subjected to an internal pressure p_1 and an external one p_2 , so that it results

$$u_{rr} = a - \frac{2b}{r^3}$$

$$u_{\theta\theta} = u_{\phi\phi} = a + \frac{b}{r^3}$$

$$\sigma_{rr} = a \frac{E}{1-2\nu} - \frac{b2E}{1+\nu r^3}$$

Using the boundary conditions, the coefficients are determined

$$a = \frac{p(1-2\nu_s)}{E_s(\rho^3-1)}$$

$$b = p \frac{(1+\nu_s)(R+d)^3}{2E_s(\rho^3-1)}$$

With the subscript s indicating the shell and $\rho = \frac{R+d}{R}$.

Thus, the deformation is

$$u_r = ar + \frac{b}{r^2}$$

and

$$\sigma_{rr}^s = p \frac{3(1-2\nu_s)}{(1+\nu_s)(\rho^3-1)} - 2 \frac{E_s}{(1+\nu_s)} \frac{u_r}{r}$$

Rearranging the terms, the volume variation from the constrained case to the free one is

$$\frac{dV}{V} = -\frac{3u}{R} = -3\frac{\varphi}{R} \frac{2\sigma(\rho^3 - 1)}{\rho^3 \frac{(1 + \nu_s)}{(1 - 2\nu_c)} + 2\frac{(1 - 2\nu_s)}{(1 - 2\nu_c)} + 2\sigma(\rho^3 - 1)}$$

Considering that $(\frac{dV}{V})^{free} = \frac{3\varphi}{R}$, it follows that

$$\frac{dV}{V} = -2\frac{\bar{V}_H}{V_{Mg}} \frac{2\sigma(\rho^3 - 1)}{\rho^3 \frac{(1 + \nu_s)}{(1 - 2\nu_c)} + 2\frac{(1 - 2\nu_s)}{(1 - 2\nu_c)} + 2\sigma(\rho^3 - 1)}$$

In conclusion the equilibrium pressure variation from the free case to the constrained one is

$$\ln\left(\frac{p^*}{p^{free}}\right) = \frac{4B}{RT} \frac{\bar{V}_H^2}{V_{Mg}} \frac{2\sigma(\rho^3 - 1)}{\rho^3 \frac{(1 + \nu_s)}{(1 - 2\nu_c)} + 2\frac{(1 - 2\nu_s)}{(1 - 2\nu_c)} + 2\sigma(\rho^3 - 1)}$$

CHAPTER III. Hydrogen

General features

Hydrogen is the first element of the periodic table and the simplest atom in nature, being made up of a proton, which forms the nucleus, and an electron (Figure 3-1). This fact is the basis of many of its features such as the electronegativity value, which is the ability to attract an electron from another atom, its small atomic size and nuclear mass. These fundamental characteristics are linked to the formation of the bond between a metal and an hydrogen atom.

As regards electronegativity, hydrogen has a medium value, so that it can form a wide range of bonds: both covalent and metallic (when the electronegativities of the atoms considered are similar) and ionic (a process that needs the transfer of an electron from the atom with the lowest electronegativity to the one which has the highest).

Neutral hydrogen has a radius of 0.529 \AA , as calculated by Bohr. This result revealed to be so important that this distance is called Bohr's radius and indicated by a_B . H^- , an atom with an extra electron, has a ionic radius of 2.1 \AA , while H^+ , that a simple proton, according to Shannon and Prewitt, varies from -0.18 \AA and -0.38 \AA [10]. The minus sign stands for the fact that the proton, or ion H^+ , attracts the surroundings electrons, creating a deformation of the ambient around the atom.

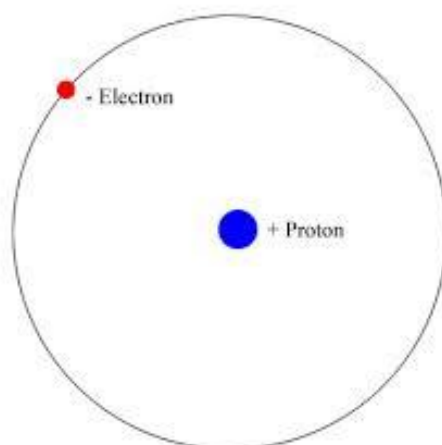


Figure 3-1

The small nuclear mass of the hydrogen atom (1.00794 amu) and strong binding interactions make the molecular vibrational levels distanced and isotope dependent. When hydrogen is linked to a metallic atom, it is possible to distinguish from the oscillator system two components: one (acoustic) with low frequencies

and similar to the vibrations of the lattice of the host metal and one (optic) with high frequencies, typical of H atoms. Vibrations of hydrogen atoms have also a finite extension, comparable to the Bohr's radius. Assuming the adiabatic approximation, H atoms may be pictured as harmonic oscillators. In this case, the wave function has a spatial variation depending on $e^{-(x/d)^2}$, where

$$d = \frac{h}{\sqrt{2\pi\Delta E}}$$

ΔE is the excitation energy of about 0.1 eV. In this way, d gets a value of about 0.3 Å.

Hydrogen has two isotopes: deuterium and tritium. While deuterium has a nucleus made up of a proton and a neutron, tritium has one more neutron forming the nucleus. It is possible to summarize their properties with Table 2 [11].

Table 2

	H	D	T
NULCEUS			
Mass	1.000	1.998	2.993
Spin	1/2	1	1/2
Moment [μ_B]	2.7928	0.8574	2.9788
ATOM			
Ionization energy [eV]	13.5989	13.0625	13.6038
MOLECULE			
Binding energy [eV]	4.748	4.748	-
Dissociation energy [eV]	4.478	4.556	4.59
Vibrational energy [eV]	0.5160	0.3712	0.3402
Rotational energy [eV]	$7.32 \cdot 10^{-3}$	$3.70 \cdot 10^{-3}$	-
GAS LIQUID			
Critical temperature [K]	32.98	38.34	40.44
Critical pressure [MPa]	1.298	1.649	1.906
GAS LIQUID SOLID			
Triple point			
temperature [K]	13.96	18.73	20.62
Triple point pressure [kPa]	7.20	17.15	21.60

Hydrogen molecule according to quantum mechanics

Hydrogen molecule is made up of two atoms. It is possible to study the way by which two H atoms bound together, forming the molecule, according to quantum theory. In fact, even if Bohr's semi-classic theory has been able to explain the structure of a hydrogen atom since 1913, there is not a non quantum theory able to interpret even the simplest molecules.

The problem of hydrogen ones was resolved for the first time by Heitler and London in 1927 [12]. Hydrogen molecule theory is of fundamental importance because it shows the stability of the bound and its saturation, the fact that just two atom can unite. It is the prototype of all molecular not electrostatic bounds: covalent ones.

Let consider two electrons (1 and 2) in the field of two unitary charged nuclei (a and b) that are divided by a fixed distance R_{ab} . If it is enough large, we have two isolated atoms, so electron 1 is referred to a nucleus, and 2 to b . It is possible to describe this situation by the wave function:

$$\varphi_{0a}(\mathbf{r}_1)\varphi_{0b}(\mathbf{r}_2)$$

Where these are hydrogen fundamental state normalized eigenfunctions, centred respectively in a and b nuclei.

Energy, or the expectation value of the operator H_1+H_2 , where H_1 and H_2 are the Hamiltonian of the two separated nuclei, is obviously $2E_0$, if E_0 is each atom energy (-13.59 eV). This is the case in which R_{ab} is large.

If it is not, there is an appreciable possibility that electrons exchange one another, creating the state described by the function

$$\varphi_{0a}(\mathbf{r}_2)\varphi_{0b}(\mathbf{r}_1)$$

So the wave function results to be

$$\frac{1}{\sqrt{2}}[\varphi_{0a}(\mathbf{r}_1)\varphi_{0b}(\mathbf{r}_2) + \mu * \varphi_{0a}(\mathbf{r}_2)\varphi_{0b}(\mathbf{r}_1)]$$

This function must be integrated with the spin eigenfunction $\chi(\boldsymbol{\sigma}_1, \boldsymbol{\sigma}_2)$. The total wave function is

$$\Psi = \frac{1}{\sqrt{2}}[\varphi_{0a}(\mathbf{r}_1)\varphi_{0b}(\mathbf{r}_2) + \mu\varphi_{0a}(\mathbf{r}_2)\varphi_{0b}(\mathbf{r}_1)]\chi(\boldsymbol{\sigma}_1, \boldsymbol{\sigma}_2)$$

Eigenfunctions for a couple of spins are an antisymmetric one χ_a , corresponding to antiparallel spins, and three symmetric ones χ_1, χ_2, χ_3 , that describe parallel spins orientation. In order to respect the global

antisymmetry of the function Ψ it is important to choose the right μ value: -1 for antiparallel spins and +1 for parallel ones.

$$\chi_a = \frac{1}{\sqrt{2}}(|\downarrow\uparrow\rangle - |\uparrow\downarrow\rangle)$$

$$\chi_1 = |\uparrow\uparrow\rangle$$

$$\chi_2 = |\downarrow\downarrow\rangle$$

$$\chi_3 = \frac{1}{\sqrt{2}}(|\uparrow\downarrow\rangle + |\downarrow\uparrow\rangle)$$

Let calculate energy

$$W = \int \Psi H \Psi^* dV$$

Where H includes all the interactions between electrons, electrons and nuclei and nuclei themselves. It is possible to write

$$H = -\frac{\hbar^2}{2m}(\nabla_1^2 + \nabla_2^2) - e^2\left(\frac{1}{r_{1a}} + \frac{1}{r_{1b}} + \frac{1}{r_{2a}} + \frac{1}{r_{2b}}\right) + \frac{e^2}{r_{12}} + \frac{e^2}{R_{ab}}$$

Final result can be expressed as

$$W = 2E_0 + \frac{e^2}{R_{ab}} + J \pm K$$

With + as $\mu=+1$ and - as $\mu=-1$. J and K are

$$J = e^2 \int \left(\frac{1}{r_{12}} - \frac{1}{r_{1b}} - \frac{1}{r_{2a}}\right) |\varphi_{0a}(\mathbf{r}_1)|^2 |\varphi_{0b}(\mathbf{r}_2)|^2 dV_1 dV_2$$

$$W = Re \left[e^2 \int \left(\frac{1}{r_{12}} - \frac{1}{r_{1b}} - \frac{1}{r_{2a}}\right) (\varphi_{0a}(\mathbf{r}_1)\varphi_{0b}(\mathbf{r}_2))^* \varphi_{0a}(\mathbf{r}_2)\varphi_{0b}(\mathbf{r}_1) dV_1 dV_2 \right]$$

J is called coulombian integral and K exchange integral.

Both J and K are negative in the region of the distances R_{ab} that are the ones where the molecule is created, but K is much bigger and can enter the energy expression with the opposite sign. So the attractive or repulsive character of the interaction is determined by this parameter.

According to this model, the minimum of energy is 3.14 eV (4.48 is the experimental value) and the equilibrium distance 0.80 Å, instead of 0.74 Å (Figure 3-2).

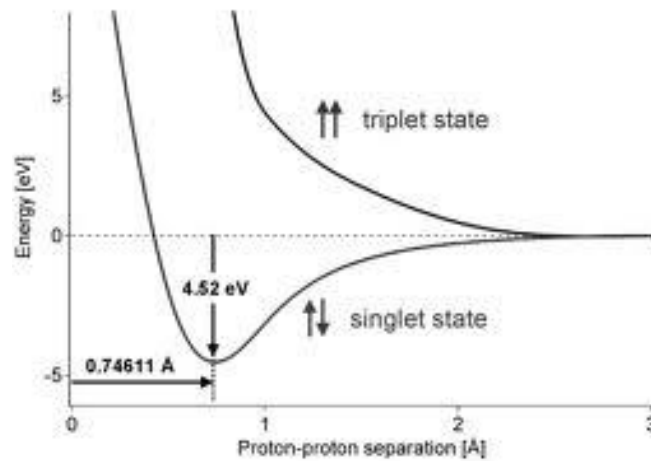


Figure 3-2

Molecular hydrogen exists in three different states in nature: solid, liquid and gas. The triple point is defined by $T_{\text{triple}} = 13.96 \text{ K}$ and $P_{\text{triple}} = 7.20 \text{ kPa}$ and the critical one, as mentioned before, by $T_c = 32.98 \text{ K}$ and $P_c = 1.298 \text{ MPa}$ [13], as shown by Figure 3-3.

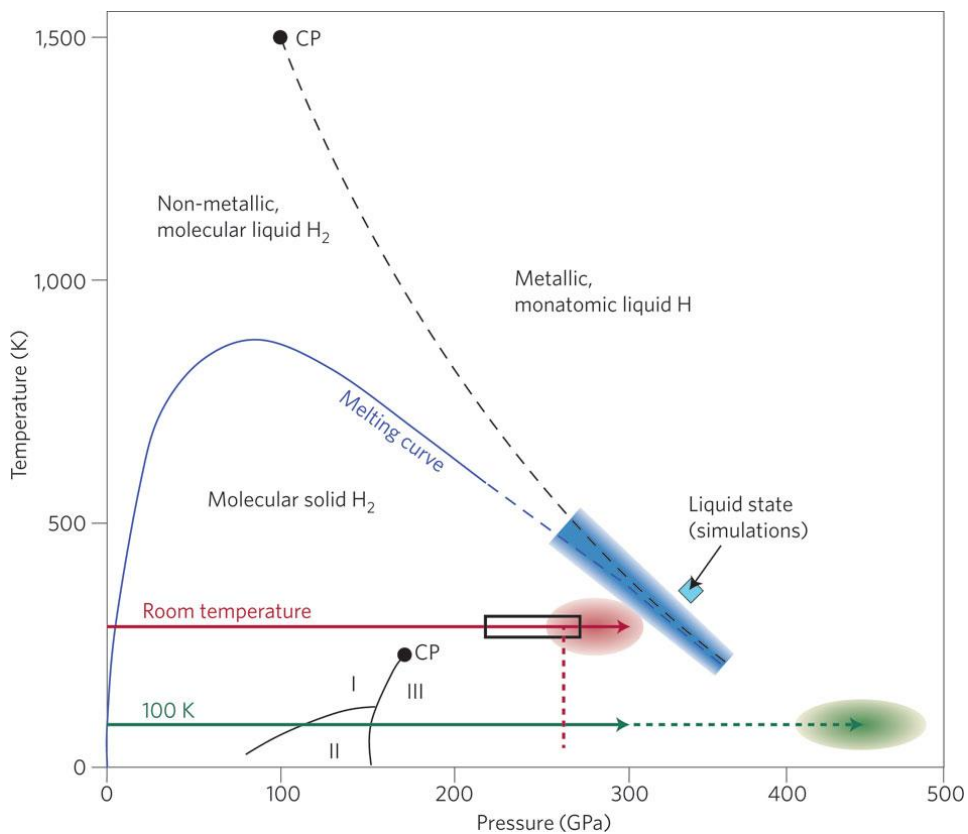


Figure 3-3

Under ordinary conditions ($T > RT$, $P < 10 \text{ MPa}$) hydrogen may be described as an ideal gas. According to this assumption, the values of, respectively, chemical potential, equilibrium pressure, enthalpy and entropy per molecule are:

$$\mu^g = kT \ln \frac{P}{P_0} - E_d$$

$$P_0(T) = \frac{(4\pi M kT)^{\frac{3}{2}} 4\pi I (kT)^2}{h^5}$$

$$h^g = \frac{7}{2} kT - E_d$$

$$\frac{s^g}{k} = \frac{7}{2} - \ln \frac{P}{P_0}$$

It is also possible to write, with $T^* = 9.20 \text{ K}$

$$\frac{P_0(T)}{P_0} = \left(\frac{T}{T^*}\right)^{7/2}$$

Even if considering hydrogen molecules as forming an ideal gas is often a very good approximation, in some situation its behaviour deviates from that. For example, at RT and 10 MPa, the experimental value is 6% larger than the ideal one, increasing the chemical potential of 1.1% from the ideal gas value.

CHAPTER IV. Materials

Magnesium

Magnesium is an alkaline earth metal and the 8th most diffused element on Earth's surface and the 4th in the planet behind iron, oxygen and silicon [14]. It is a fundamental element in human biology too: its ions, the most diffused one is Mg⁺², are necessary to living cells, nucleic acids and enzymes and their presence determines the taste of natural water.

Magnesium has three stable isotopes: Mg²⁴, Mg²⁵ and Mg²⁶. All are present in significant amounts, but 79% of magnesium is Mg²⁶. The isotope Mg²⁸ is radioactive. Being very reactive, pure metal is not found naturally, so it is produced industrially by electrolysis.

Pure magnesium is a strong, light-weight metal which looks silvery white, tarnishing slightly with air exposition, and reacts with water at room temperature. Magnesium burns easily when in powder and produces a brilliant and white light with radiations going into deep ultraviolet.

Magnesium is widely used as structural metal and finds many applications as component in aluminium and zinc alloys, in the removal of sulphur during the production of iron and steel, in the production of titanium and in the manufacturing of high volume parts, for example in the automobile industry. Being a very light component, it can find wide diffusion in electronic components.

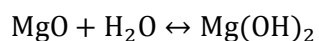
Table 3

Magnesium [15]	
General properties	
Element category	alkaline earth metal
Group, period, block	2, 3,s
Standard atomic weight	24.305(1)
Electron configuration	[Ne] 3s ² 2, 8, 2
Physical properties	
Density (RT)	1738 kg·m ⁻³
Liquid density (atm.p.)	1584 kg·m ⁻³
Melting point	923 K

Boiling point	1363 K
Heat of fusion	8.48 kJ·mol ⁻¹
Heat of vaporization	128 kJ·mol ⁻¹
Molar heat capacity	24.869 J·mol ⁻¹ ·K ⁻¹
Atomic properties	
Oxidation states	+2, +1
Electronegativity (Pauling scale)	1.31
Ionization energies	1st: 737.7 kJ·mol ⁻¹
Atomic radius	160 pm
Covalent radius	141±7 pm
Van der Waals radius	173 pm
Miscellanea	
Crystal structure	hexagonal close-packed
Magnetic ordering	paramagnetic
Electrical resistivity	(20 °C) 43.9 nΩ·m
Thermal conductivity	156 W·m ⁻¹ ·K ⁻¹
Thermal expansion	(25 °C) 24.8 μm·m ⁻¹ ·K ⁻¹
Speed of sound	4940 m·s ⁻¹
Young's modulus	45 GPa
Shear modulus	17 GPa
Bulk modulus	45 GPa
Poisson ratio	0.290
Mohs hardness	2.5

Magnesium oxide

Magnesium oxide is a white hygroscopic solid mineral. It has an empirical formula of MgO and consists of a lattice of Mg²⁺ ions and O²⁻ ions held together by ionic bonding. Magnesium hydroxide forms in the presence of water, but it can be reversed by heating it to separate moisture, according to the reaction



It is also possible to find magnesium peroxide MgO_2 but it is a metastable compound. According to evolutionary crystal structure prediction, MgO_2 is thermodynamically stable at pressures above 116 GPa and a totally new semiconducting suboxide Mg_3O_2 is thermodynamically stable above 500 GPa [16].

Magnesium oxide is used as a refractory material in furnace linings for producing iron, steel, nonferrous metals, glass, and cement. MgO finds applications also in the agricultural, chemical, and construction industries, often as an electrical insulator in fire-resistant cables.

Table 4

Magnesium oxide [17]	
Properties	
Molecular formula	MgO
Molar mass	40.3044 g/mol
Density	3580 kg/m ³
Melting point	3125 K
Boiling point	3870 K
Solubility in water	0.0086 g/100 mL (30 °C)
Acidity (pK_a)	10.3
Band gap	7.8 eV
Thermal conductivity	45–60 W·m ⁻¹ ·K ⁻¹
Refractive index(<i>n_D</i>)	1.736
Structure	
Crystal structure	Halite (cubic), cF8
Space group	Fm $\bar{3}$ m, No. 225
Coordination geometry	Octahedral (Mg ²⁺); octahedral (O ²⁻)
Thermochemistry	
Std enthalpy of formation $\Delta_f H^\ominus_{298}$	-602 kJ·mol ⁻¹
Standard molar entropy S^\ominus_{298}	27 J·mol ⁻¹ ·K ⁻¹

Palladium

Palladium is an element with the chemical symbol Pd and an atomic number of 46. Palladium belongs to group 10 of the periodic table, but has a very atypical configuration in its outermost electron shells compared to the other members of group 10, having fewer filled electron shells than the elements directly preceding it (a phenomenon unique to palladium).

Palladium is a soft silver-white metal that resembles platinum. It is the least dense and has the lowest melting point of the platinum group metals. It is soft and ductile when annealed and greatly increases its strength and hardness when it is cold-worked.

Naturally occurring palladium is composed of seven isotopes, which includes six stable isotopes. The most stable radioisotopes are ^{107}Pd with a half-life of 6.5 million years (found in nature), ^{103}Pd with a half-life of 17 days, and ^{100}Pd with a half-life of 3.63 days.

Over half of the supply of palladium and its congener platinum goes into catalytic converters, which convert up to 90% of harmful gases from auto exhaust (hydrocarbons, carbon monoxide, and nitrogen dioxide) into less-harmful substances (nitrogen, carbon dioxide and water vapour). The second-biggest application of palladium in electronics is in the manufacture of multilayer ceramic capacitors, in which palladium (and palladium-silver alloys) are used as electrodes. Palladium (sometimes alloyed with nickel) is used in connector plating in consumer electronics. Palladium is also used in dentistry, medicine, hydrogen purification, chemical applications, groundwater treatment and jewellery. Palladium plays a key role in the technology used for fuel cells, which combine hydrogen and oxygen to produce electricity, heat, and water. Palladium readily absorbs hydrogen at room temperatures forming palladium hydride PdH_x with x below 1. While this property is common to many transition metals, palladium is unique by the high absorption capacity and by that it does not lose its ductility until high x value. This property has been investigated for designing an efficient, yet inexpensive hydrogen storage material (palladium itself is prohibitively expensive for this purpose).

Ore deposits of palladium and other PGMs are rare and the most extensive deposits have been found in the Transvaal Basin in South Africa, the Stillwater Complex in Montana, United States, the Thunder Bay District of Ontario, Canada, and the Norilsk Complex in Russia. Recycling is also a source of palladium, mostly from scrapped catalytic converters [18].

The numerous applications and limited supply sources of palladium result in the metal attracting considerable investment interest.

Table 5

Palladium [19]	
General properties	
Element category	transition metal
Group, period, block	10, 5, d
Standard atomic weight	106.42
Electron configuration	[Kr] 4d ¹⁰ 2, 8, 18, 18
Physical properties	
Density (near r.t.)	12.023 g·cm ⁻³
Liquid density atm.p.	10.38 g·cm ⁻³
Melting point	1828.05 K, 1554.9 °C, 2830.82 °F
Boiling point	3236 K, 2963 °C, 5365 °F
Heat of fusion	16.74 kJ·mol ⁻¹
Heat of vaporization	358 kJ·mol ⁻¹
Molar heat capacity	25.98 J·mol ⁻¹ ·K ⁻¹
Atomic properties	
Oxidation states	0, +1, +2, +4
Electronegativity (Pauling scale)	2.20
Ionization energies	1st: 804.4 kJ·mol ⁻¹
Atomic radius	137 pm
Covalent radius	139±6 pm
Van der Waals radius	163 pm
Miscellanea	
Crystal structure	face-centred cubic
Magnetic ordering	paramagnetic
Electrical resistivity	(20 °C) 105.4 nΩ·m
Thermal conductivity	71.8 W·m ⁻¹ ·K ⁻¹
Thermal expansion	(25 °C) 11.8 μm·m ⁻¹ ·K ⁻¹
Speed of sound	3070 m·s ⁻¹
Young's modulus	121 GPa

Shear modulus	44 GPa
Bulk modulus	180 GPa
Poisson ratio	0.39
Mohs hardness	4.75

CHAPTER V. Inert Gas Condensation

General features

Low dimensional systems can be produced by two opposite approaches: one called *bottom up*, according to which the nano-system is built putting more and more material on a substrate, and another defined *top-down*, where a bulk material is divided into more and more pieces, smaller and smaller.

Inert Gas Condensation (IGC) can be listed in the first group and represents a wide diffused method to build nanoparticles, due to its simplicity and easiness of controlling the growth. Schematically it can be described in the following way: a bulk sample is heated (usually by Joule's effect making a current pass between two electrodes) so that it sublimates. The material produced is directed to the substrate and cooled by an inert gas flow. As the material reaches the target, different phenomena can occur: particles may move, interact and melt together.

Since this technique concerns very sophisticated systems, high purity of the evaporated samples and high vacuum levels in the work chamber are requested.

Experimental setup

The main chamber experimental set up used in this work is made up of (Figure 5-1):

- An ultra high vacuum chamber produced in inox steel *Thermionics NANO-A-2L-2-S* with a diameter of 45 cm and 69 cm high, resulting in a volume of about 110 litres, with a window which permits to look at what happens in the chamber itself;
- Two tungsten boats, hold between two copper electrodes heated by Joule's effect and containing a hole in which the material to be sublimated is put;
- Two current generators *Thermoionics HCPS 8*, by which a high alternate current is generated
- Water cooling pipelines;
- A channel, which directs He flow and makes, together with the inert gas, the metallic vapours go towards the chamber centre;
- A *Bronkhorst Hi-Tech's EL-FLOW select F201CV* mass flow controller;

- A metallic cylinder, which can rotate directed by the operator outside the chamber, with a diameter of 15 mm and 30,5 cm high;
- An *Edwards - Film Thickness Monitor FTM7 E0886-69-000* quartz microbalance, able to monitor the quantity of material deposited through the change of the quartz crystal vibrational frequency. Measurements depends also on pressure and temperature changes;
- A *Varian TURBO-V300* turbomolecular pump, with maximum flow of 300 lt/s and minimum vacuum value of about 10^{-7} torr;
- An *Edwards E2M18* rotational pump, with maximum flow of 5,7 lt/s and minimum vacuum value of about 10^{-3} torr, able to pump either the chamber in order to make the so called pre-vacuum and the back of the turbomolecular pump, thanks to a specific system of valves;
- A *Varian ConvecTorr p-type* Pirani IMG vacuum sensor;
- A *Varian cermaical CDG gauge VCMT13TGA* capacitive pressure sensor, able to measure He flow;
- A *Varian Multi-gauge controller L8350301* controller, able to manage the turbomolecular pump, Pirani and IMG sensors;
- A PC software implemented by LabVIEW, which controls the ceramic pressure sensor, the quartz balance, the tension between the electrodes and the flow controller.

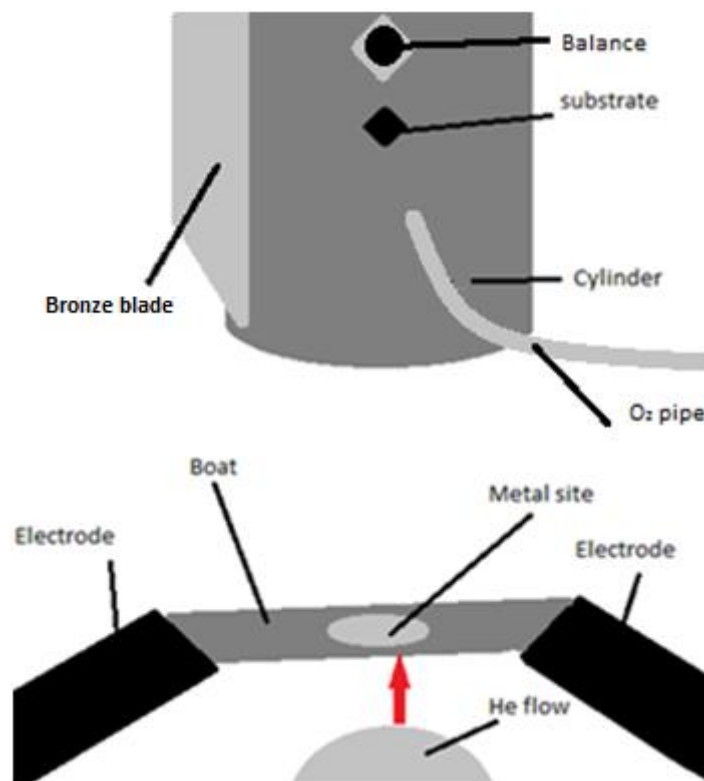


Figure 5-1

Next to the main chamber there is a smaller one for compaction of pellets. These two volumes are linked by a gate and it is possible to transfer the sample powders by a bowl attached to a magnetic field by that is manually controlled by the user. The central part of the chamber has got a fixed piston on which powders are deposited and a mobile one, connected to a hydraulic press *SPX Power Team 100TON*.

It is possible both to make hydrogen enter and interact with the sample and to treat it thermally due to the presence of an oven whose action takes place thanks to electrical resistances. This system is cooled by water pipes.

The second chamber is equipped by:

- An *Edwards E2M18* rotational pump, with maximum flow of 5,7 lt/s and minimum vacuum value of about 10^{-3} torr, able to pump either the chamber in order to make the so called pre-vacuum and the back of the turbomolecular pump, thanks to a specific system of valves;
- A *Varian TURBO - V70* turbomolecular pump, with maximum flow of 70 lt/s;
- A *Varian ConvecTorr p-type* Pirani IMG vacuum sensor.

Powders are produced in the main chamber evaporating the material flow on the central cylinder which rotates by the action of an engine and which is cooled filling the core with liquid nitrogen. Once deposited, the material is scraped by a bronze blade and collected in the blow for transfer.

The setup used has got two peculiarities: the possibility of creating more samples during a single experiment and of inserting an oxygen leak.

As regards the first one, the fact that the cylinder can rotate and that it can be directed by the user has made possible the synthesis of more samples during a single experiment. This setup characteristic was exploited to create samples with different exposition times to the material flow. After an initial phase during which the deposition rate was not constant and the flux was directed towards a part of the cylinder without substrates, the user rotated the cylinder so that the material could be deposited on them. This operation could be controlled by the window. In order to change the substrate and synthesize a new sample, the user just had to move the cylinder again.

The control of the oxygen leak can be considered one of the most original contributes of this work. The oxygen line is provided with a needle valve that, together with the pressure control made by the PC software, has permitted to obtain and estimate very small oxygen flow values. The oxygen line was filled with low quantities of gas and the chamber pressure set at about 0,6 torr. After that, the valve was just barely opened and a chronometer started. It was stopped as the pressure arrived to 0,7 torr, so that the

flux could be calculated. If it was too high, the chamber was emptied by the rotational pump and the previous steps done again, until the flux value was the one desired.

CHAPTER VI. Nucleation theories

Classical nucleation theory

IGC is a technique in which nanoparticles are formed during the vapour phase through a process defined homogeneous nucleation. This situation is made possible due to the fact that the gas becomes oversaturated: even partial pressure lowers during the gas diffusion, its cooling, helped by the inert gas flow presence, makes equilibrium pressure lower more. The result is the nucleation start.

Let consider a nucleus made up of v atoms and let μ^α and μ^β be the chemical potentials of the two phases α and β . In this way, it is possible to write the bulk free energy as

$$\Delta G_{bulk} = v(\mu^\alpha - \mu^\beta)$$

Being the nucleus small, it is impossible to point it as a thermodynamic system where surface contributes are neglected. Let call γ be the surface energy and η a geometrical coefficient, so

$$\Delta G_{surface} = \eta\gamma v^{2/3}$$

Then

$$\Delta G = \Delta G_{bulk} + \Delta G_{surface}$$

The two contributes have opposite sign, as the system is instable, so that for low values of v free energy increases until it reaches a maximum value, that can be pointed as ΔG_c , after which it lowers.

That maximum value and v_c , the relative number of atoms forming the nucleus with the highest value of free energy, can be determined imposing

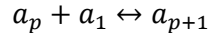
$$\frac{d\Delta G}{dv} = 0$$

Results are

$$v_c = -\frac{8(\eta\gamma)^3}{27(\mu^\alpha - \mu^\beta)^3}$$

$$\Delta G_c = \frac{1}{3}\eta\gamma v_c^{2/3}$$

The process of formation of a cluster composed of $p + 1$ particles can be described by the following expression



the process is reversible. Let write the cluster flux from a one of ν particles to a one of $\nu + 1$ particles as:

$$J_\nu = \beta_\nu N_\nu - \alpha_{\nu+1} N_{\nu+1}$$

Where β_ν describes the probability of the creation of a $\nu + 1$ particles cluster and $\alpha_{\nu+1}$ the passage from $\nu + 1$ to ν . Assuming that most of the material is in the initial phase, it can be derived, with ΔG standing for Gibbs free energy, that

$$N_\nu = N e^{-\Delta G/(kT)}$$

So, at the equilibrium J is zero and

$$\alpha_{\nu+1} = \beta_\nu * \frac{N_\nu}{N_{\nu+1}} = \beta_\nu \exp\left(\frac{\Delta G_{\nu+1} - \Delta G_\nu}{kT}\right) \approx \beta_\nu \exp\left(\frac{1}{kT} * \frac{\partial \Delta G}{\partial \nu}\right)$$

Supposing that $Z_{\nu+1} \approx Z_\nu + \frac{\partial Z}{\partial \nu}$ and that $J(t) = J \forall t$

$$J = \beta_\nu N_\nu * \left(\frac{Z_\nu}{N_\nu} - \frac{Z_{\nu+1}}{N_{\nu+1}}\right)$$

Where Z represent the numerical cluster distribution. If $Z_\nu = N_\nu$ for $\nu \leq p$ and $Z_\nu = 0$ for $\nu > s$ where p and s are two values of the number of particles, after some mathematical passages, it is possible to obtain:

$$J = \beta_c N \sqrt{\frac{\Delta G_c}{3\pi kT v_c^2}} * \exp\left(-\frac{\Delta G_c}{kT}\right)$$

The term under square root is called Zeldovich factor and its values is typically 0,1.

Beyond classical theory

Nucleation theory is not self-consistent as it will be proved later. However, beyond mathematical considerations, it is necessary to say that classical theory does not pay attention to cluster translational and rotational degrees of freedom and to its partial pressure.

Several attempts to overcome these limits have been made by physicists.

Dillman and Meier added the curvature dependence of the surface energy and additional degrees of freedom in order to get thermodynamic consistency [20]. They found that

$$\frac{\Delta G}{kT} = u(v) * v^{2/3} \gamma' + \tau * \ln(v) - \ln(q_0 V) - v \Delta G_{bulk}'$$

where $u(v)$ describes the size dependence of the surface free energy and the second and the third terms shows the difference between the molecular structure of a free cluster and a group of the same number of particles in the bulk material. τ and q_0 are two coefficients whose values are derived by the fit of critical density and pressure.

The so called "density functional theory" states that any nucleating system has an inhomogeneous structure whose free energy is a unique functional of the average density. Thermodynamic equilibrium holds as density is at its minimum at a given temperature. Cahn and Hillard found that [21]

$$\Psi[\rho(r)] = \int dr f_h[\rho(r)] - \mu * \rho(r) + k[\nabla\rho(r)]^2$$

Where Ψ is the grand-potential, ρ the average density, r the nanoparticle radius, f_h the free energy of a homogeneous system, μ the chemical potential and k describes a non local contribution to f_h .

Kinetic nucleation theory

The kinetic nucleation theory do not consider the constrained equilibrium of the classical one at values of entropy more than 1, but with a stable equilibrium at entropy equal to 1 [22]. The passage between condensation and evaporation is described by

$$c_1 - c_{n-1} \leftrightarrow c_n$$

Where n indicates a n -mer. Let write the rate of growth as

$$J_n = \xi a_{n-1} c_{n-1} - E_n c_n$$

With ξ that expresses the monomer flux to the interface from the ideal gas kinetic theory

$$\xi = c_1 * \sqrt{kT/(2\pi m)}$$

And

$$E_n = \xi^e a_{n-1} \frac{c_{n-1}^e}{c_n^e}$$

With ξ^e the monomer evaporation coefficient from the equilibrium condition $J_n = 0$.

The following formulas stand:

$$\frac{J_n}{\xi a_{n-1} c_{n-1}^e} = \frac{c_{n-1}}{c_{n-1}^e} - \frac{\xi^e c_n}{\xi c_n^e}$$

$$\frac{\xi^e}{\xi} = \frac{1}{S} = \left(\frac{c_n}{c_n^e}\right)^{-1}$$

$$c_n^e = N e^{-\left(\frac{\Delta G(n)}{kT}\right)}$$

$$H(n) = \ln(\xi a_n c_n^e S)$$

$$J = \sqrt{\frac{H''(n)}{2\pi}} e^{H(n)}$$

Where N is a normalization constant and c is linked to the Boltzmann statistic.

In the case of classical theory of nucleation the equation below is not satisfied for $n = 1$

$$\frac{\Delta G}{kT} = \frac{\gamma}{kT} * n^{2/3} - n * \ln S$$

This situation is not very interesting, since the values of n that are meaningful around n^e . Kinetic theory of nucleation overcomes this difficulty, as for $S = 1$:

$$\frac{\Delta G}{kT} = \frac{\gamma}{kT} * n^{2/3}$$

However, the results for n^e are the same for both theories. What changes is J :

$$\frac{J_{KNT}}{J_{CNT}} = \frac{1}{S} * e^\gamma$$

It has to be stressed that γ itself is linked to temperature.

Coalescence

In a homogenous process of nucleation it is possible to distinguish four different situations, as described in the Figure 6-1:

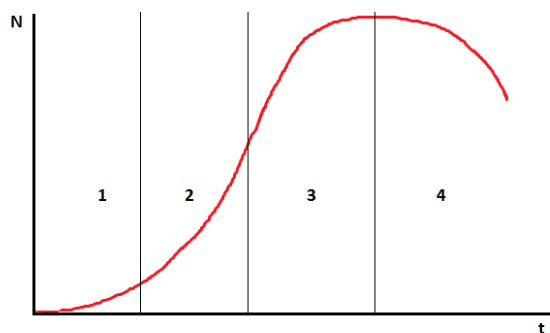


Figure 6-1

1. Incubation: the number of nuclei grows very slowly with the passing of time;
2. Stationary: the rate of growth is almost constant: $\dot{N} \sim k$;
3. Slowing down: the number of nuclei starts to lower and the previously formed entities become bigger and bigger;
4. Coalescence: already present nuclei start to melt together.

The coalescence process occurs when particles arrive on the substrate too. Once there, nanoparticles move due to the thermal effect. Their motion should be something similar to a Brownian one and depends on their temperature and the kind of substrate, if it is amorphous or crystalline, for example.

It was found that the union of two islands is an exothermic reaction, so that the heat produced during the process rises the nanoparticles temperature itself, feeding the melting more and more particles. It is clear that this phenomenon put an inferior limit to the minimum nanoparticles size.

Much direct and indirect evidence have been found in these years in order to prove the coalescence process. One of the most convincing is the decrease of the number density of nanoparticles during the deposition. In any case, the classical model, according to which island growth is thought to be led by monomers deposition, then followed by migration and coalescence with other growing particles, presents some questionable assumptions, as the fact that particles composed by more than a single monomer do not migrate on the surface [23]. Another process that must be understood better is the relation between coalescence, migration and new material deposition: two ways are possible, maybe both (Figure 6-2).

According to the first, particles melting is due to the growth, the second one, instead, focuses on the islands motion.

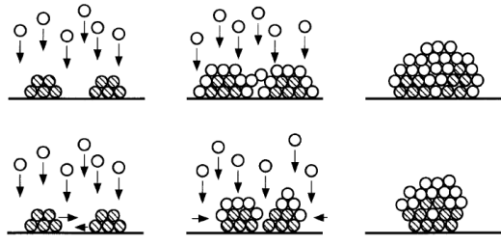


Figure 6-2

CHAPTER VII. Devices used

SEM

A Scanning Electron Microscope is an instrument able to show images of objects with sizes around nanometres, reconstructing the signals produced by the interaction between a focused electron beam produced by the microscope and the sample.

High vacuum is needed when the instrument is in use.

History

The first SEM was developed by von Ardenne (Figure 7-1) in 1937, who obtained a microscope with high magnification by scanning a very small raster with a demagnified and finely focused electron beam.

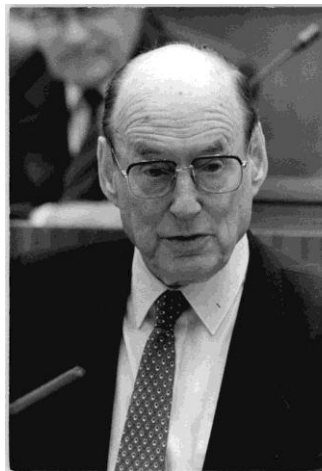


Figure 7-1

Further works and advancements were led by Cambridge's group in 1950s and 1960s which finally made possible the marketing of the first commercial instrument: the "Stereoscan" (1965) [24].

General features

The probe used by the device is a beam of electrons produced by thermionic effect that occurs in a metal filament heated by Joule's effect through the passage of current. Typically, the material used is tungsten,

since it has the highest melting temperature and the lowest vapour pressure of all metals. A more performing but also expensive alternative is represented by lanthanum hexaboride.

Once produced, electrons are accelerated and focused by a system of magnetic lens that results in a spot about 0.4 to 5 nm in diameter. Typically the final ones deflect the beam in the x and y axes so that it scans over a rectangular area of the sample surface.

Primary electrons, shot by the microscope (schematically shown in Figure 7-2), interact with the sample surface within a volume whose shape has the form of a pear and it extends from less than 100 nm to about 5 μm on the surface. The extension of this zone depends on the electrons energy and the sample atomic number and density. Electrons interact with the object with numerous and repeated scattering events, so that different kinds of electrons are produced: high energy ones undergo elastic scattering and are reflected, while secondary electrons are the result of inelastic scattering. From the dropping out of excited electrons X rays are produced.

Each signal is analyzed by a specific detector, always linked to an electronic amplifier that makes possible for an opportune software to produce a picture. Each pixel represents a zone of the detector sensitive area and its brightness is proportional to the intensity of the signal, whose value is linked to the number of electrons hitting the device.

Secondary electrons (SE), originated in the most external nanometres of the sample, are detected by a system which couples a scintillator and a photomultiplier. SE are first collected by attracting them towards an electrically biased grid, and then further accelerated towards a phosphor or scintillator positively biased. Now they have an energy sufficient to make the scintillator emit a flash of light (a phenomena called cathodeluminescence), which excites the photomultiplier, usually positioned outside the SEM column.

The formerly described detector is inefficient for the detection of high energy elastic scattered reflected electrons because the positively biased detection grid has little ability to attract them. Dedicated backscattered electron (BSE) detectors are positioned above the sample in a "doughnut" type arrangement, concentric with the electron beam, maximizing the solid angle of collection. BSE detectors are usually either of scintillator or of semiconductor types. When all parts of the detector are used to collect electrons symmetrically about the beam, atomic number contrast is produced: heavy elements backscatter electrons more strongly than light ones and thus appear brighter in the image. However, strong topographic contrast is produced by collecting back-scattered electrons from one side above the specimen using an asymmetrical, directional BSE detector.

X-rays are detected via apposite sensors which exploit techniques like EDS (energy dispersive X-ray spectroscopy) or WDS (wavelength dispersive X-ray spectroscopy).

The spatial resolution of the SEM depends on the size of the electron spot, which in turn depends on both the wavelength of the electrons and the electron-optical system that produces the scanning beam, and of the volume of interaction. They are both large compared to the distances between atoms, so SEM resolution is not high enough to image individual atoms. However it has compensating advantages like the ability to image a comparatively large area of the specimen; the ability to image bulk materials (not just thin films or foils); and the variety of analytical models available for measuring the composition and properties of the specimen.

Magnification is independent from the system of lens adopted and results from the ratio of the dimensions of the raster on the specimen and on the display device. Assuming that the display screen has a fixed size, higher magnification can be produced reducing the size of the raster on the specimen. Magnification is therefore controlled by the current supplied to the x, y scanning coils, or the voltage supplied to the x, y deflector plates, and not by objective lens power. Moreover, it can vary between several orders of magnitude.

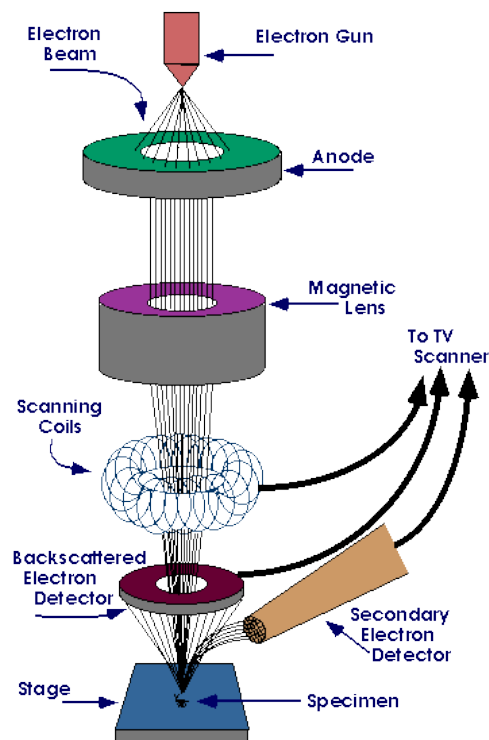


Figure 7-2

Experimental setup

The SEM used during this work is a *Cambridge Stereoscan 360*, able to create the electrons from the heating of a tungsten filament and accelerate them thanks to a 40 keV potential. This device can detect secondary electrons, with energies lower than 50 eV, a volume of interaction 1 μm deep and a path inside the sample of length between 3 nm and 10 nm. Backscattered electrons are revealed by the machine, but this ability has not been exploited, due to its poor spatial resolution. *Cambridge stereoscan 360* can also determine the atomic structure of the sample, distinguishing the energy of the photons emitted by the atoms during the dropping out of the electrons, after the interaction with the electronic beam.

TEM

Transmission electron microscopy is a microscope technique able to create images of nanometric samples, interpreting the result of the interaction between an electronic beam and an ultrathin specimen, collected on an opportune device.

As for SEM, very low pressures are necessary to the correct instrument working.

History

TEM history starts with the birth of quantum mechanics, since the use of electrons as probe became reasonable after De Broglie's theory. The first TEM was created by Max Knoll and Ernest Ruska (showed in Figure 7-3) in 1931 and just two years later a TEM with higher resolution than the one of optic microscopes was produced [25]. In 1939 TEM became a commercial device.

A further result was acknowledged in the 70s when field emission gun TEM was developed by Crewe at the University of Chicago [26]. In 2008, Jannick Meyer described the direct visualization of light atoms such as carbon and even hydrogen put on a single layer grapheme substrate [27].



Figure 7-3

General features

As for SEM, the probe consists in an electron beam produced by thermionic effect by a metallic filament heated by the passage of an electric current. As mentioned before, the most common material used as filament is tungsten, even if hexaboride lanthanum reaches better performances, but its widespread use is limited by cost.

Once extracted, the upper lenses of the TEM (whose structure is shown by Figure 7-4) permit the formation of the electron probe to the desired size and location for later interaction with the sample. The electron beam can be controlled by the presence of an electromagnetic field: the application of high voltages make possible for the electrons to accelerate and acquire energy, while magnetic fields generated by coils called magnetic lens modify their orientation.

Typically a TEM has three kinds of lens: condenser lenses, objective lenses and projector ones. The first are responsible for primary beam formation, while the second ones focus the beam that comes through the sample itself. The projector lenses are used to expand the beam onto the phosphor screen or other imaging device. The magnification of the TEM is due to the ratio of the distances between the specimen and the objective lens' image plane.

Another important part of the device is the one which permits to insert the sample into the TEM and to move it. TEM specimen stages are designed in order to minimize air entrance in the microscope. Sample holders are adapted to hold a standard size of grid upon which the sample is placed or a standard size of self-supporting specimen. Usual grid materials are copper, molybdenum, gold or platinum. This grid is placed into the sample holder, which is paired with the specimen stage. Once inserted in the device, the sample can be moved in order to study different zones and to focus the image. It is possible to do that both in the XY plane and in the Z axis. Also rotations are permitted.

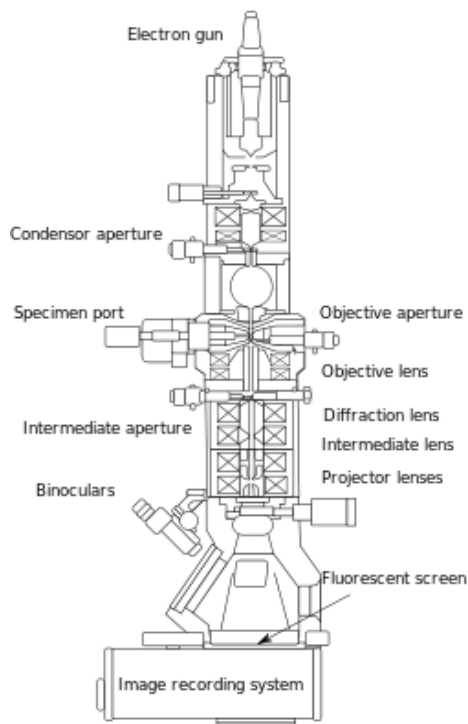


Figure 7-4

TEM images are created interpreting the information included in the electronic wave functions exiting the sample. As mentioned before, the projector lenses aid focusing the image on the appointed device. The intensity of the observed image can be approximated by a temporal average of wave functions amplitude:

$$I = \frac{k}{t_1 - t_0} \int_{t_0}^{t_1} \Psi^* \Psi dt$$

It is clear that intensity I does not depend only on the wave amplitude, but also on its phase. Different imaging techniques modify the beam in order to obtain the desired information. To obtain high resolution images, it is necessary to have the thinnest sample possible, so that it cannot be treated it as an absorbing object, subjected to Beer's law. There are different methods to produce an image by TEM and each of them brings different information.

The most common mode of operation is the bright field imaging mode, in which the contrast is formed by absorption of the electrons in the sample: thicker regions or zones characterized by an higher atomic number appear darker than others. The image is considered as the two dimensional projection of the sample and a first analysis can be done exploiting Beer's law.

Diffraction contrast is a technique based on the fact that the electron beam may undergo Bragg scattering, by which the crystalline sample disperse electrons into discrete locations. Bragg reflections can be selected to study only the part of the sample that causes the electrons to scatter. Modern TEMs are equipped with sample holders that are able to tilt the specimen to a range of angles that makes possible to obtain specific diffraction conditions.

Utilizing the advanced technique of electron energy loss spectroscopy, present in TEMs appropriately equipped, electrons can be distinguished upon their energy, using EELS spectrometers. These devices allow for the selection of particular energy values, which can be associated to the way the electron has interacted with the sample. EELS spectrometers can often be operated in both spectroscopic and imaging modes, allowing for isolation or rejection of elastically scattered beams.

Crystal structure can also be investigated by high-resolution transmission electron microscopy (HRTEM), also known as phase contrast. When utilizing a field emission source and a specimen of uniform thickness, the images are formed due to differences in phase of electron waves, which is caused by specimen interaction. So the image is not only dependent on the number of electrons hitting the screen, making direct interpretation of phase contrast images more complex. However this effect can be used as an advantage, as it can be manipulated to provide more information about the sample.

Experimental setup

TEM measurements were performed at IMM (Istituto di Microelettronica e Microsistemi) of the CNR in Bologna. The device used was *Field-Emission Gun Tecnai F20 Super-twin* equipped with EDAX energy-dispersive X-ray spectrometer (EDS), Gatan Electron energy loss spectrometer (EELS) and Scanning TEM attachment (STEM).

XRD

History

X-rays were discovered by Wilhelm Conrad Röntgen in 1895. Then, a dispute was born among physicists in order to define X rays nature. Finally, they were recognized as an electromagnetic wave, so a particular kind of light, since between the end of the XIX century and the beginning of the XX century the predominant conception of light was the one derived from Maxwell's view. It was accepted later that X rays, such as any

radiation, have also a particle-like nature, being made up of photons. Sommerfield's group found that X ray wavelength was about 10^{-10} m, a characteristic needed to make diffraction happen. The theory of this phenomenon was developed by Bragg in 1912, also known as elastic scattering theory [28].

General features

X ray diffraction (XRD) is a widely diffused investigation technique of crystal structures. When an X ray beam hit the sample, it undergoes diffraction due to the particular periodic structure of the crystal. The result of this phenomenon is collected on specific films that show a two dimensional image. Thanks to Fourier transformation and the theory of diffraction, it is possible to derive the three dimensional crystal structure.

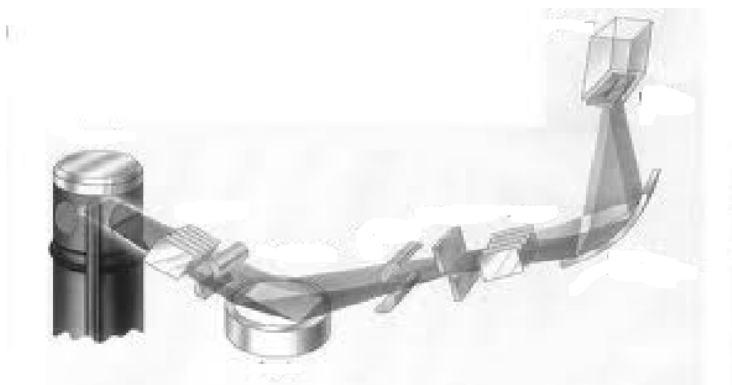


Figure 7-5

X rays can be produced by synchrotron or by diffractometer (Figure 7-5). The former creates the brightest X rays, a feature that makes them have an astonishing resolution. Their principal limit is represented by the fact that they are very expensive and large, for this fact they are usually national facilities with several beam lines, each of them performing a different measure. Diffractometers, smaller, cheaper but less performing than synchrotrons, accelerate electrons with high electric potentials and make them hit atoms. Their inner electrons are excited and leave the atom. The filling of the hole so created by another electron creates a X ray.

X rays are generally filtered to a single wavelength, making it monochromatic, and collimated to a specific direction, before hitting the sample.

Bragg proposed his simple but right theory about diffraction in 1912. Suppose that the incoming waves are reflected symmetrically by the crystal atomic planes, where each one reflects just a very little fraction of the radiation. Diffraction is observed when reflections interfere constructively. Consider parallel planes separated by the same distance d (hkl are the relative Miller's indices) as in Figure 7-6. The difference of path between adjacent planes is $2d_{hkl} \sin \vartheta$ where the angle is the one shown below.

Constructive interference occurs when the difference of path equals an integer multiple of the distance d :

$$2d_{hkl} \sin \theta = n\lambda$$

If every plane had reflected perfectly, then just the first one would have interfered with the wave. On the contrary, each plane reflects just from 10^{-3} to 10^{-5} of the total radiation, so, in a perfect crystal, the number of the planes that take part of the phenomenon varies between 10^3 and 10^5 .

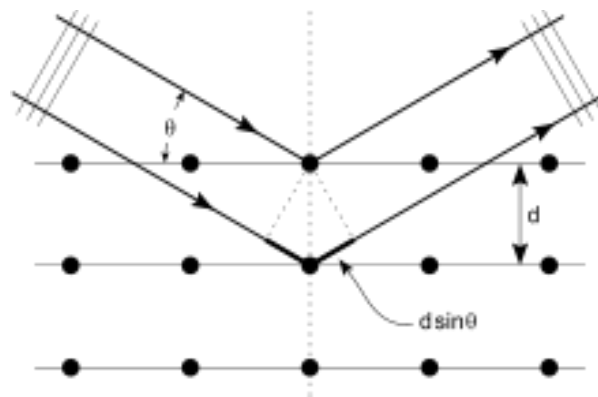


Figure 7-6

Bragg's law is linked to the theorem which states that the \mathbf{G} vectors, the ones connecting two points of the Fourier's space, determine the possible X rays reflections (Figure 7-7). The amplitude of the diffused wave is

$$F = \int dV n(\mathbf{r}) \exp[i(\mathbf{k} - \mathbf{k}')\mathbf{r}] = \sum_{\mathbf{G}} \int dV n_{\mathbf{G}} \exp [i(\mathbf{G} - \Delta\mathbf{k})\mathbf{r}]$$

Where $n(\mathbf{r})$ is the electronic density, $n_{\mathbf{G}}$ its Fourier transformation, \mathbf{k} and \mathbf{k}' , respectively, the incident and diffused wave vectors, $\Delta\mathbf{k}$ their difference and V the sample volume. When the vectors difference and \mathbf{G} are equal, F is different from zero.

The connection between the two approaches is that $d_{hkl} = 2\pi/|\mathbf{G}|$.

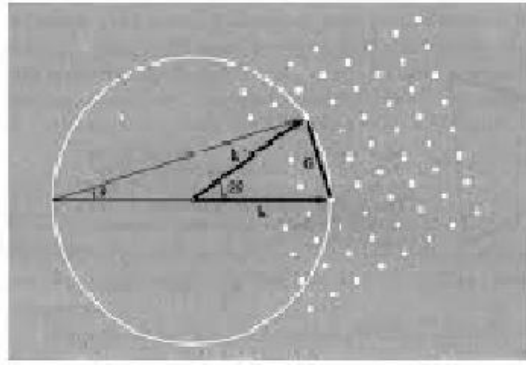


Figure 7-7

When a crystal is mounted and exposed to an intense beam of X-rays, it scatters the X-rays into a pattern of spots of reflections that can be observed on a screen behind the crystal. The relative intensities of these spots provide the information to determine the arrangement of molecules within the crystal in atomic detail. The intensities of these reflections may be recorded by a photographic film, an area detector or by a charge-coupled device (CCD) image sensor. The peaks at small angles correspond to low-resolution data, whereas those at high angles represent high-resolution data; thus, an upper limit on the eventual resolution of the structure can be determined from the first few images.

One image of spots is insufficient to reconstruct the whole crystal; it represents only a small slice of the full Fourier transform. To collect all the necessary information, the single crystal must be rotated step-by-step through 180° , with an image recorded at every step.

Isolating a single monocrystal is a complicated operation, since it is easier to study a polycrystalline sample or a powder of it. In these cases, crystals are oriented randomly in all directions, so the results are diffractions cones, as the monocrystal was rotated uniformly.

In three dimensional space, a point P is defined by the three Miller's indices h_p, k_p, l_p ; if the crystal is rotated uniformly, the vector d of the reciprocal space associated to the three indices describes a sphere centred in the origin and with a radius equal to the vector modulus. That sphere intercepts the Edwald's one, forming a cone of aperture 2ϑ , called Scherrer cone. The single point P determines a unique angular aperture $2\vartheta_p$ but all its possible orientations draw a cone whose circumference is given by the interception with the imaging film.

In general, an ideal crystallites distribution generates a series of cones with the same origin, each one associated to a single point. The imaging device presents different concentric circumferences.

Then, the diffraction pattern of a polycrystalline sample is determined by both the diffraction angle and the intensity of the diffracted ray. Each (h_p, k_p, l_p) circumference can be pointed by two parameters: $2\theta_p$ and I_p^{TOT} , as Figure 7-8 shows. All the points with orientation equal to the one of the point P give their contribution to I_p^{TOT} .

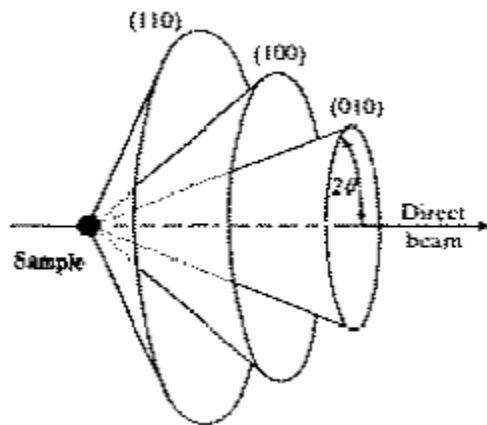


Figure 7-8

The diffraction image is a squeezing of the three dimensional crystal in the one dimensional space of 2θ (Figure 7-9). Each diffraction peak is linked to the reciprocal space point and, for this reason, it is possible to link it to a combination of Miller's indices. Generally, it may happen that some orientation is not statistically relevant, so the peaks intensity is not totally trustful. This problem can be partially resolved increasing the number of crystallites.

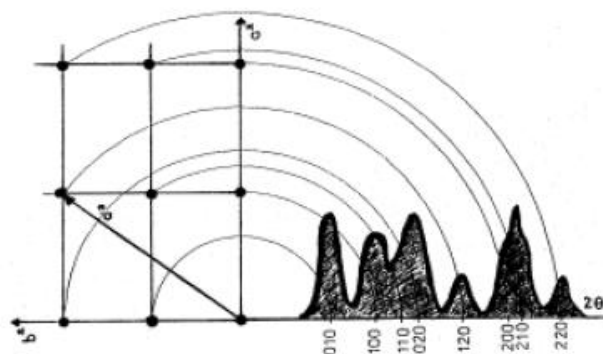


Figure 7-9

Experimental setup

The diffractometer used in this work is *PANalytical X'Pert Pro* that exploits the Bragg-Brentano geometry and uses as X ray source a Cu anode whose wavelength is 1.54 Å.

Generally a graph produced by an opportune software linked to the instrument plots the number of diffracted photons versus 2ϑ . The so built diffractogram is analysed by the Rietveld method that connects the collected intensity to some structural parameters, according to

$$I_i^{calc} = \sum_{j=1}^{Nphases} S_{Fj} \sum_{k=1}^{Npeaks} L_k |F_{kj}|^2 S_j(2\theta_i - 2\theta_{kj}) P_{kj} A_j$$

S_{Fj} depends on the incident wave intensity and on the cell volume, L_k is the Lorentz polarization factor which is linked to geometrical parameters as the beam dimension and the sample position, A_j is the absorption factor, P_{kj} depends on the presence of preferential orientations in the sample, F_{kj} is the Debye-Waller factor and $S_j(2\theta_i - 2\theta_{kj})$ determines the peak form.

The high number of variables on which the diffractogram depends makes necessary the use of an opportune software for its analysis: MAUD was chosen for this task [29].

CHAPTER VIII. Samples morphologic characterization

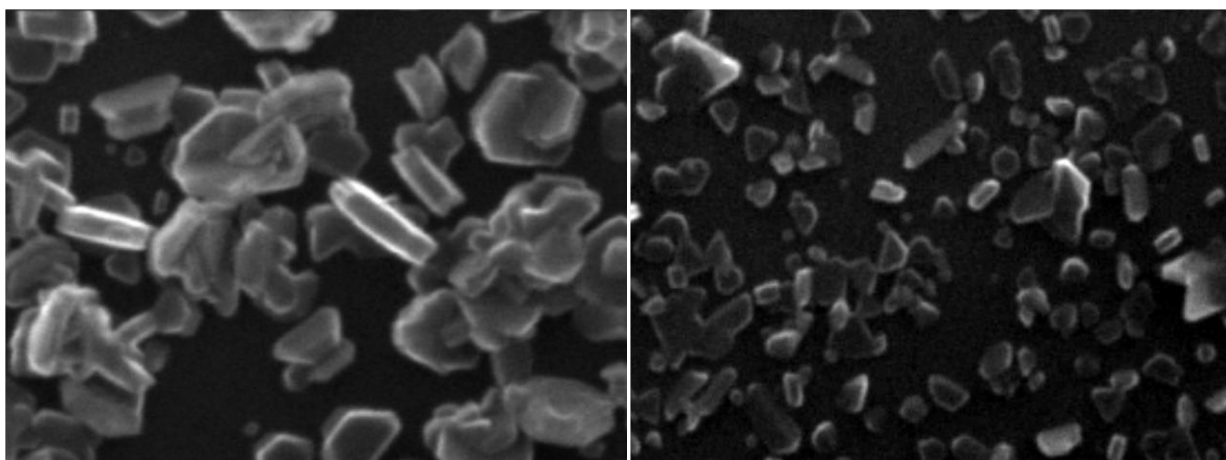
The kinetics of hydrogen absorption and desorption and the enthalpy involved in the processes can be modified by adjusting the nanoparticles size. In this paragraph the most significant samples are shown together with their relative SEM images. All samples were produced by IGC while the chamber pressure was around 2 torr, in a helium atmosphere. The inert gas flow was of 65 mln/s.

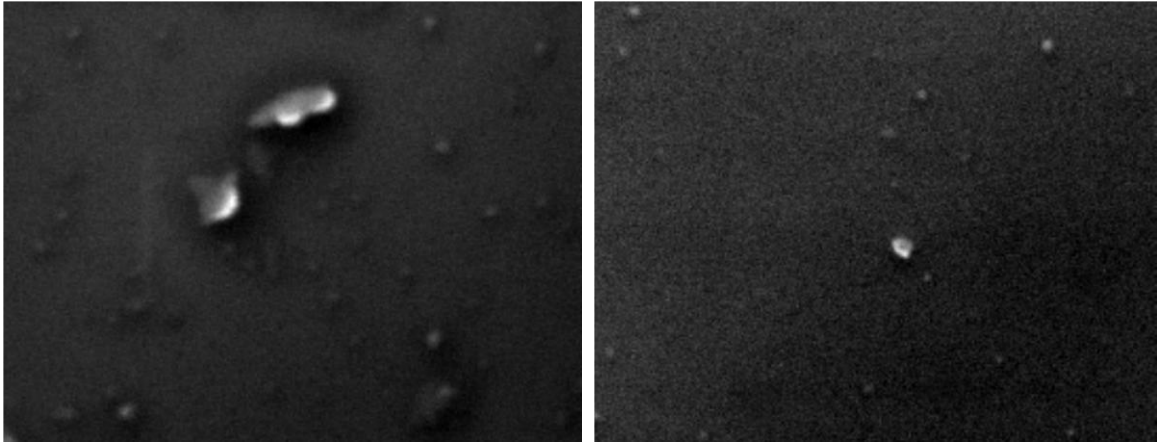
From pure Mg nanoparticles to Mg/MgO systems

MgO_87

The first attempt to form nanoparticles with a Mg core covered by a MgO shell is represented by MgO_87. After having created high vacuum, the oxygen needle valve was opened and closed very quickly, so that the pressure was of $4 \cdot 10^{-6}$ torr in the chamber. Then helium was inserted and the experiment went on as usual. The presence of the rotational pump let us think that the quantity of oxygen present lowered as time passed. According to SEM pictures it seems that this low O_2 quantity was not relevant in nanoparticles synthesis and they looked very similar to pure Mg ones.

Below pure Mg samples images are shown with deposition time of 5 minutes, 2 minutes, 1 minute and 30 seconds, respectively [30].





Increasing the deposition time makes the particles dimensions larger and larger and closer and closer to the typical hexagonal shape. An accurate study of the correlation between deposition time, particles sizes and the ratio between coverage and size is summarized in Figure 8-1 [30].

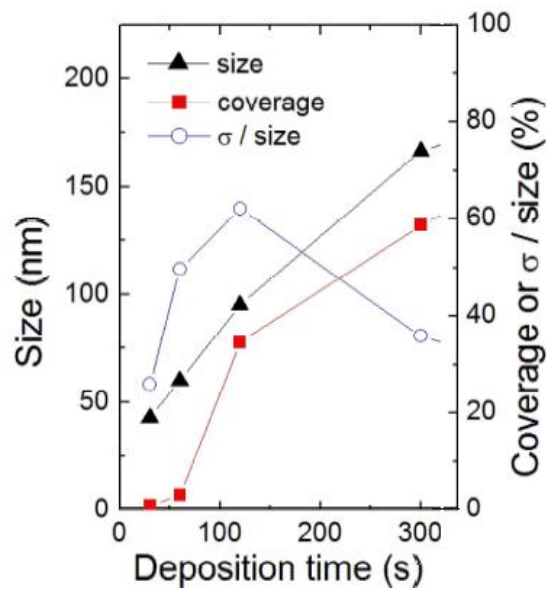
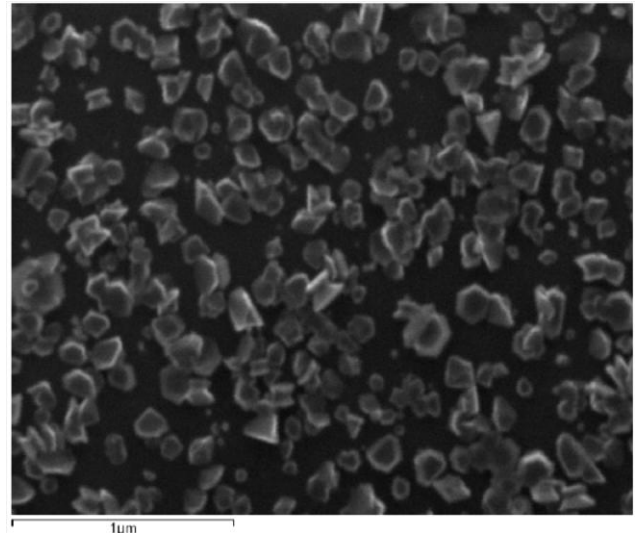
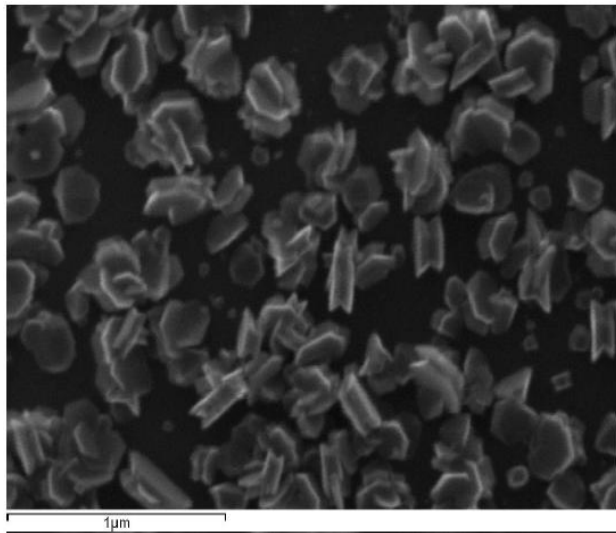


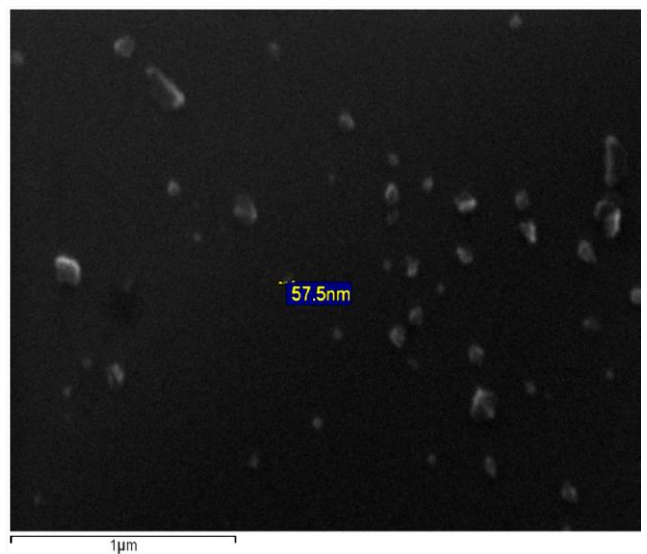
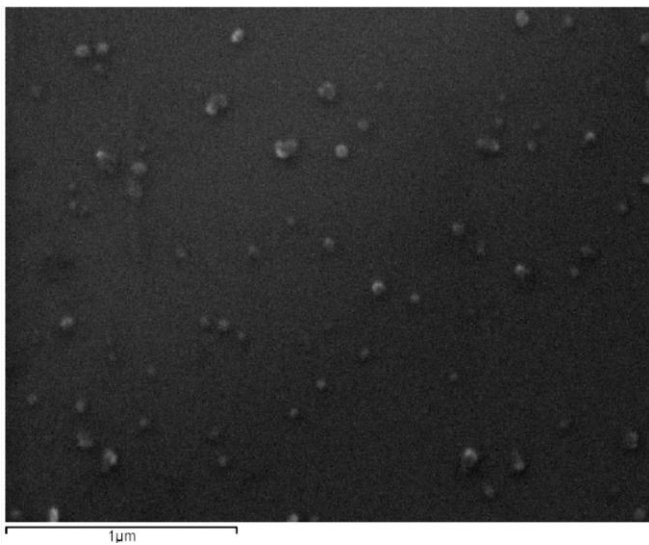
Figure 8-1

Four samples were synthesised and their outlook is be linked to the deposition time.

Time	5 min	Time	2 min
Thickness	5 nm	Thickness	3,5 nm



Time	1 min	Time	30 s
Thickness	2 nm	Thickness	1 nm



It appears clear that increasing deposition time makes nanoparticles bigger and bigger. As mentioned in *Coalescence* section, this result can be addressed to the union of bigger and bigger islands, to the union between previous islands thanks to the arrival of other material or to both the processes.

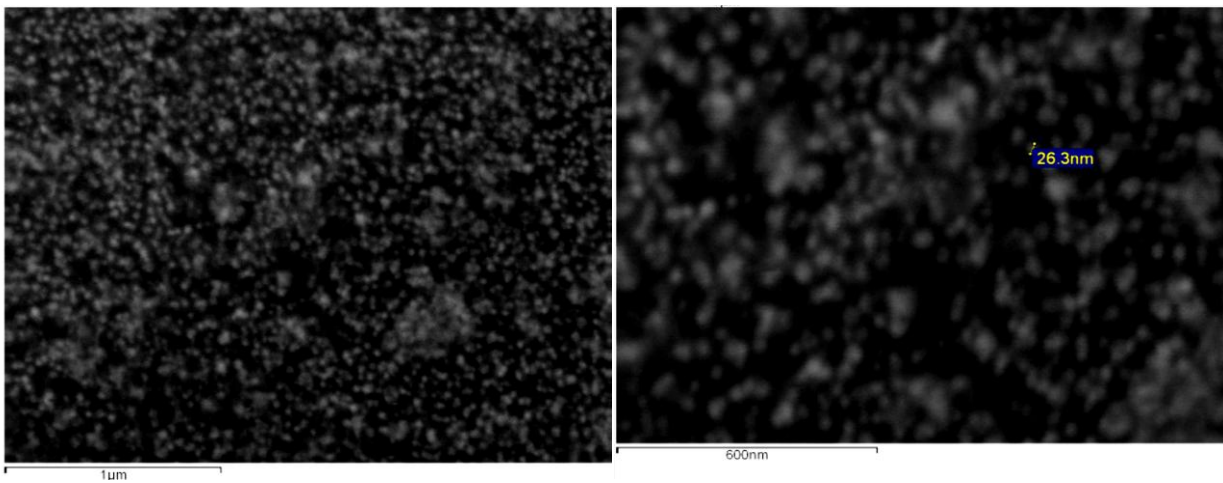
Moreover, while in the first sample the particles are all around 200 nm with a clear hexagonal structure, in the last most particles are around 60 nm of diameter.

MgO_88

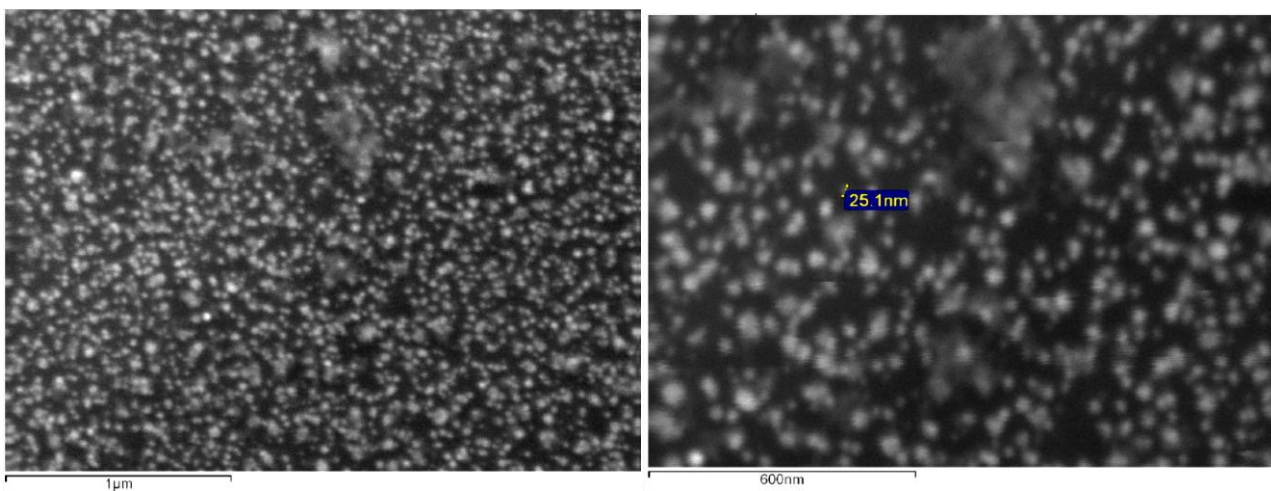
In order to be sure of the presence of a MgO shell, an oxygen flux was created and positioned so that it met the Mg particles before they got to the cylinder.

In this experiment O_2 flux was approximately 10^{-4} torr/s, equal to 0,015 mln/s.

Time	5'
Thickness	7,8 nm

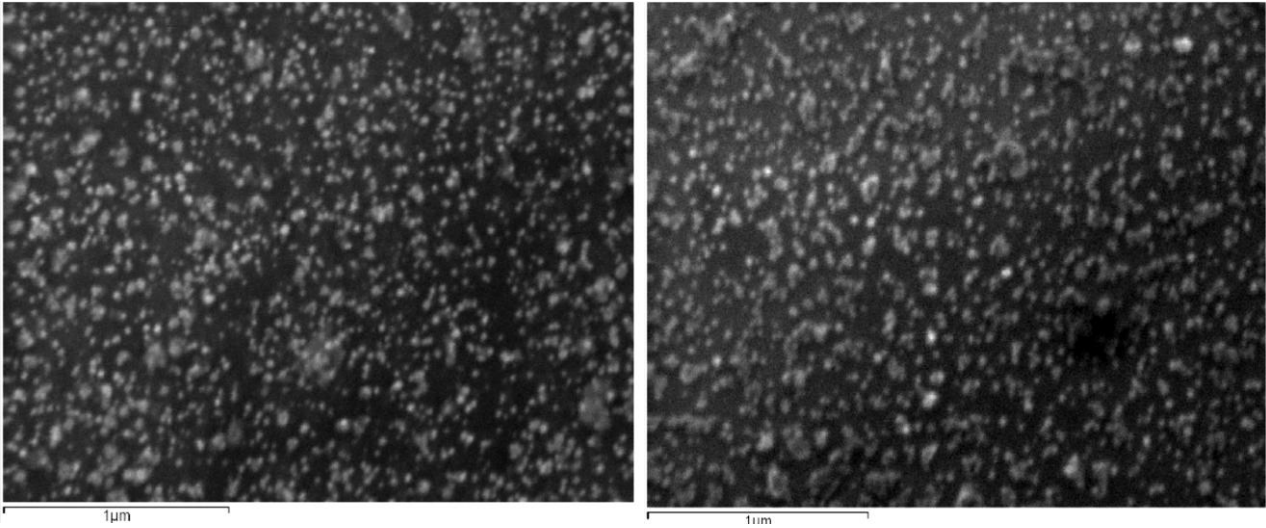


Time	2'
Thickness	3 nm

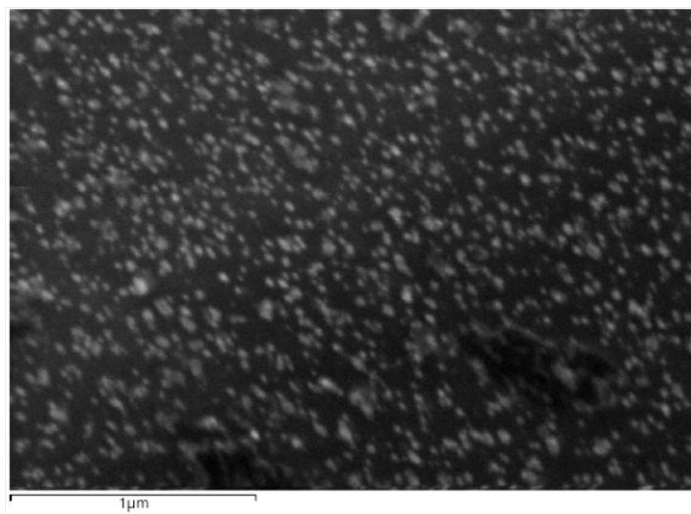


Time	1'
Thickness	1,2 nm

Two different zones can be distinguished watching the sample at SEM at low magnification: one clearer (on the right) and one darker (on the left). The difference is caused by the different amount of material present.



Time	30''
Thickness	0,7 nm



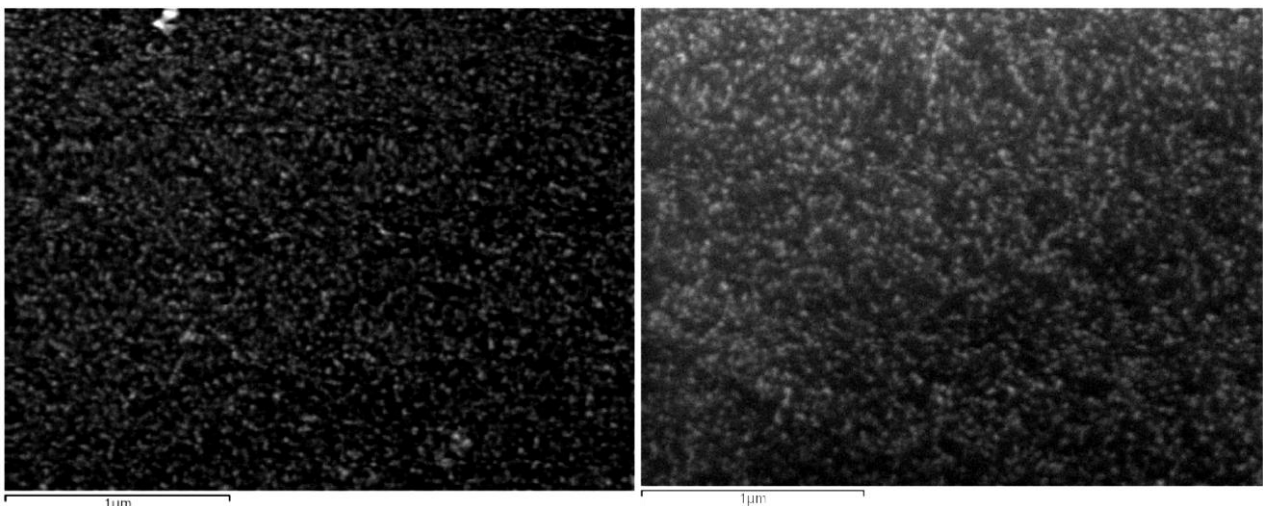
These samples are very different from the previous and demonstrate that it is possible to create very small particles covering Mg cores with MgO shells: some are found to have diameters around 20 nm. It is possible to hypothesize that the oxide shell limits the particles movement and/or the coalescence between islands. The evidence of that nanoparticles structure will be shown later. Obviously, the longer the deposition is the more numerous the nanoparticles are and the easier they get in contact: observing carefully the several "white" zones of the first two samples, they appear as agglomerates of single particles, not as bigger ones. The idea that the particles coalesce once they have arrived on the substrate is coherent with this remark and gives importance to the kind of substrate used in the experiment. Agglomerates can form with the arrival of more material too.

MgO_Pd_89

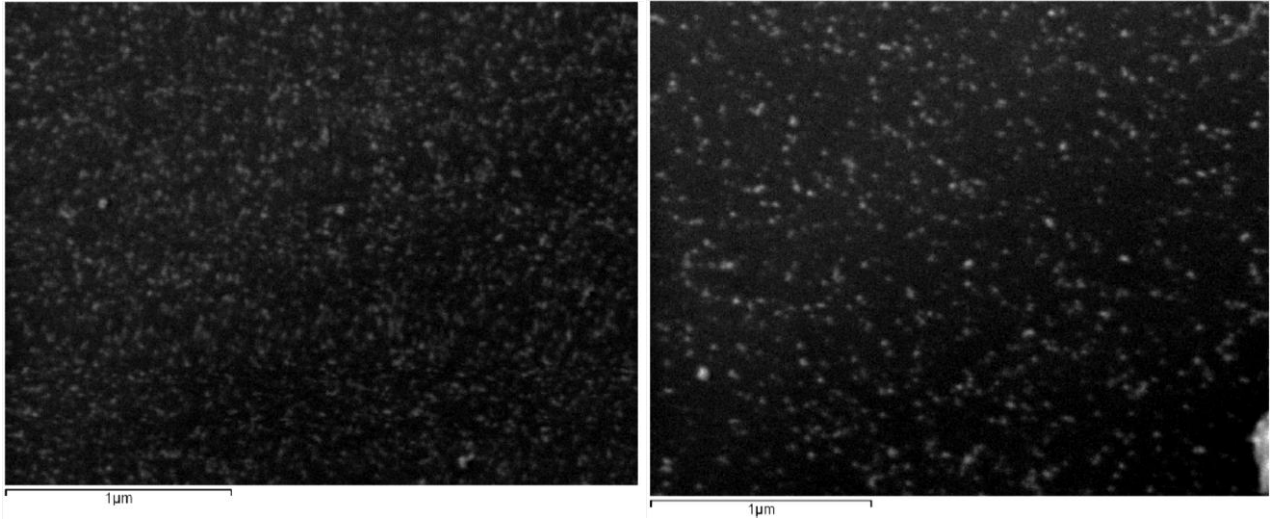
In order to understand the role of the substrate, this experiment differs from the previous one for the presence of a 5 nm thick Pd layer used as substrate, which had been deposited on silicon substrates before the Mg sublimation took place.

Palladium was heated by a 270 A current, magnesium by a 96 A one and O₂ flux was of 1,75 torr/s.

Time	5 min	Time	2 min
Thickness	6,9 nm	Thickness	1,5 nm



Time	1 min	Time	30 s
Thickness	0,8 nm	Thickness	0,7 nm



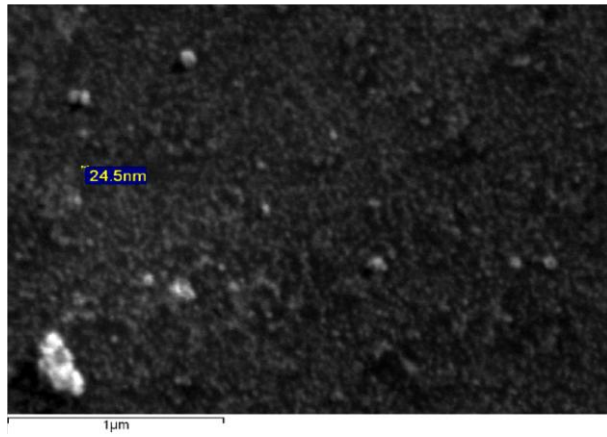
It could seem at a first look that the presence of Pd substrate limits the nanoparticles movement and, so, the melting probability. However, the quantity of material present could explain the difference respect to MgO_88 too. In order to understand more deeply the role of palladium, further experiments were performed.

MgOPd_98

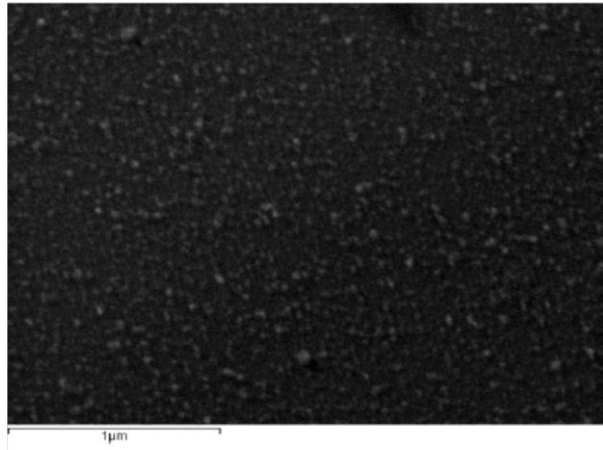
In order to grasp better the issue before mentioned it was chosen to differentiate the samples according to the role of palladium, having fixed the Mg evaporation time.

Palladium was sublimated by a 260 A current and magnesium by a 92 A one, oxygen flux was $8,85 \cdot 10^{-5}$ torr/s.

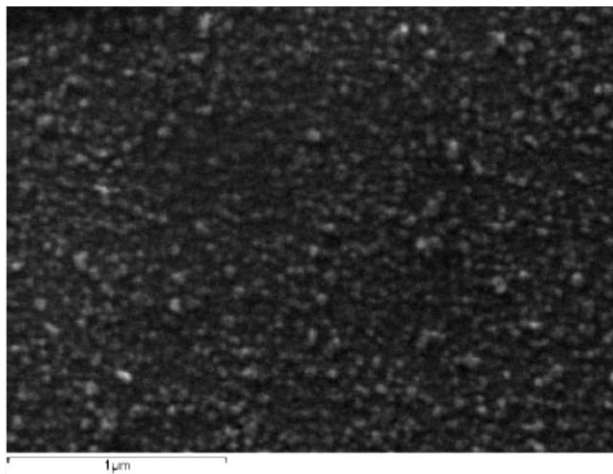
Time	2'
Thickness	4,9 nm
Palladium presence	Substrate



Time	2'
Thickness	5,5 nm
Palladium presence	Substrate and coating



Time	2'
Thickness	5,1 nm
Palladium presence	Coating



The experiment showed that the presence of Pd substrate does not change dramatically the disposition and the dimensions distribution of the nanoparticles respect to what happens when they are deposited on the usual silicon substrate. What appears of some relevance is the Pd coating: it betters the SEM images quality, being palladium a metal and so more sensible to the SEM electron flux, and seems to prevent the formation of nanoparticles clusters, blocking them in their arrival position. In this way the possibility of further nanoparticles movement, which may create agglomerates, is reduced.

These considerations appear valid but a central role must be attributed to the sublimation process and to the oxygen flux value.

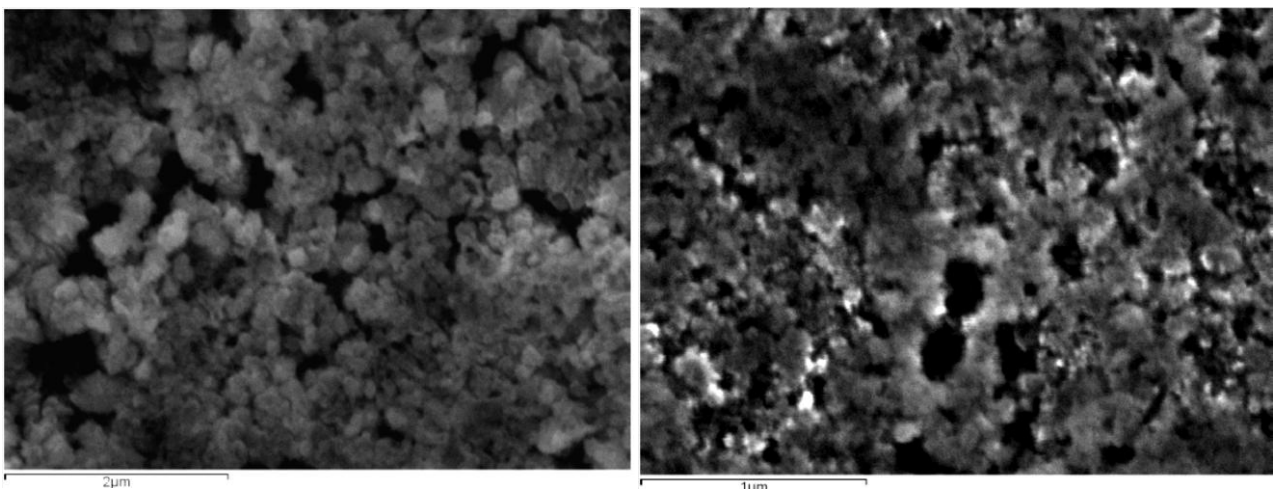
MgO_95

The following images are taken by a pellet made imposing a 98 MPa pressure for 30 seconds on the sample powder. The pellet surface appears smooth observing it by the naked eye but it is also evident that there are darker and lighter zones.

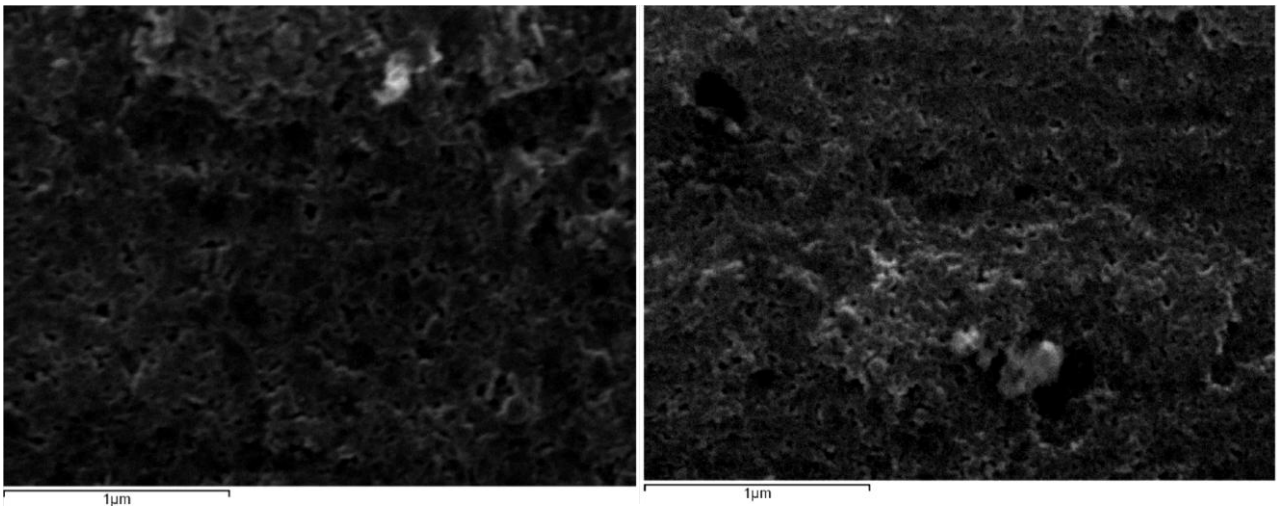
SEM analysis shows that the surface is rough: light zones present particles flakes, dark ones appear like terraces and the boundaries between the two different areas show the presence of nanoparticles.

Powders were produced collecting the material deposited on the cylinder, cooled by the liquid nitrogen. Magnesium was heated by a current of 114 A and the oxygen flux was about $1,39 \cdot 10^{-4}$ torr/s.

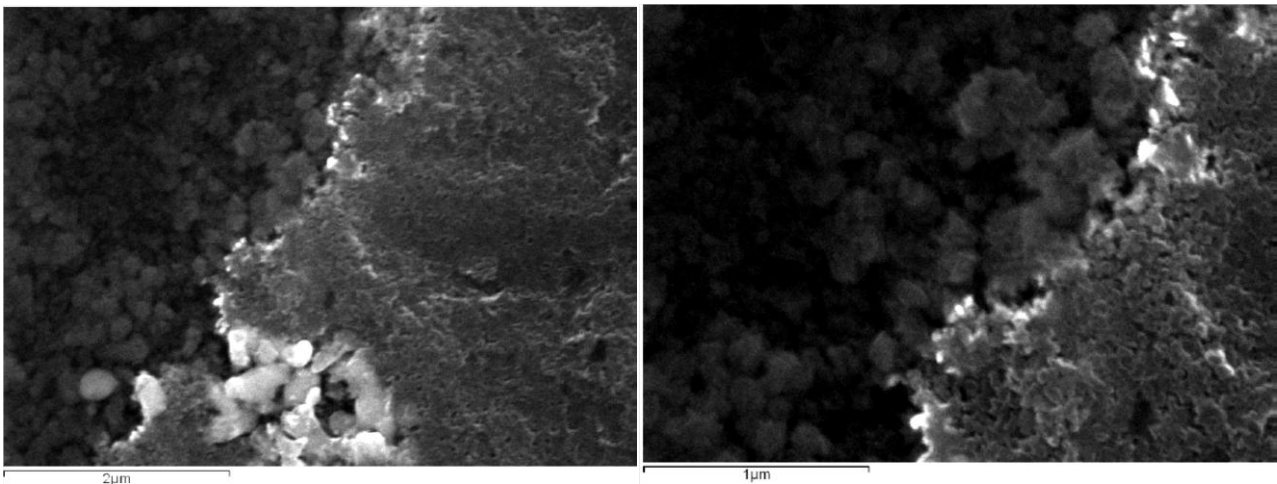
Lighter zone



Darker zone

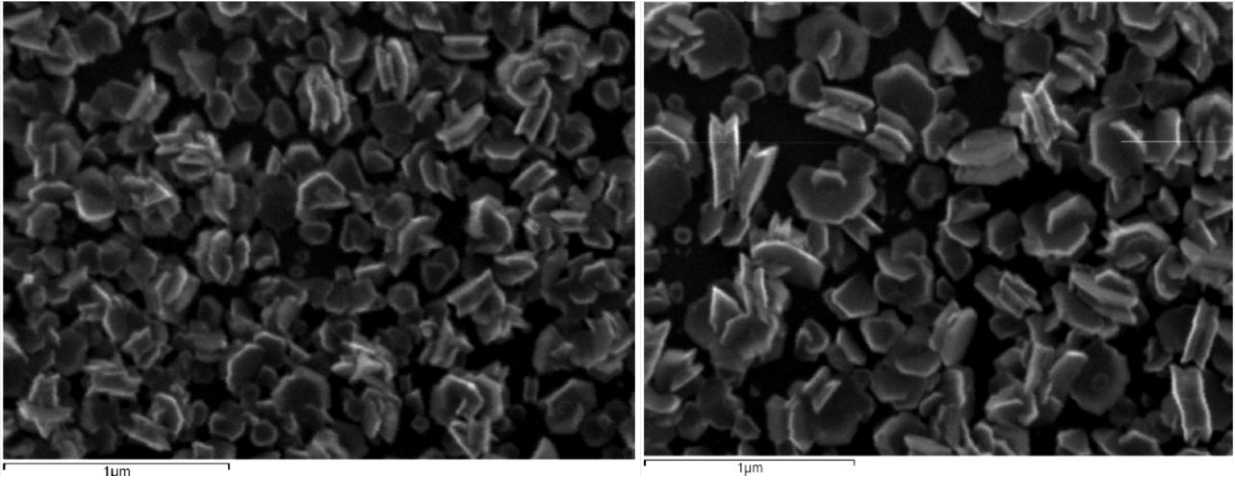


Boundary



While material was evaporated on the rotating cylinder, it was observed that two regions appeared on it, separated by an imaginary line which corresponded to the position of the oxygen flux. The zone under this line presented a colour varying between white and yellow, while the other one looked darker. In order to understand if morphologic and structural differences were present, in two experiments Si wafers were positioned one below this imaginary line and one above. Observing SEM images, it seems that bigger and less numerous nanoparticles covered the lower part of the cylinder, while the other one collected more material and smaller particles.

It is quite clear confronting the images of MgO_87: the one on the left comes from the upper part respect to the previously mentioned imaginary line, the one on the right from the other.



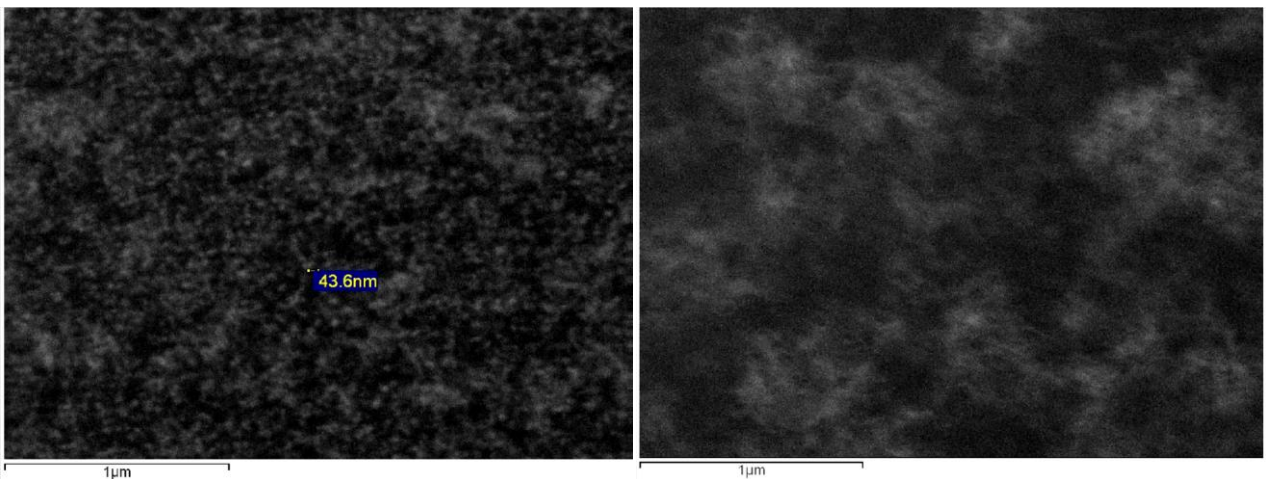
An entire experiment was dedicated to this problem: MgO_Pd_97.

MgO_Pd_97

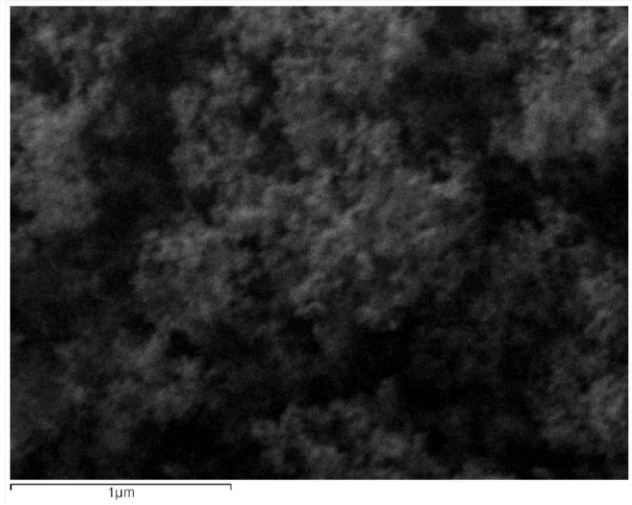
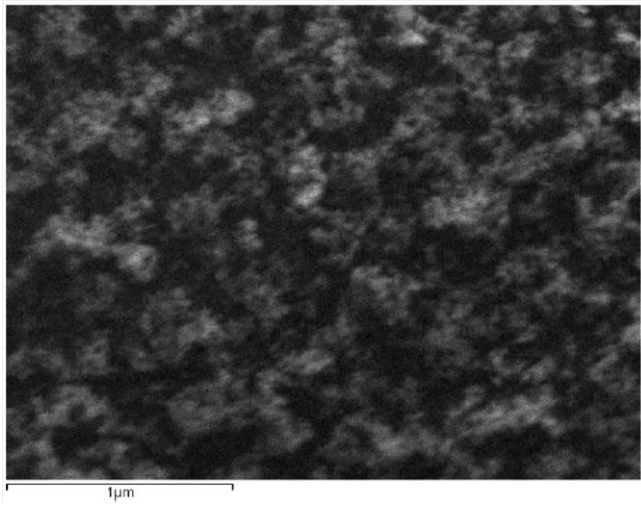
The images are ordered as follows: for each sample the one on the left is relative to the silicon present in the upper part, the one on the right is in the other. The last four images show nanoparticles covered by a 5nm thick Pd coating, the first four do not present this layer.

Palladium was sublimated by a 270 A current and magnesium by a 102 A one. The O₂ flux was of $1,4 \cdot 10^{-4}$ torr/s.

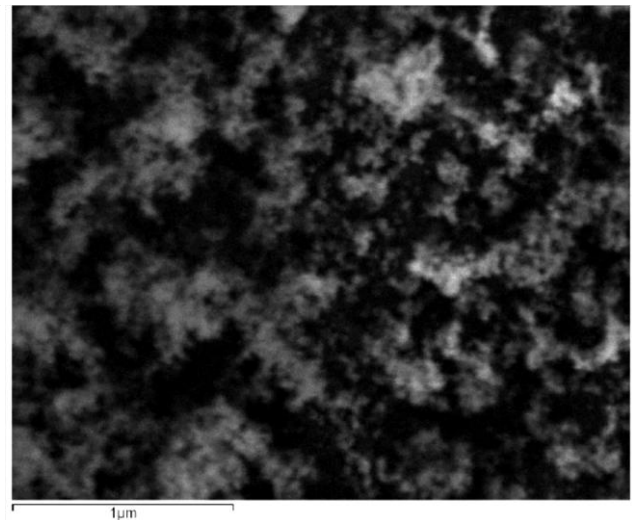
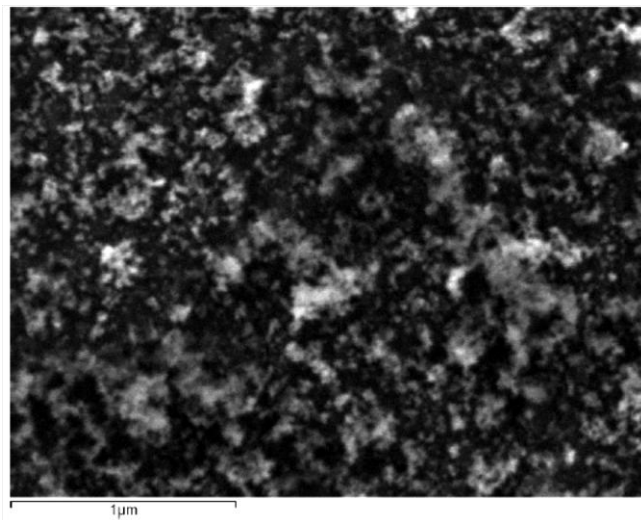
Time	5'
Thickness	6 nm



Time	5'
Thickness	9,5 nm



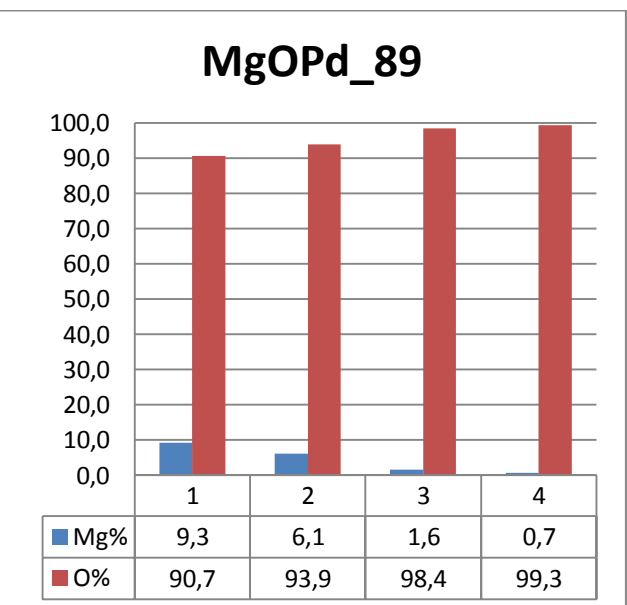
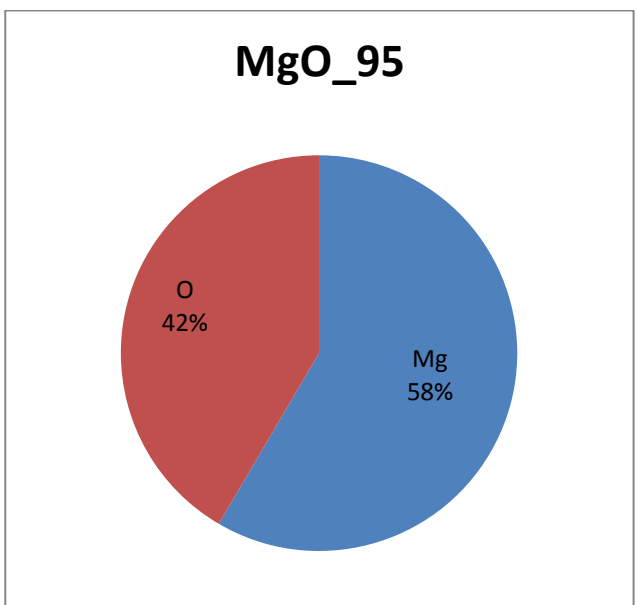
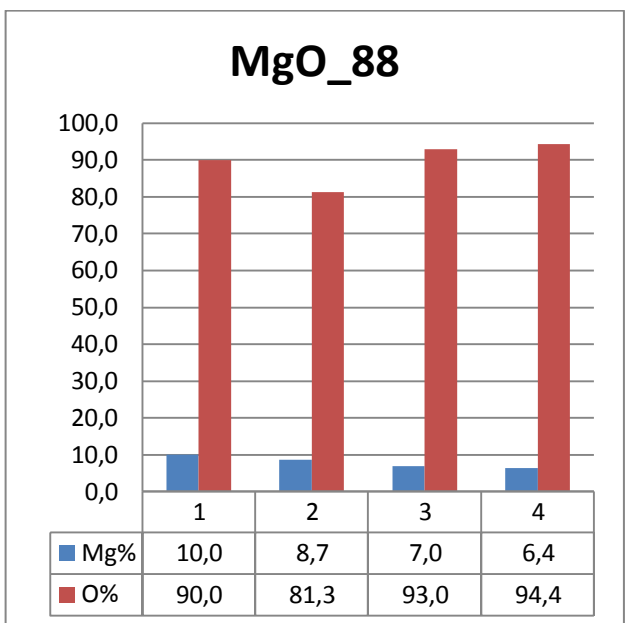
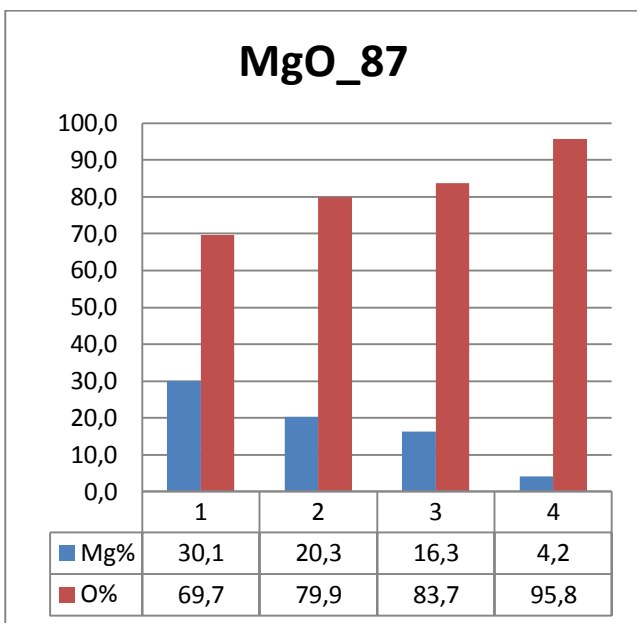
Time	1'
Thickness	2,7 nm

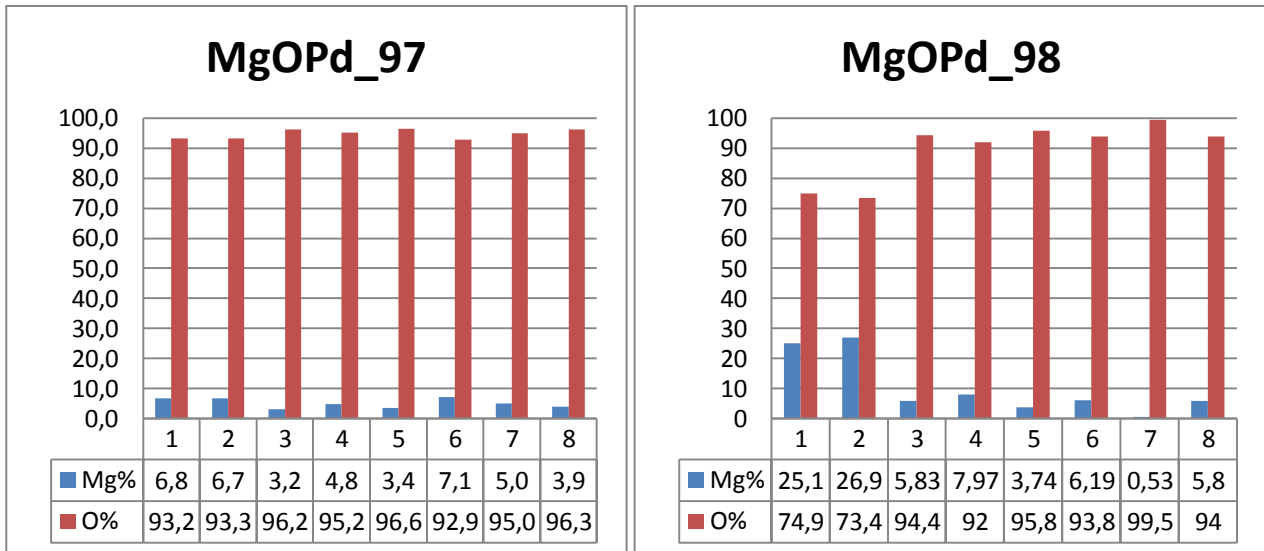


The presence of the Pd layer improves greatly the images quality: in the second sample the observation of nanoparticles results very hard due to charge effects as MgO is an insulator. In any case, it is possible to confirm what said before: the zone above the oxygen line experiences less agglomeration and smaller particles.

EDX results represent a semi-quantitative confirmation of what said before: histograms show that the magnesium relative abundance is linked to the sample exposition time to the particles flux and to the position of the silicon substrate, if above or under the oxygen flux line.

The large amount of oxygen is also linked to the presence of SiO₂ in the substrate. The percentages are relative to the atomic weight and the numbers 1, 2, 3 and 4 correspond respectively to the samples of 5 minutes, 2 minutes, 1 minute and 30 seconds of evaporation. As regards MgOPd_97 and MgOPd_98, 1, 2, 3, 4, 5, 6, 7, and 8 correspond to 5 minutes of evaporation upper part and lower part, 2 minutes upper part and lower part, 1 minute upper part and lower part and 30 seconds upper part and lower part.





XRD analysis

XRD analysis was performed in order to check the fact the nanoparticles created really showed both a metallic fraction a MgO one. Using MAUD program it was also possible to have an idea of the particles structure, as it can calculate the volumes fractions of Mg and MgO in the whole sample. Imaging the particles as spheres with a Mg core and an oxidized shell, as in Figure 8-1, it is possible to write:

$$\frac{4}{3} * \pi R_1^3 = x * \frac{4}{3} * \pi R_2^3$$

$$R_1 = \sqrt[3]{x} R_2$$

$$R_{MgO} = R_2 - R_1 = R_2(1 - \sqrt[3]{x})$$

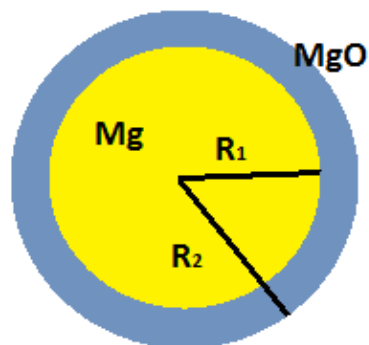


Figure 8-2

MgO_95

Palladium was sublimated by a 260 A current and magnesium by a 114 A one. The oxygen flux was $1,25 \cdot 10^{-4}$ torr/s.

This sample presents the requested structure and confirms the validity of the growth technique and the average particles diameter results to be around 36,65 nm, a good value respect to this work objectives.

Figure 8-3 comes from the pellet analysis, Figure 8-4 from material powders.

The passage from the weight percentages to the Mg core radius and MgO shell thickness is achieved exploiting MAUD calculations, geometrical considerations and the relation between mass, volume and density (Table 6). Of course, these data should be considered as simple estimates, since the nanoparticles have not a spherical shape, but a hexagonal one, as will be showed in the TEM analysis section. This explains the fact that $R_{Mg} + R_{MgO}$ is different from 36,65 nm

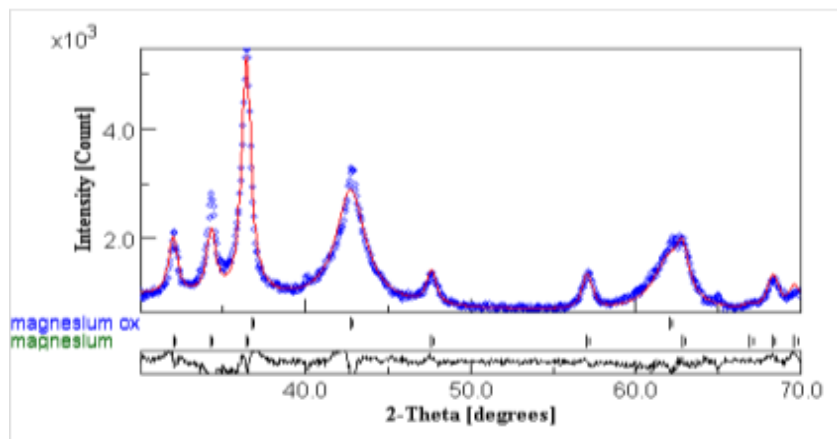


Figure 8-3

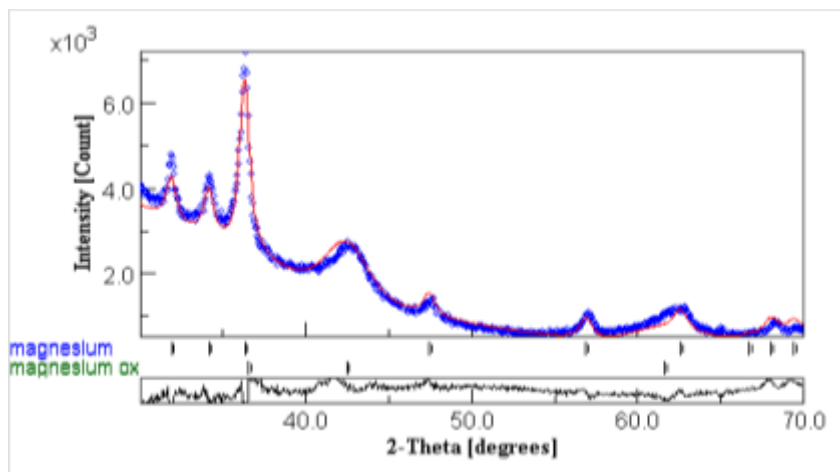


Figure 8-4

Table 6

MgO_95 powder	
Mg % (weight)	47,06
MgO % (weight)	52,94
$2R_{Mg}$ (nm)	29,77
$2R_{MgO}$ (nm)	14,63

MgO_93

Palladium was sublimated by a 260 A current and magnesium by a 110 A one. The oxygen flux was $2 \cdot 10^{-4}$ torr/s. In this case the spectrum is relative to powders (Figure 8-5).

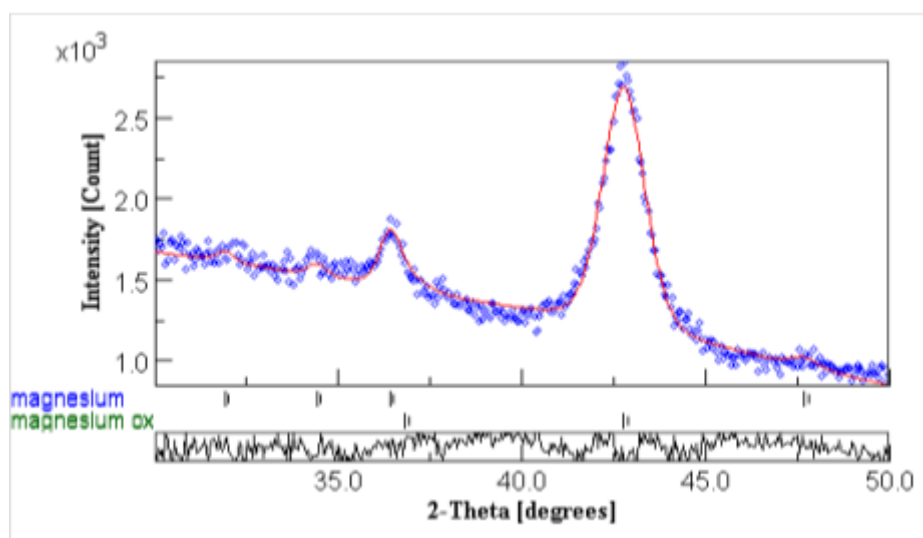


Figure 8-5

Table 7

MgO_93 powder	
Mg % (weight)	9,73
MgO % (weight)	90,63
$2R_{Mg}$ (nm)	35,57
$2R_{MgO}$ (nm)	62,44

This sample shows a different ratio between R_{Mg} and R_{MgO} and a total radius longer than the one of the previous case (Table 7). Actually, the results of MgO_95 are closer to what is desired, since the

nanoparticles are smaller and with a thinner oxidized shell. It is possible to address the diverse results to different experimental conditions during the nanoparticles growth: the oxygen flow seems to be the critical parameter.

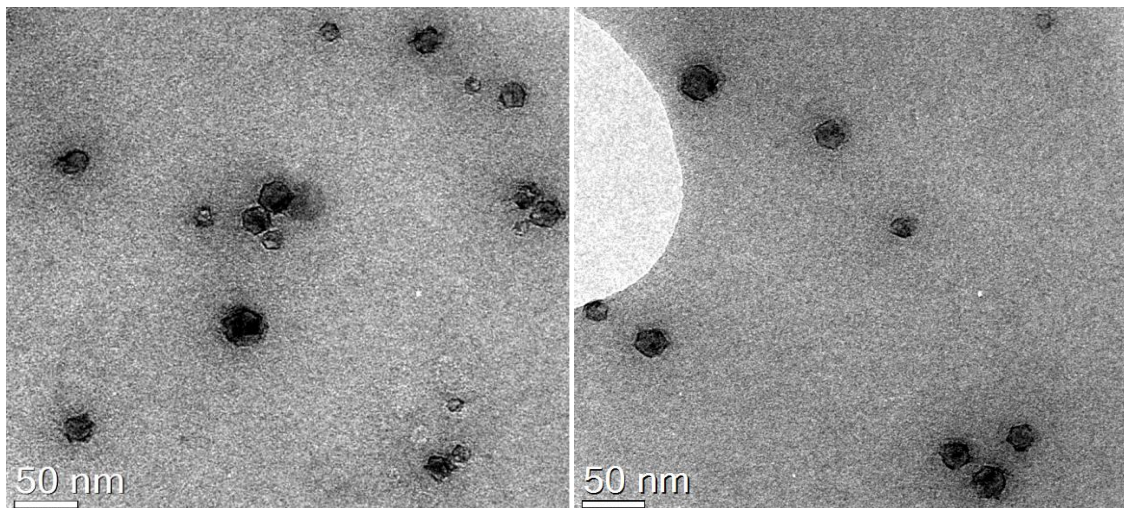
TEM analysis

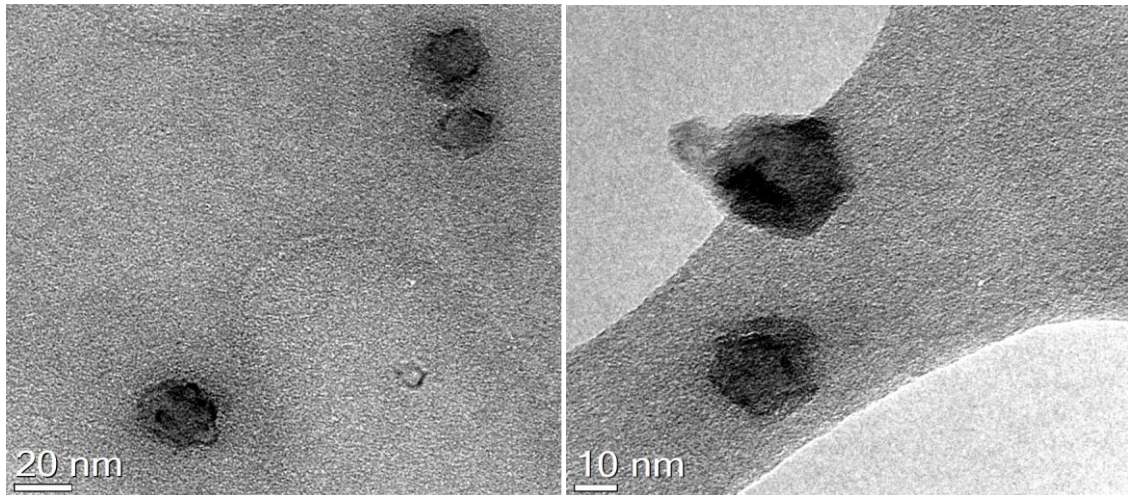
TEM images stress the fact that the creation of nanoparticles with a metallic core and an oxidized shell was achieved. Each technique used shows different nanoparticles characteristics.

The sample used analyzed by this technique was MgO_102, where the oxygen flux was of about $1,2 \cdot 10^{-4}$ torr/s.

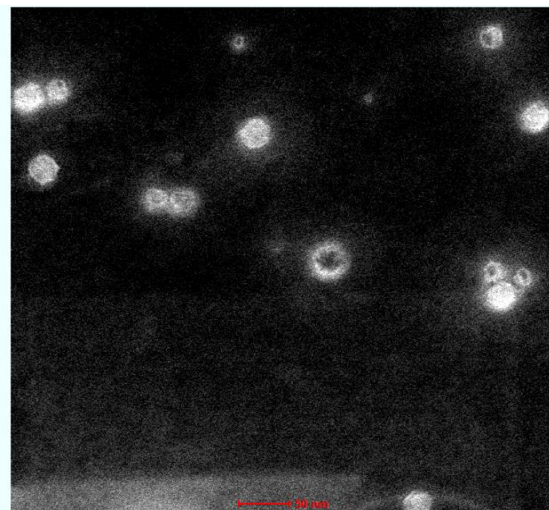
Bright field TEM images reveal that the smallest particles have faced but irregular shapes, while bigger ones get the typical hexagonal structure. The inner and the external parts of the nanoparticles have different colours, being the core brighter than the shell. The fact that hexagonal and not cubic structures are present confirms that magnesium nanoparticles are formed before getting in contact with the oxygen flow which, then, creates the oxidized shell.

Different magnifications are shown.





An high-angle annular dark-field imaging (HAADF) STEM image of some NPs dispersed on carbon film. This technique is sensitive to variations in the atomic number of atoms in the sample. Nanoparticles have a brighter contrast respect than the carbon film. Some particles present a brighter shell so it is possible that are some voids in the inner part of them.



The presence of holes is an evidence of the synthesis of core-shell structure nanoparticles. As it has been explained by a Chinese group, the fast diffusion of Mg atoms from the core to the external part of the particle, combined with the slow one of O atoms, creates holes [31]. The phenomenon that takes place is the so called in situ Kirkendall effect. In 1947, Smigelkas and Kirkendall reported the movement of the interface between a diffusion couple (copper and zinc) as the result of the different diffusion rates of these two species at an elevated temperature [32]. This phenomenon, was the first experimental proof that atomic diffusion occurs mainly through vacancy exchange and not by the direct interchange of atoms, much

rarer phenomenon. The net directional flow of matter is balanced by an opposite flow of vacancies, which can condense into voids or annihilate at dislocations. Directional material flows also result from coupled reaction-diffusion phenomena at solid/gas or solid/liquid interfaces, leading to deformation, void formation, or both during the growth of metal oxide or sulphide films. These holes are usually explained by outward transport of fast-moving cations through the oxide layer and a balancing inward flow of vacancies to the vicinity of the metal-oxide interface. The observed volume fraction for pores is much smaller than would be expected considering the diffusing material amount. It can be explained considering both that vacancies can diffuse into a large volume of material and that they can react with crystalline defects [33]. If the faster-diffusing species is confined into a nanoparticle core, the net rate of vacancy injection should increase markedly, because of the high surface-to-volume ratio of the particle and the absence of defects in the core [34] as in the considered case.

The device was also able to calculate the distribution of the particles diameters (Figure 8-6). The result was very interesting since it is evident that oxidation blocked the particles diameters growth, keeping them very small.

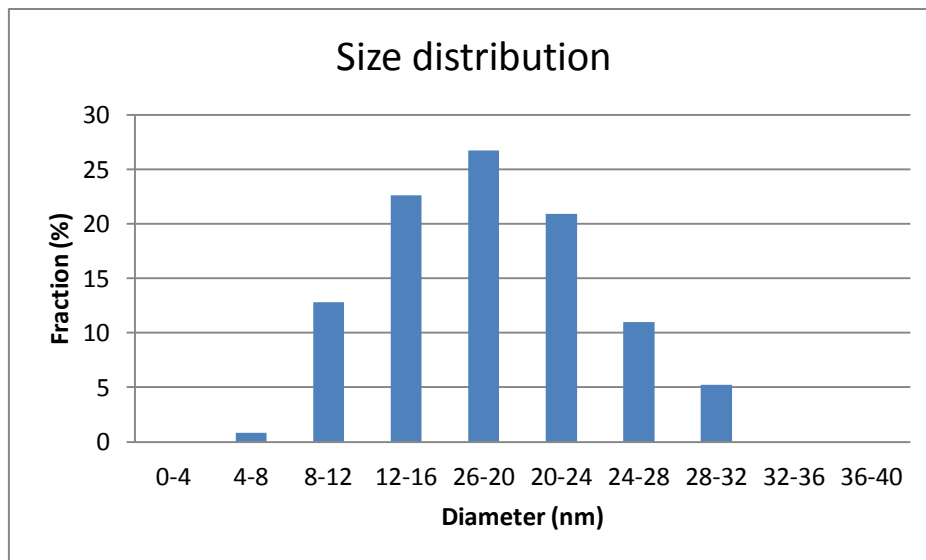
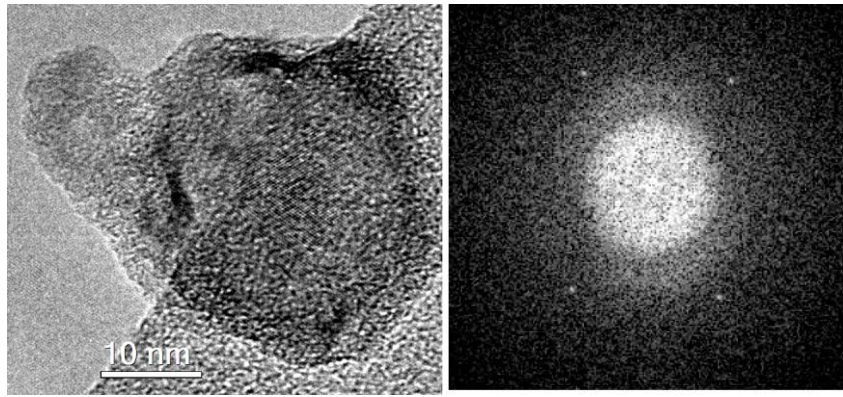


Figure 8-6

High Resolution TEM (HRTEM) image (in the next page on the left) and Fast Fourier Transformation analysis (whose result is on the right) show that nanoparticles are monocrystalline and that crystalline planes are present. The device was able to give an estimate of the interplanar distance.

$$d = (2,78 \pm 0,08)\text{\AA}$$



In Table 8 are reported the experimental lattice fringes found by FFT of HR-TEM images with literature data for Mg and MgO phase. The presence of the last one was unexpected. In the round brackets Miller indexes of the corresponding crystallographic plane are specified.

Table 8

FFT-HR d(Å)	Mg d(Å) (hkl)	MgO d(Å) (hkl)
2,78 ± 0,08	2,778 (100)	
2,60 ± 0,07	2,605 (002)	
2,46 ± 0,06	2,452 (101)	2,425 (111)
2,09 ± 0,06		2,100 (200)

EDS spectra were acquired focusing the electron beam on a single NP and on the carbon film. While copper and carbon X-ray signals derive from the grid and from the carbon film on which the sample is deposited, iron and cobalt ones come from the polar pieces of TEM. Note that there is also a presence of silicon and calcium X-ray signals. Figure 8-7 is relative to the particle, Figure 8-8 to the carbon film, but nothing relevant was derived by these two graphs.

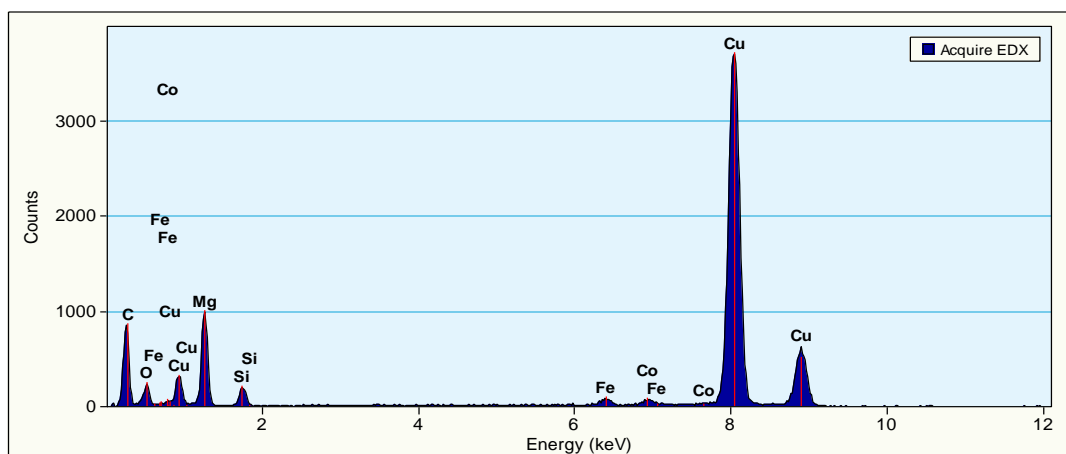


Figure 8-7

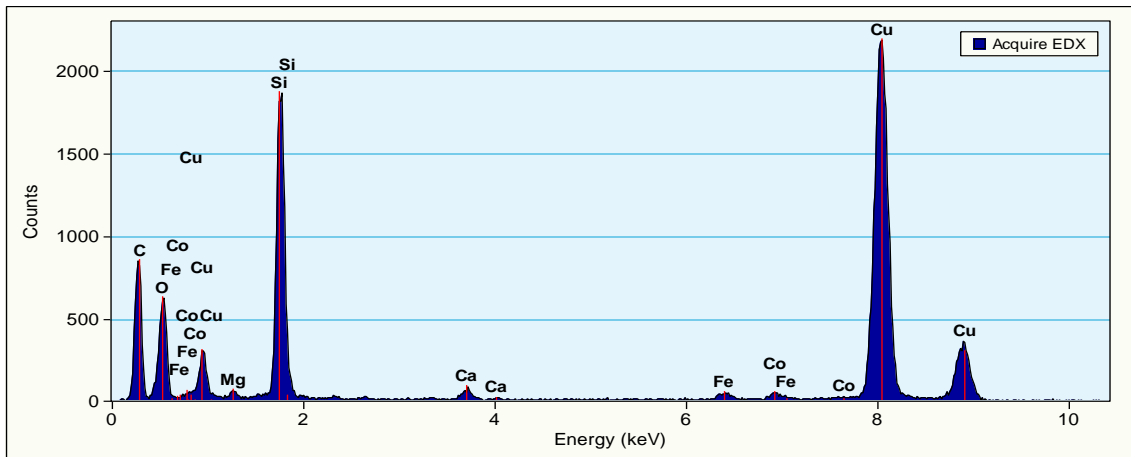


Figure 8-8

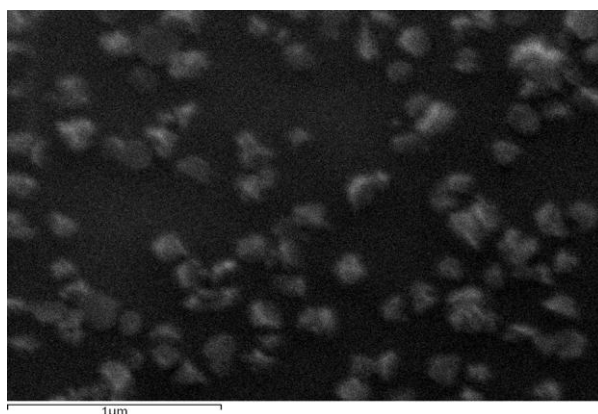
CHAPTER IX. Samples subjected to hydrogenography

In order to understand better the behaviour of nanoparticles with a Mg core and a MgO shell, it can be useful to compare them to pure Mg nanoparticles. For this reason MgPd_51 and MgPd_101 were subjected to hydrogenography measurements. All the images of this section are taken by samples where the material is deposited on two kind of transparent glasses, different for dimensions and composition, that can be named as 1 (square of 15 mm X 15 mm) and 2 (20 mm X 20 mm) . Remember that in the previous section silicon was used as substrate.

MgPd_51

MgPd_51 was grown for a long time and present the typical magnesium nanoparticles with hexagonal disks with diameters between 100 nm and 200 nm and a thickness around 50 nm. The glass used is 1 and a small MgO shell is present due to the sample exposition to air.

Time	40'
Thickness	22 nm

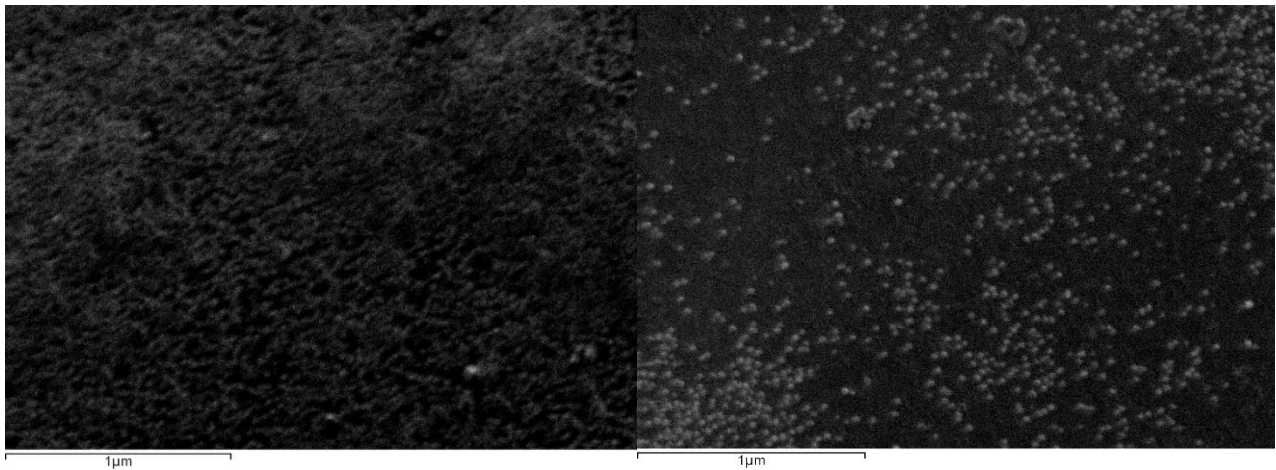


MgPd_101

In this experiment the sample substrate changed: glass 2 was used and the effect proved to be very relevant. While the sample exposed for 2 minutes to evaporation could not be seen due to charge effect, the others showed an interesting result: very small nanoparticles were produced without the presence of

the oxygen flux and thus of the MgO shell, even if a thin oxidation is present due to the sample exposition to air. It is assumed that also MgPd 101 2 minutes shows little nanoparticles, as other sample do. All samples were covered by a 5 nm palladium layer and while palladium was sublimated by a 260 A current, magnesium by a 102 A one.

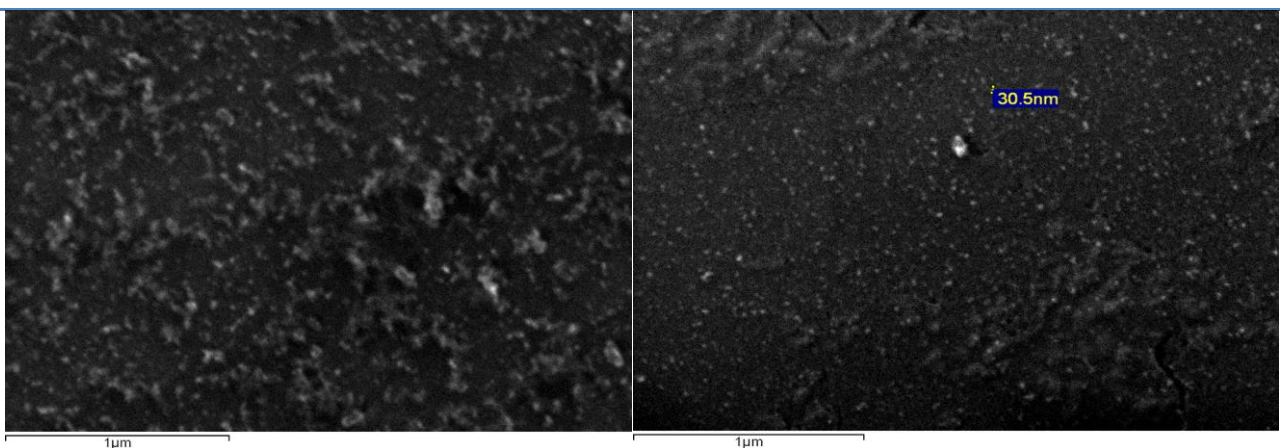
Time	1 min	Time	30 s
Thickness	1,4 nm	Thickness	0,8 nm



MgOPd_99

Palladium was sublimated by a 260 A current and magnesium by a 102 A one, oxygen flux was $1,6 \cdot 10^{-4}$ torr/s. The samples present both a substrate and a coating of palladium and the substrate is glass 1.

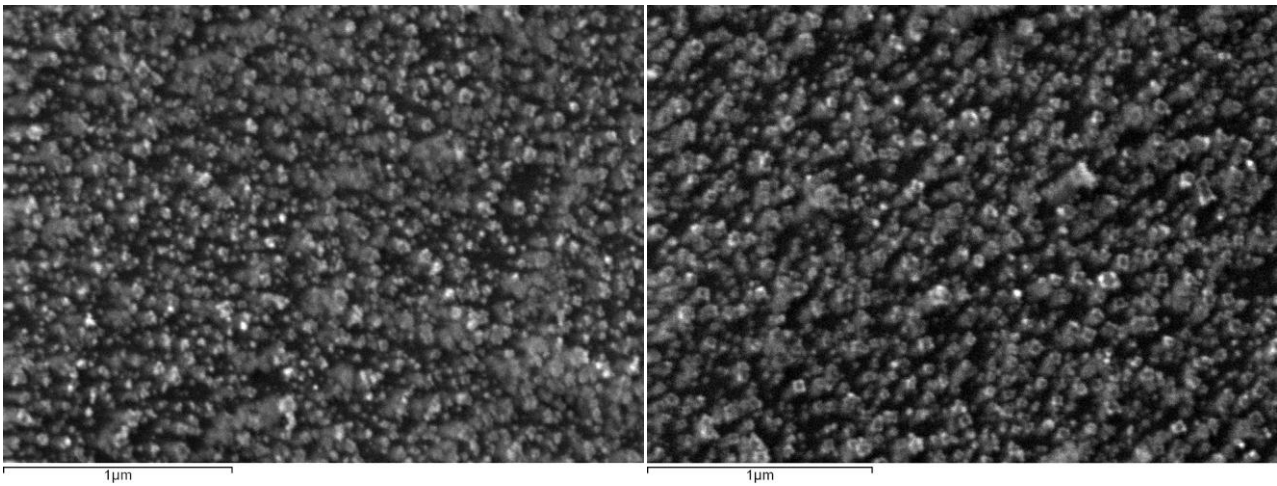
Time	5 min	Time	2 min
Thickness	7,2 nm	Thickness	5,0 nm



MgOPd_100

Palladium was sublimated by a 270 A current and magnesium by a 102 A one, oxygen flux was $1,2 \cdot 10^{-4}$ torr/s. Both samples are covered by a 5 nm palladium coating. Glass 1 is the substrate.

Time	2 min	Time	1 min
Thickness	4,7 nm	Thickness	1,6 nm



CHAPTER X. Hydrogenography

General features

Hydrogenography is a recently introduced experimental technique whose basis is the fact that the quantity of hydrogen stored in a material changes its optical transmission. Thanks to an opportune setup, this method is capable of monitoring the absorption and the desorption of hydrogen of several samples subjected to the same experimental conditions simultaneously. However, the real utility of this approach is the possibility of obtaining the values of key thermodynamic quantities as enthalpy and entropy of hydrate formation.

In order to store hydrogen, MgH_2 could be a very promising material, since it contains 7,6% wt of hydrogen. Its limit is represented by its large enthalpy of formation that is -74 kJ/mol, because it makes the hydrate too thermodynamically favoured respect to the situation in which hydrogen and magnesium are separated: absorbing H_2 is easy but freeing it is too hard, a negative skill for a material that has to behave as storing one. Different attempts to destabilize MgH_2 reversibly and successfully have been made doping the material with elements such as Ni, Cu, Co and Fe whose hydrogen absorption is hard. The hydrates so formed have all enthalpies more negative than what needed. This problem is overcome by changing Mg with Mg_2Si , but in this situation hydrogen absorption is not reversible.

Enthalpy of formation and Pressure-Concentration-Isotherms are determined measuring the changes of optical transmission as the hydrogen concentration varies. Optical transmission is derived by Lambert-Beer's law, according which

$$\ln(T) = -\lambda x$$

Where x is the sample thickness, λ the absorption coefficient (for Mg it is equal to 0.11 nm^{-1}). Transmitted intensity I can be written as a function of the absorbed hydrogen:

$$I = I_0[(1 - f) + f e^{-\lambda_\alpha x(1-c) - \lambda_\beta xc}] + I_b$$

Where I_0 is the incident intensity, λ_α the absorption coefficient in the metallic phase, λ_β in the hydrate one, c indicates the percentage of hydrogen present in the material ($c = 1$ in the hydrate phase and 0 in the metallic one), f the covering of the sample on the substrate and I_b the noise signal.

Hydrogenography is applicable to any reaction involving a change in the electronic structure of the material. This is the case of light-weight hydrogen storage materials such as alanates and boronates,

insulators with a wide optical band gap. But the presence of a Mott transition is not necessary: hydrogenography was applied with good results also to a system such as Pd-H that is metallic at any H₂ pressure.

Another advantage is that it is not necessary to have a former knowledge of the relation between the optical properties and hydrogen concentration to apply the method: under isothermal conditions, if there is a hydrogen concentration plateau in the *PCI* due to coexisting phases, the transmittance will necessarily exhibit a plateau at the same pressure.

Experimentally it has been shown that a dramatic change in optical transmission occurs when two phases coexist. Using experimental data it is possible to create the so called *PTI* (Pressure-Transmission-Isotherms), plotting hydrogen pressure versus the logarithm of the normalized transmittance. According to Beer-Lambert's law the logarithm of this ratio is proportional to the hydrogen concentration while the two phases are coexisting.

In the end, *PTI* are similar to *PCI*, but the diffusion issues typical of the *PCIs* are lowered.

Substrate presence effects

An important point to discuss is the presence of the substrate. Hydrogenizing a sample makes it increase its volume for values between 11% to 32%.

While bulk materials can expand in all three dimensions, the rigid substrate where nanoparticles are deposited do not allow the free expansion of the film parallel to the surface during hydrogenation. The contrast between the adhesion forces and the sample expansion generates compressive stresses that might influence the equilibrium plateau pressures of the samples and, consequently, their thermodynamics (Figure 10-1).

It is possible to address this behaviour to the H-H interaction that is an elastic one. Normally, when H₂ diffuses in the host material, it increases its volume, creating a long range strain field around the solute atom, making it easier for further hydrogen to enter the system. However, the sign of this interaction depends on the boundary conditions and the presence of the substrate makes the sign of the force switch from attractive to repulsive. For this reason, hydrogen must have a higher chemical potential to diffuse in the material and to create a new phase. Thus, the substrate makes the equilibrium plateau shift to higher pressure values.

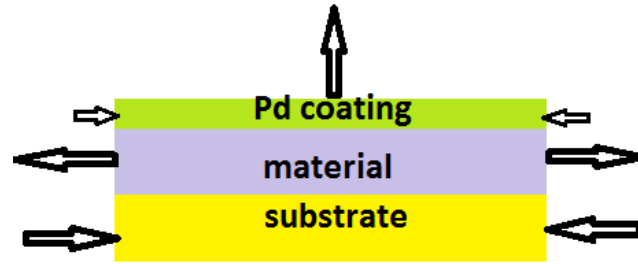


Figure 10-1

Hysteresis phenomenon

Ideally the processes of hydrogenation and dehydrogenation would be described by the same isotherms, but it is not what is experimentally observed: a phenomenon called hysteresis occurs.

There are two different approaches that explain the presence of this feature and both focus their attention towards the presence of stresses arising in material during the phase transformation. Hysteresis is related to elastic and/or plastic deformations.

In the first case the sample is thought to behave like an elastic body, without permanent deformations. When hydrogen enters the material, it creates strain and consequently stress, as it is below the Yield stress of the material. Sinha et al developed a model to explain the hysteresis presence exploiting the elastic strain energy effects in combination with the occupational sites of hydrogen inside the host material [35]. According to this study, gas atoms occupy interstitial sites smaller than the atoms themselves. For this reason there is no energy barrier to overcome during desorption and the dehydrogenation process can occur at lower pressures respect to absorption. Schwarz and Khachatryan used a different approach, focusing not on hydrogen atoms, but solving the problem in terms of metallic and hydrate phases in the material [36]. The formation of the expanded (hydrate) phase occurs under the compressive forces of the metallic phase during hydrogenation, leading to the so called coherency stresses. The opposite situation happens during desorption, where the metallic phase is formed under a tensile stress generated by the hydrate phase. Therefore, dehydrogenation benefits from the presence of an already expanded lattice and so it takes place at lower pressures. The hysteresis depends on the mechanical properties of the metal hydride (Shear modulus G_s and Poisson's ratio ν), lattice expansion ε_0 , width of the plateau ($c_\beta - c_\alpha$) and temperature, according to the following relation:

$$\ln \left(\frac{P_{abs}}{P_{des}} \right) = \frac{8\nu G_s \frac{(1-\nu)}{(1+\nu)} \varepsilon_0^2 (c_\beta - c_\alpha)}{kT}$$

When a material is deformed plastically dislocations appears and they play a non-irrelevant role during hydrogen formation and decomposition. According to Flanagan et al, their presence makes a shift of plateaus to higher and lower pressures, respectively [37]. The overall hysteresis is equal to the energy involved in formation and movement of dislocation during hydrogenation and dehydrogenation. Anyway, the fact that nanoparticles cores are formed by single crystals, as TEM analysis showed, makes less likely this hypothesis for the systems studied. Another approach considers the problem in terms of Gibbs free energy: it is the path followed by Birnbaum et al [38]. They assumed that the change of the free energy during hydride formation ΔG_{abs} involves different terms, as shown below

$$\Delta G_{abs} = \Delta G_{abs}^{chem} + \Delta G_{abs}^{el} + \Delta G_{abs}^{pl} + \Delta G_{abs}^{surf} \Delta G_{abs}^{surf}$$

Where ΔG_{abs}^{chem} is the free energy change on forming the unconstrained hydrate phase, ΔG_{abs}^{el} and ΔG_{abs}^{pl} the free energies associated to elastic and plastic deformations and ΔG_{abs}^{pl} is the surface free energy term. Similarly, the change of free energy during dehydrogenation ΔG_{des} can be written as

$$\Delta G_{des} = \Delta G_{des}^{chem} + \Delta G_{des}^{el} + \Delta G_{des}^{pl} + \Delta G_{des}^{surf}$$

Assuming that all the terms except the ones relative to plastic deformations have similar values, the overall Gibbs free energy change is just given by

$$\Delta G = \Delta G_{abs} - \Delta G_{des} = \Delta G_{abs}^{pl} - \Delta G_{des}^{pl}$$

Therefore, the model addresses the presence of hysteresis just to plastic deformations.

Experimental setup

The main component in a hydrogenography setup is the (de)hydrogenation gas cell that contains the samples. It is placed in an oven with a temperature controller. Due to the presence of sapphire windows, the maximum temperature that can be present in the cell is 573 K. In order to perform the measure, a white light source illuminates the samples, while a CCD camera detects the amount of light that passes through the sample. This operation is done while a hydrogen flow passes into the camera. The pressure is so determined modifying the inlet and the outlet flux and choosing the desired gas mixture entering the chamber. The software can detect at the same time both different samples and different parts of the same sample. It can also average the results in the XY plane or just along one direction: X or Y.

Figure 10-2 shows the samples disposition as seen by the CCD camera. The zones different brightness depends on their transparency.

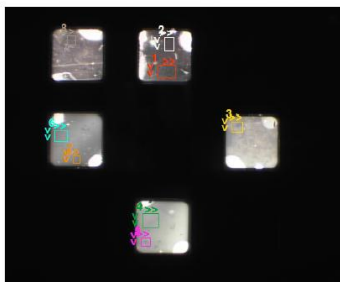


Figure 10-2

The experimental set up used in this work is schematically represented by Figure 10-3 and made up of:

- Two PT-100 resistors, that act as temperature controllers;
- A 150 W white light source;
- A 3-channel (RGB) SONY XC-003 CCD camera
- A blanket, which covers the camera and the vacuum cell, in order to avoid any disturbance to the setup coming from the external environment;
- A PID system, that controls the opening of the input valve;
- A baratron pressure gauge, reading the actual pressure;
- A flow meter, that controls the pumping speed, together to the output valve;
- A Delta 0-30 volt power supply, which regulates the opening of the output valve;
- Two gas bottles, with different mixtures of pure hydrogen, argon and hydrogen;
- A pumping system consisting of a diffusion and a rotary pump.

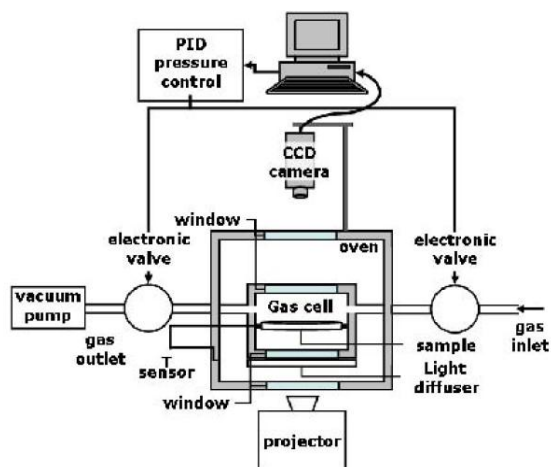


Figure 10-3

Results

Hydrogenography measurements performed were equilibrium ones: hydrogen pressure changed its value after a constant time set by the user. The gas bottle which was utilized to make hydrogen enter was the one with a mixture of argon (95,85%) and hydrogen (4,15%). The pressure rate could be set as a linear, a quadratic or a logarithmic function. An example is shown in Figure 10-4.

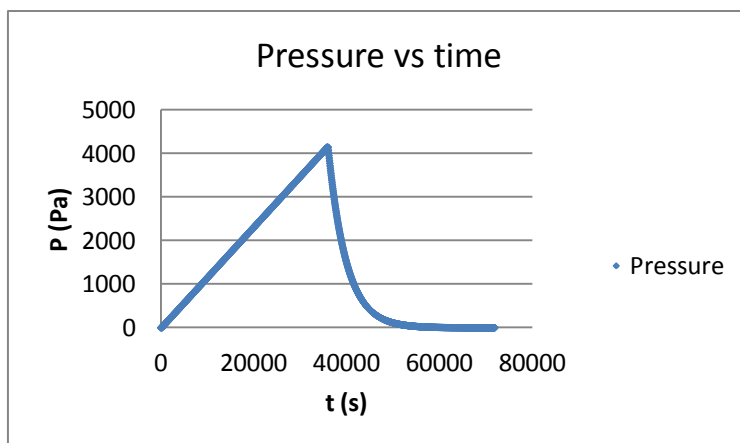


Figure 10-4

Anyway, all the measurements performed had both a logarithmic increase and decrease.

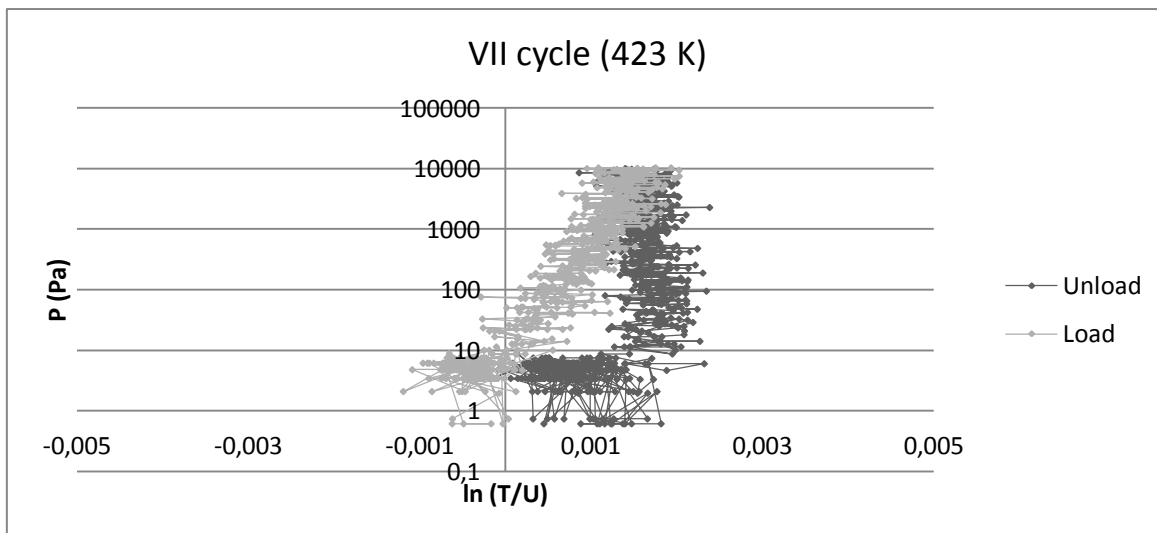
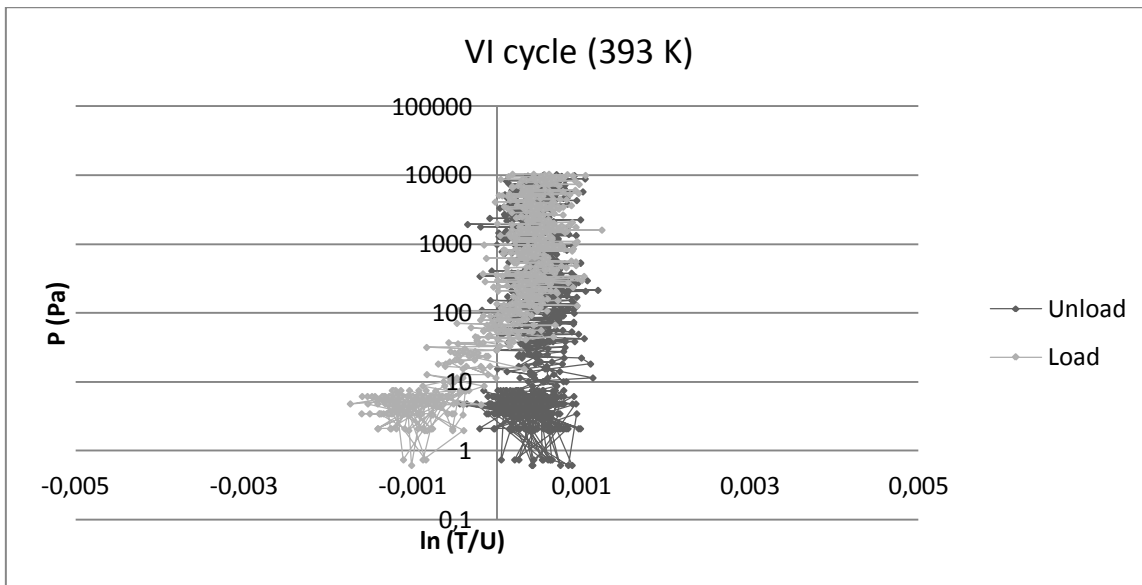
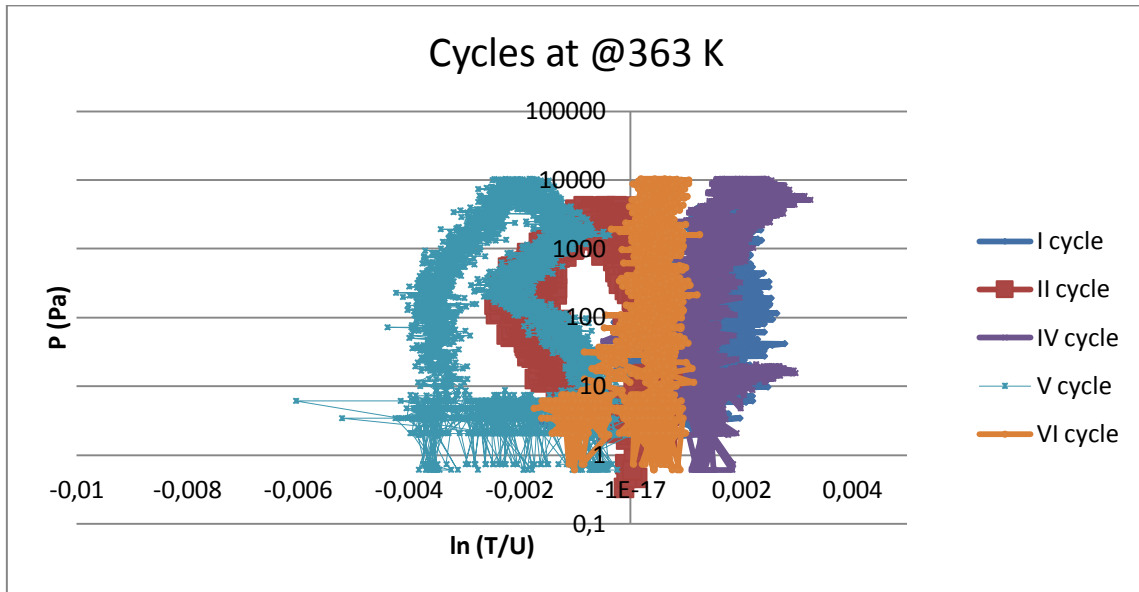
The expression $\ln\left(\frac{T}{U}\right)$ stands for:

$$\ln\left(\frac{T}{U}\right) = \ln\left(\frac{\frac{I - I_d}{I_0 - I_d}}{\frac{J - J_d}{J_0 - J_d}}\right)$$

Where I and J represent, respectively, the light intensity relative to the sample and to the light source, the subscript 0 stands for the initial value (without hydrogen) and d for the dark value, the value measured by the CCD camera even if the light source is covered.

MgOPd_99 2 minutes

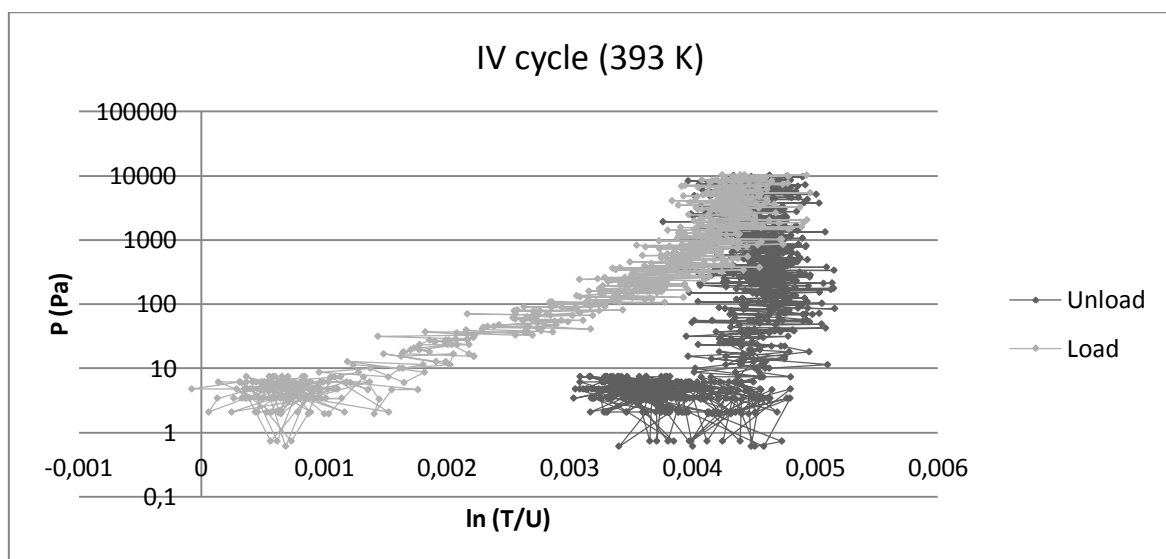
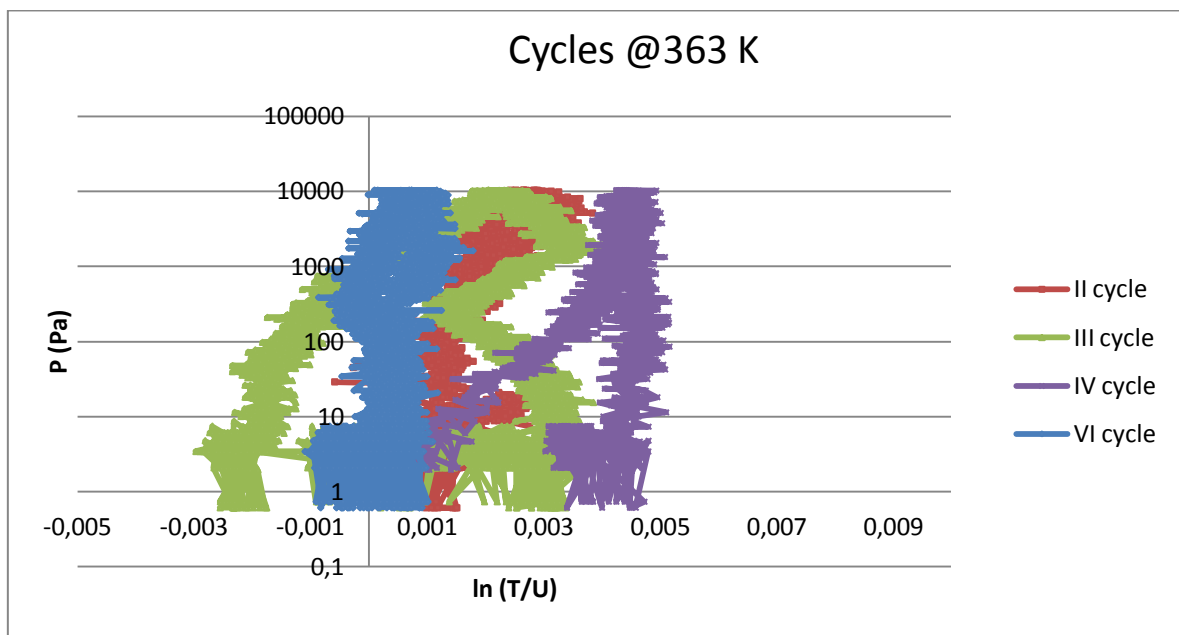
This sample underwent eight cycles: six at 363 K (the first five and the last), one at 393 K (the sixth) and one at 423 K (the seventh).

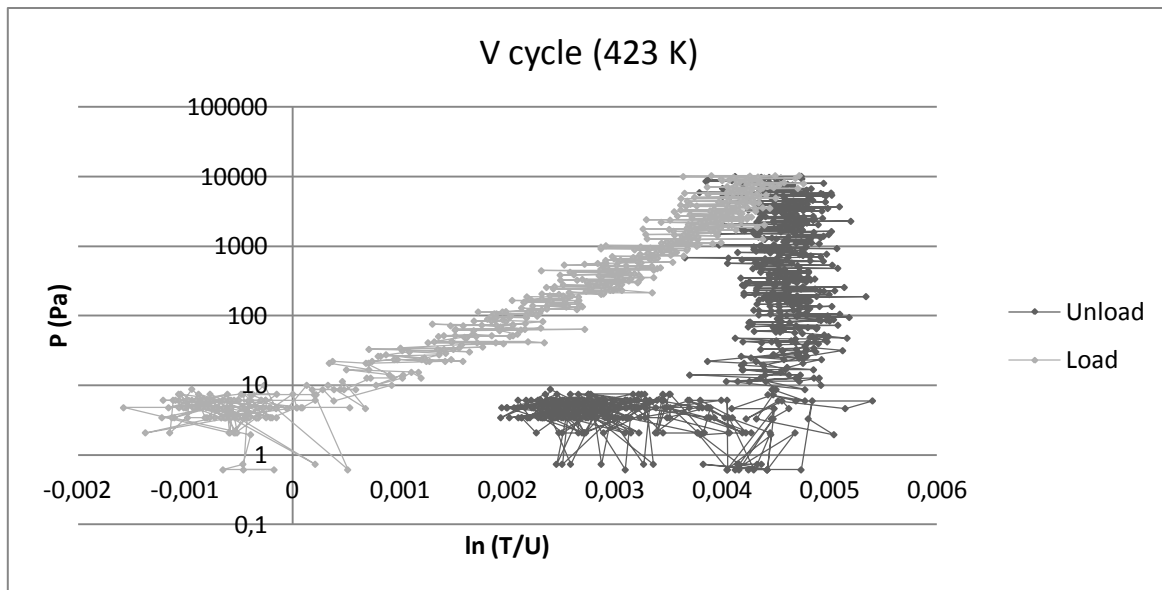


As can be grasp from the data, no plateau appears. Moreover the very low values on abscissa mean that the optical contrast is very low, probably due both to the poor hydrogen absorption efficiency and the small amount of material. The third cycle was not shown since its behaviour was so irregular that the measurement surely suffered from measuring setup problems.

MgOPd_99 5 minutes

The cycles made on the sample were six: the forth at 393 K, the fifth at 423 K and the others at 363 K.

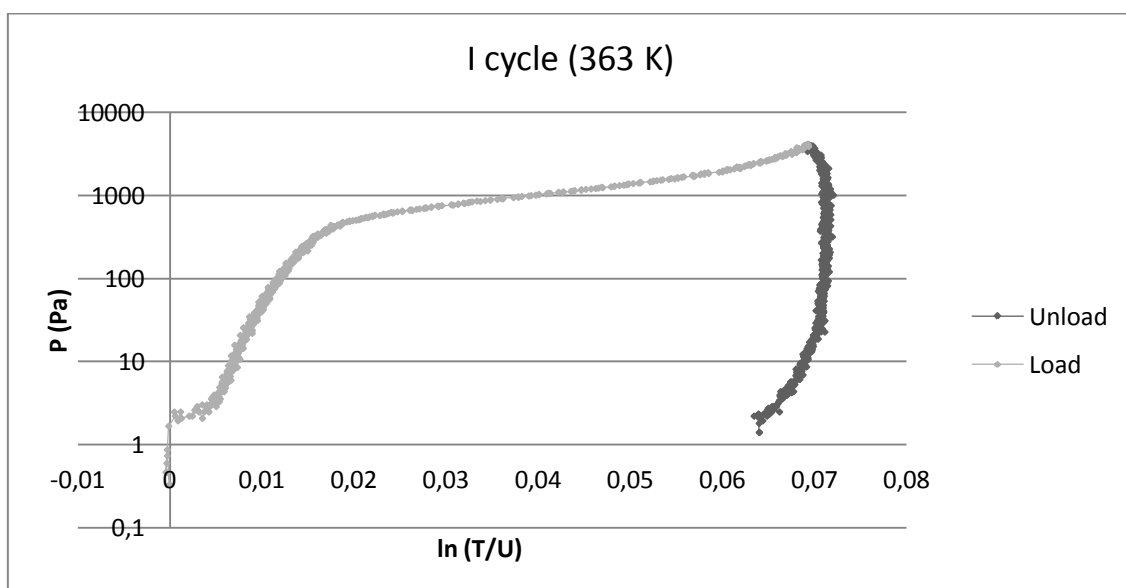


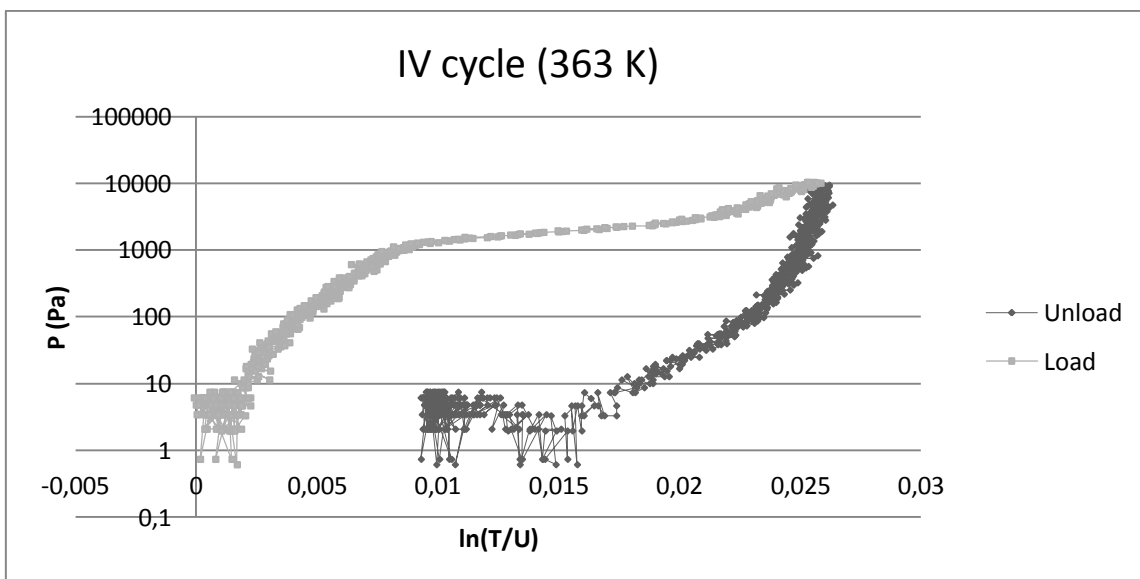
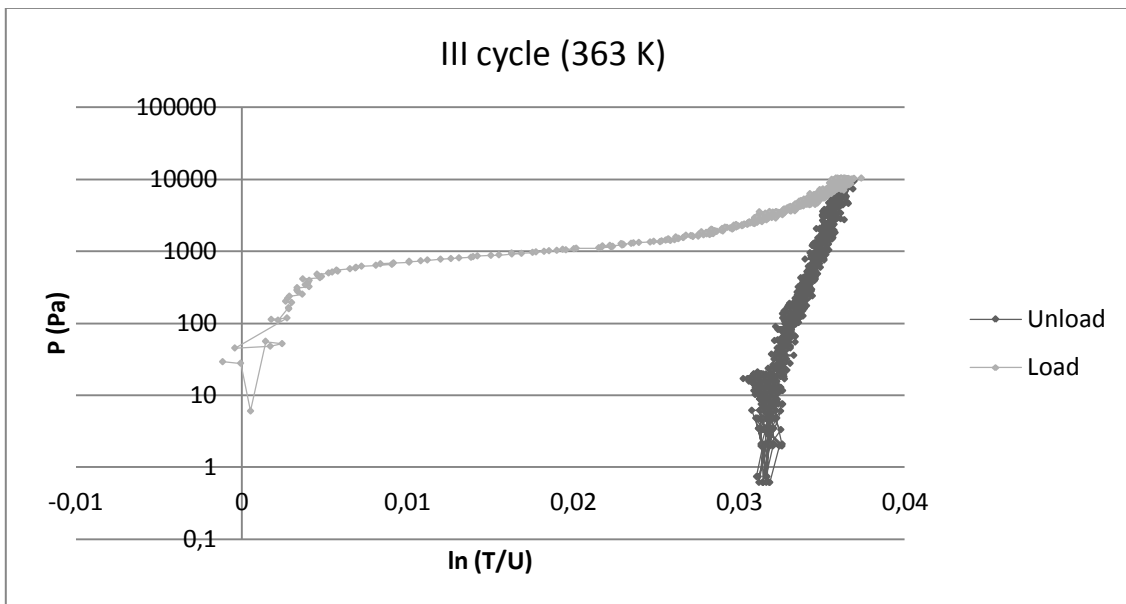
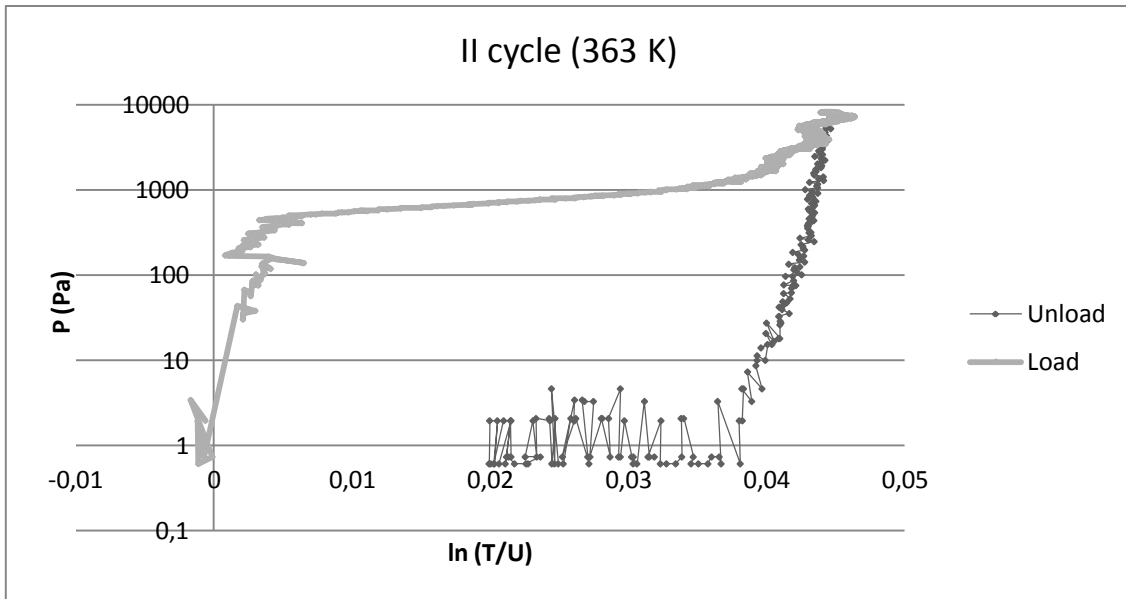


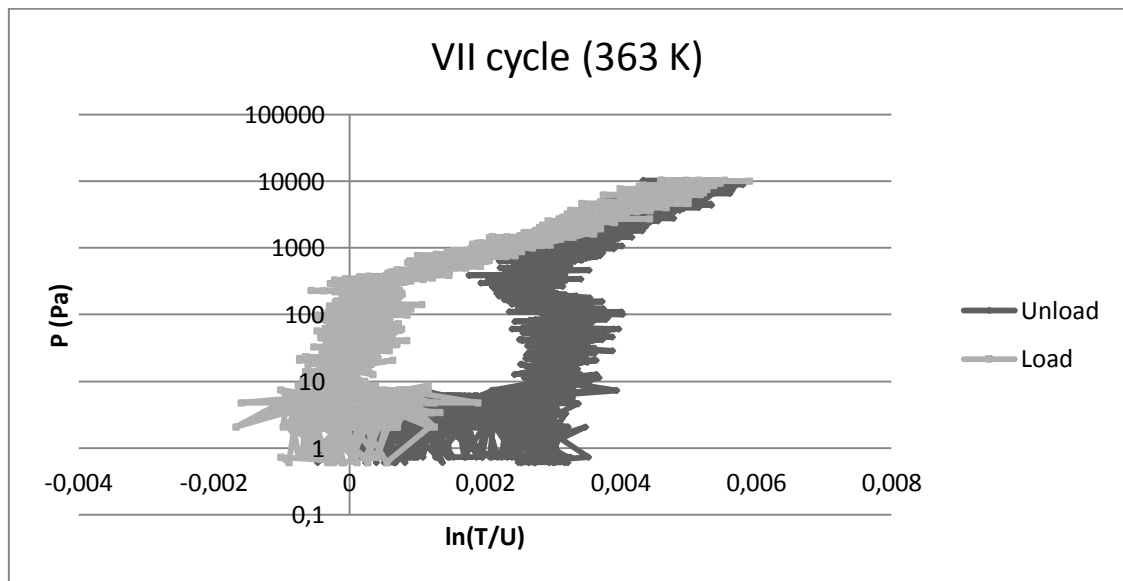
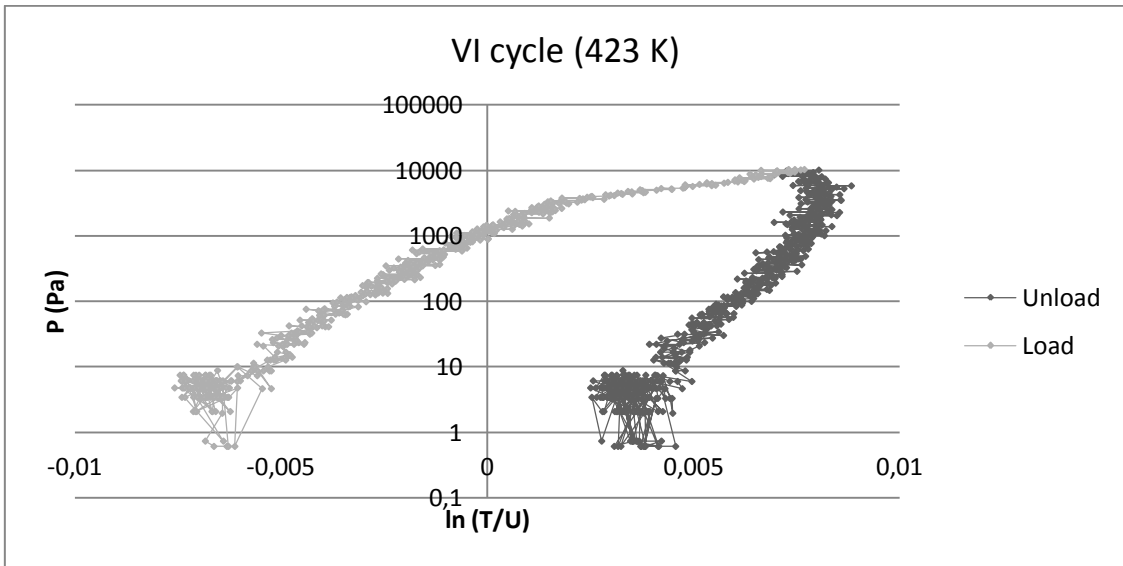
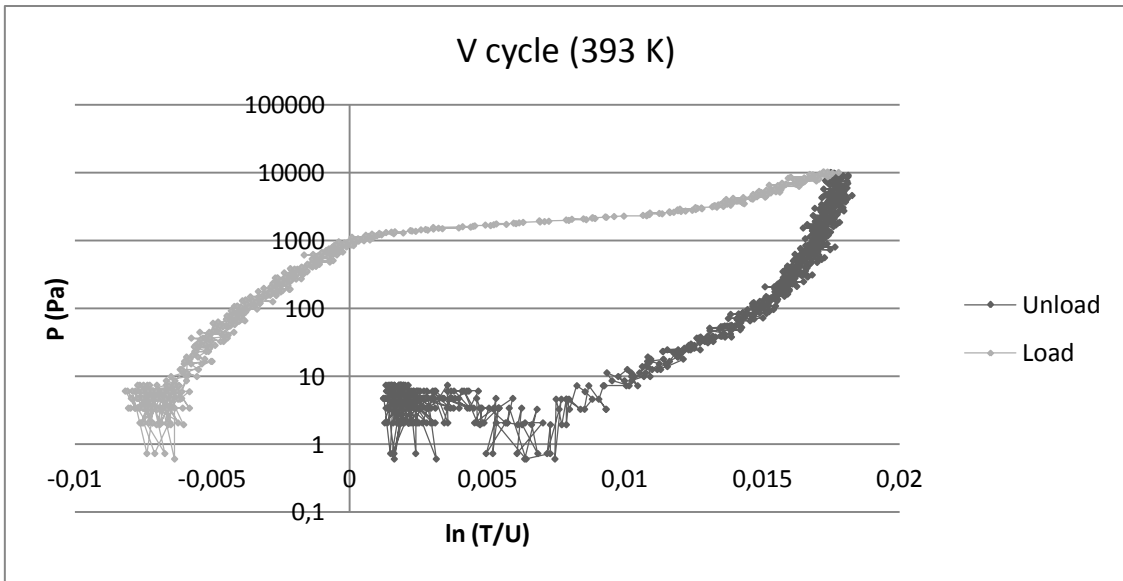
This sample shows a higher optical contrast than in the previous case. It is possible to address these difference to the higher deposition time and, thus, the larger amount of material deposited. The first cycle was not represented since its shape was so strange that must have been affected by errors in the measurement.

MgPd_101 2 minutes

This one underwent seven measurements: the first four and the last at 363 K, the fifth at 393 K and the sixth at 423 K.







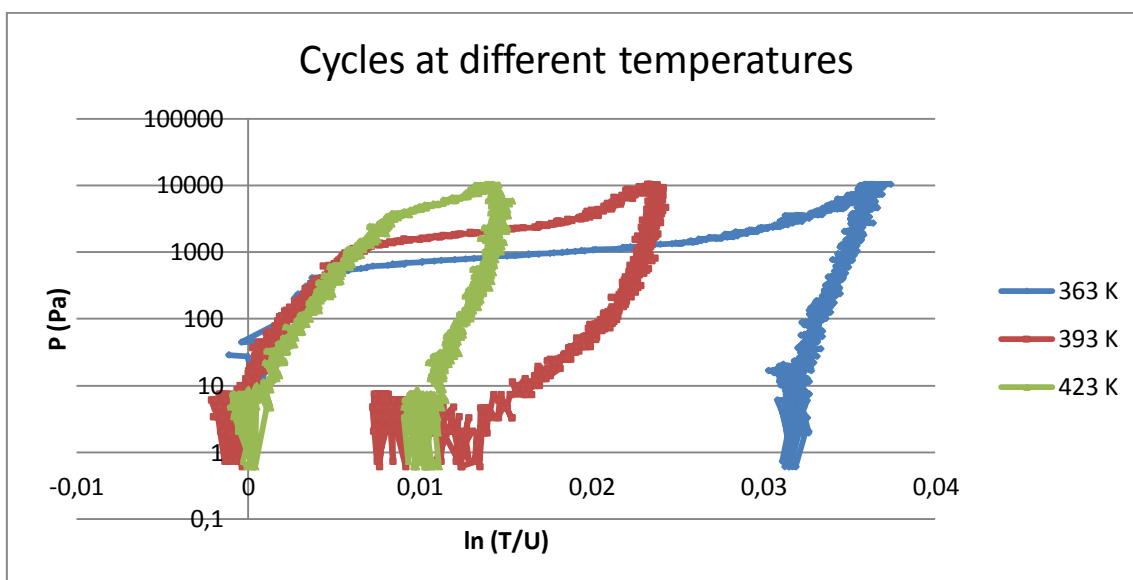
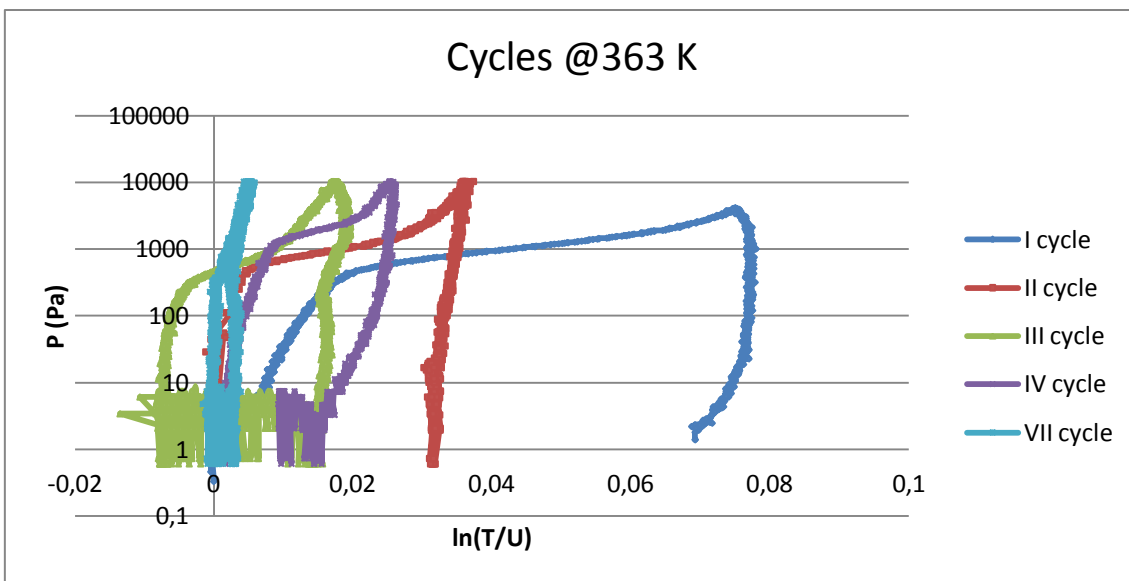


Table 9

P_{eq} (Pa)	T (K)
528	363
1947	393
5105	423

This sample performed very well, showing a plateau in each cycle and also at different temperatures, so that it was possible to calculate the enthalpy of formation, even if in a quite rough manner: the equilibrium pressure values were estimated graphically from the plots. Once the inflections points are individuated, which limit the plateau, the corresponding abscissa points are found. The equilibrium pressure is the one of the average between the two x-axis points, chosen as told before. The error estimate is the 5%.

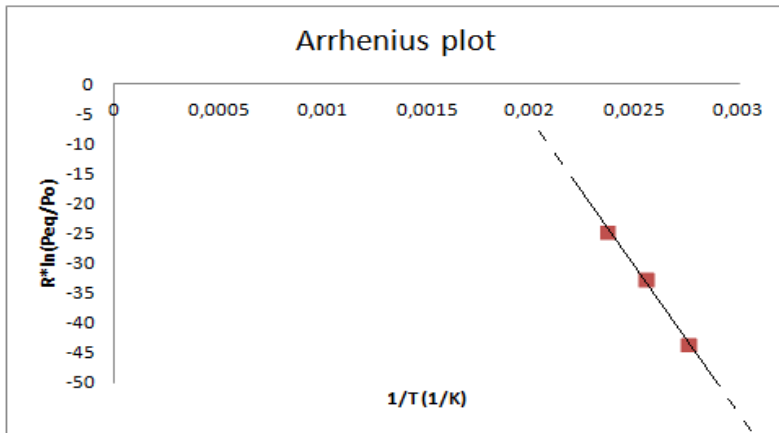


Figure 10-5

$$\Delta H = -(48 \pm 2) \frac{kJ}{mol}$$

$$\Delta S = (11 \pm 3) \frac{J}{K mol}$$

Anyway, it is also evident that cycling more times the samples, the optical contrast decreases, as if a complete desorption has not been reached for each cycle. A phenomenon that can be imagined looking at the unloading branch in the plots and at the one below, where on the abscissa there is simply the samples luminous intensity. Each cycle, except the first one, starts almost at the last value of the previous one. The first cycle was not considered since it shows initial and final intensity values very far from the others.

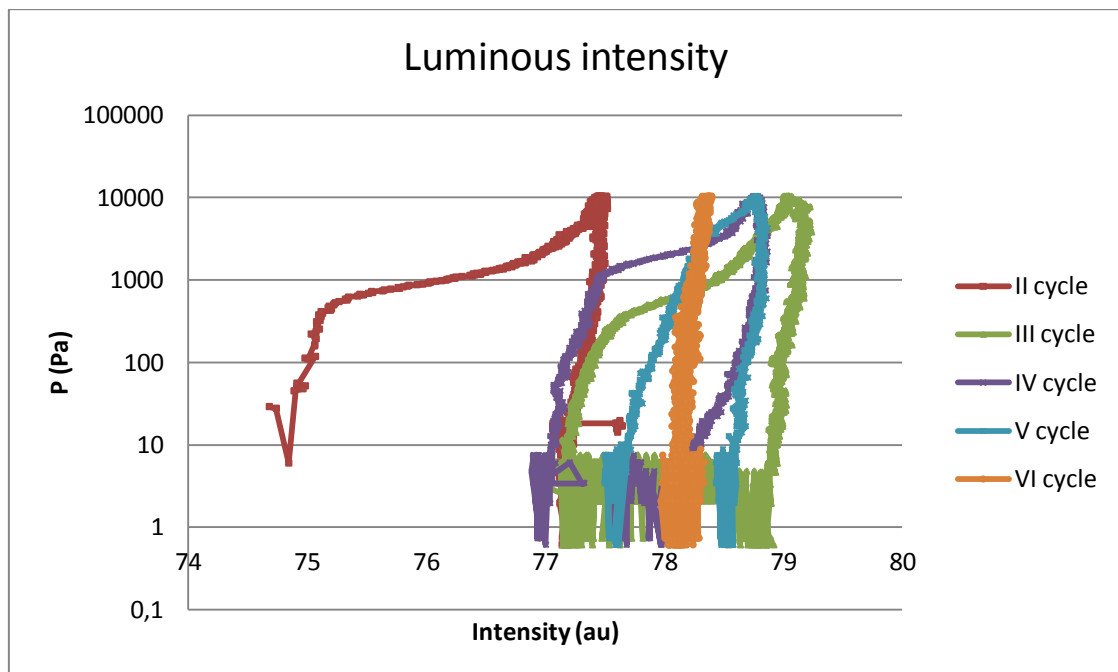
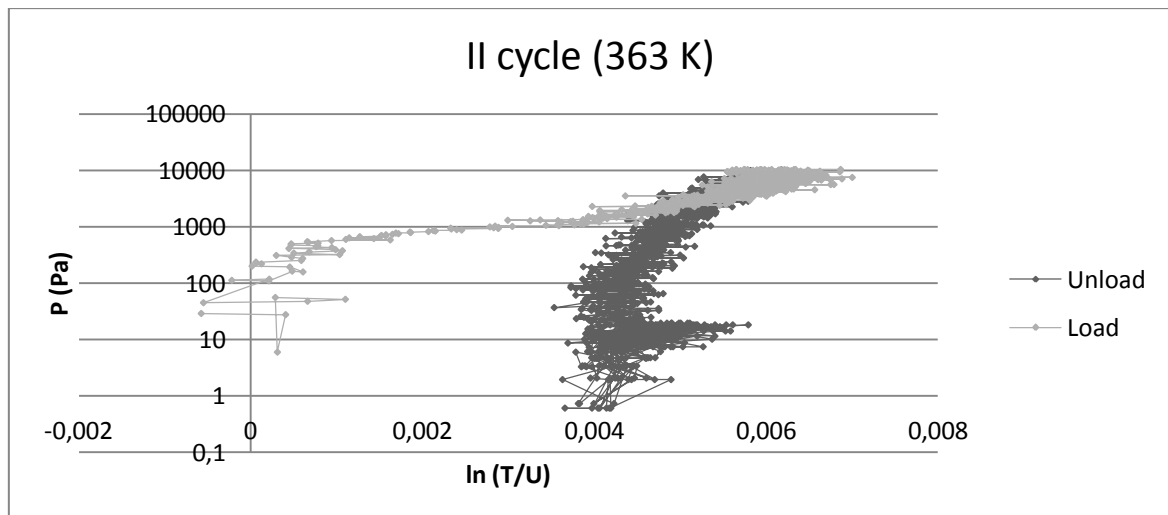
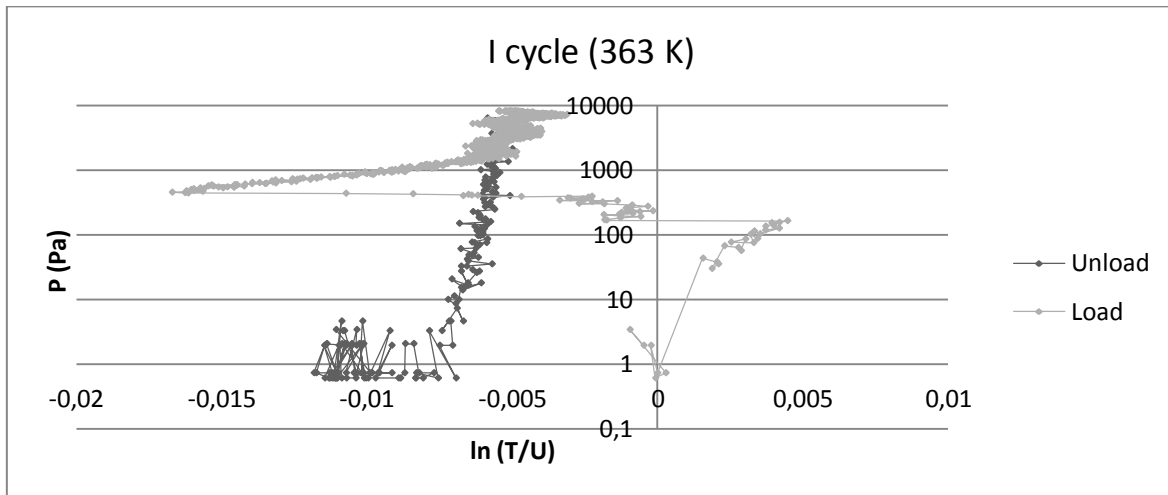


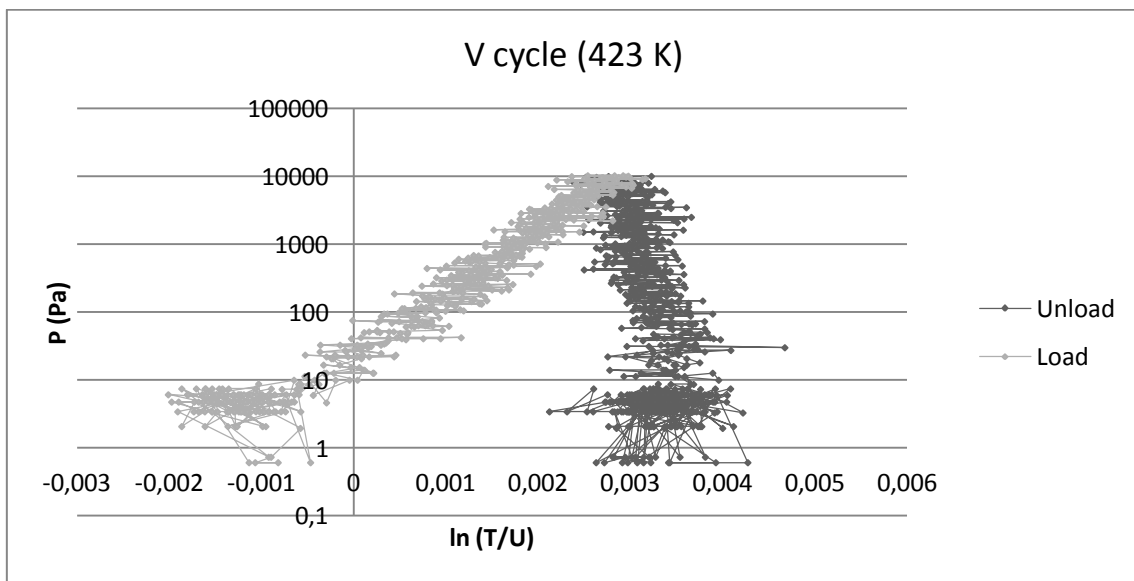
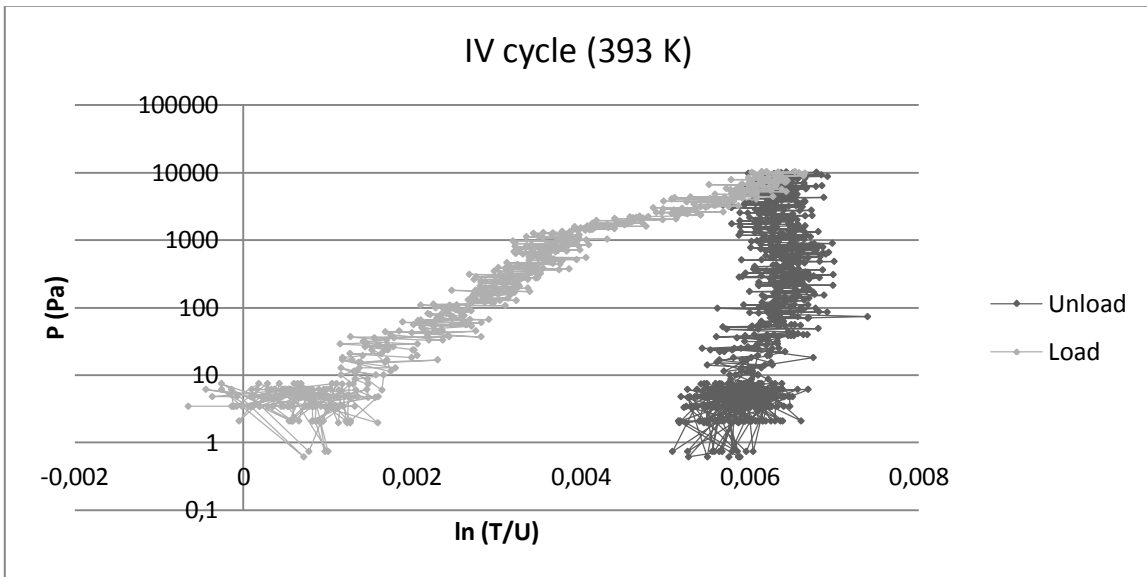
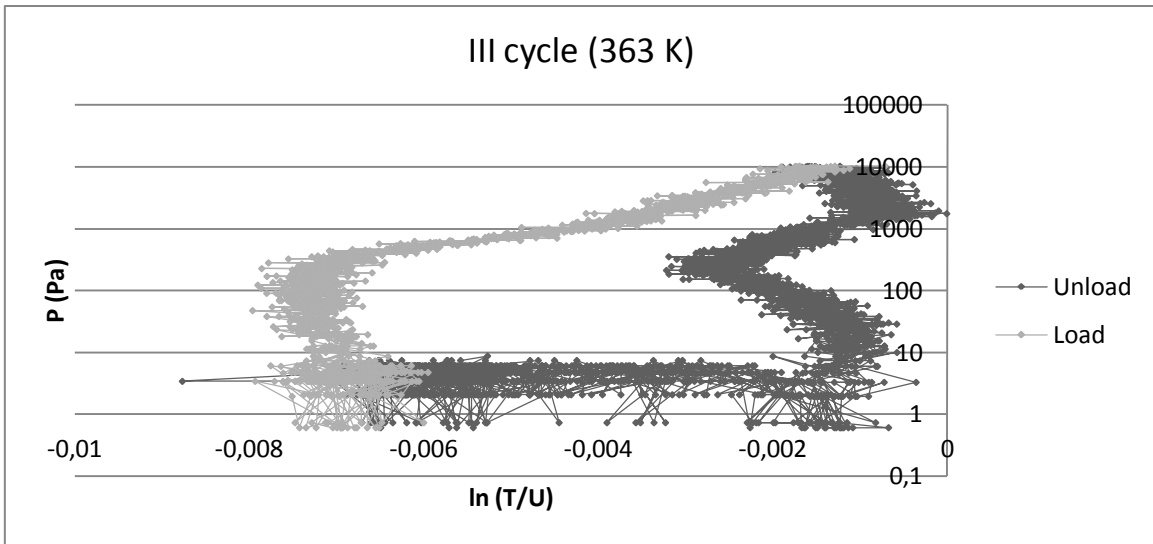
Table 10

Cycle	Average of the first five RAW data (au)	Average of the last five RAW data (au)
II	74,83	77,62
III	77,66	77,28
IV	77,25	77,59
V	77,55	78,49
VI	78,18	78,06

MgPd₁₀₁ 1 minute

This sample was put in the experimental setup as the MgOPd₉₉ 5 minutes.





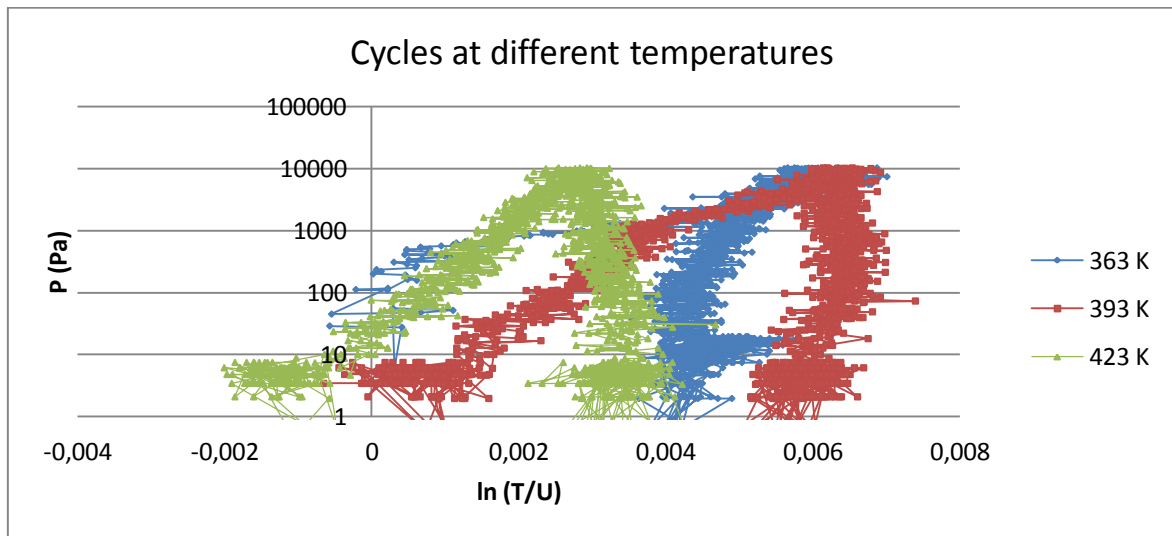
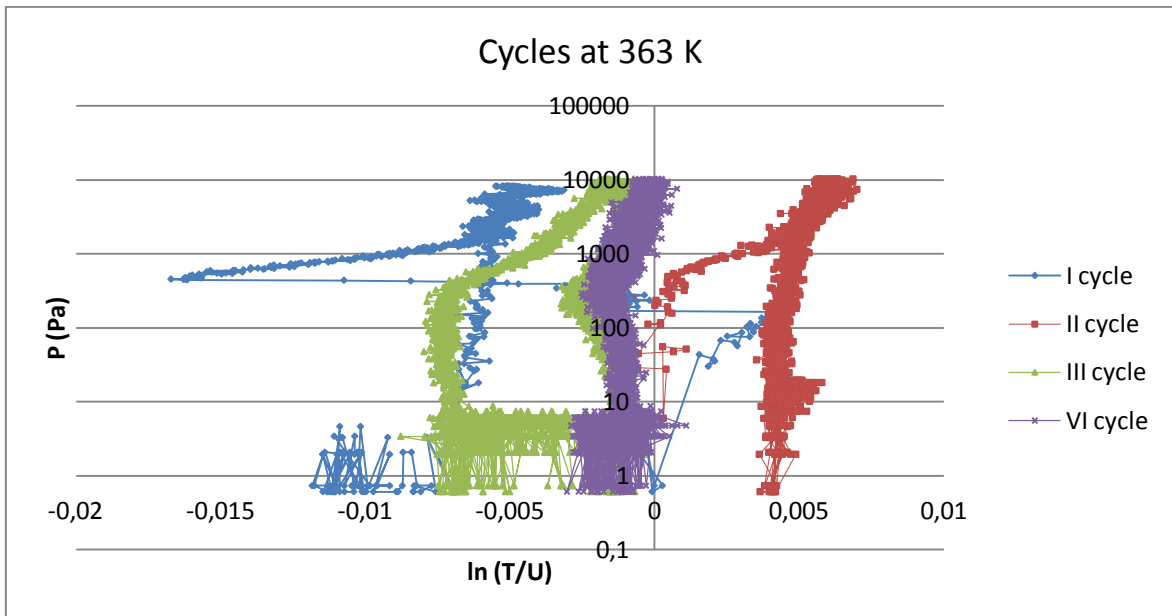
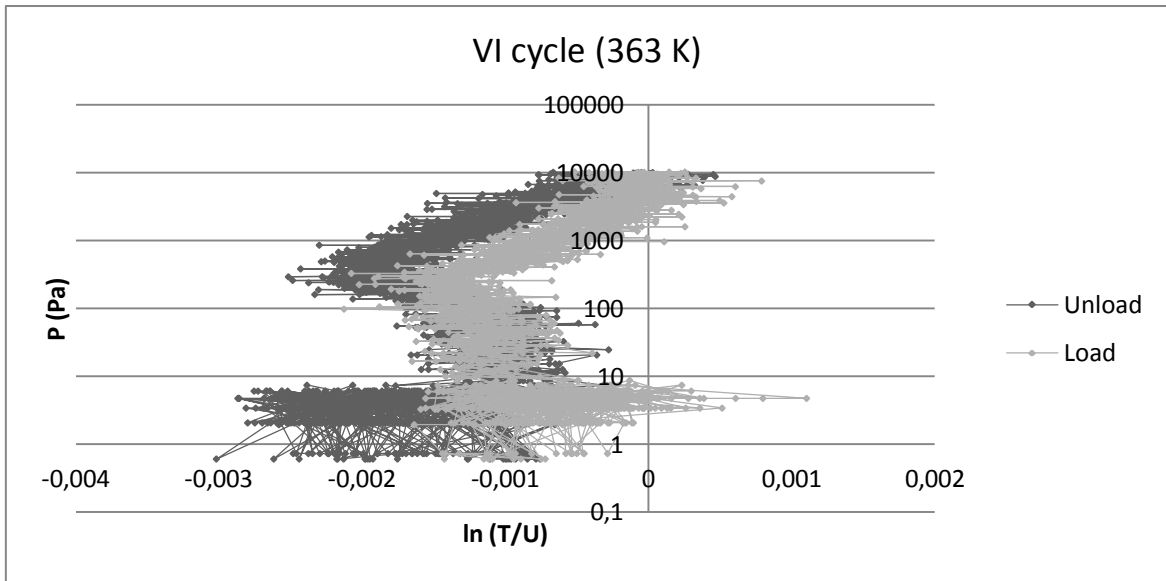


Table 11

P_{eq} (Pa)	T (K)
552	363
1995	393
--	423

This sample shows clear plateaus except for the case of the VI cycle. The reason could lie in the progressive deterioration of the sample, as observed before.

Anyway it is possible to do an evaluation of both formation enthalpy and entropy by exploiting the same technique used previously and the resulting Arrhenius plot (Figure 10-6).

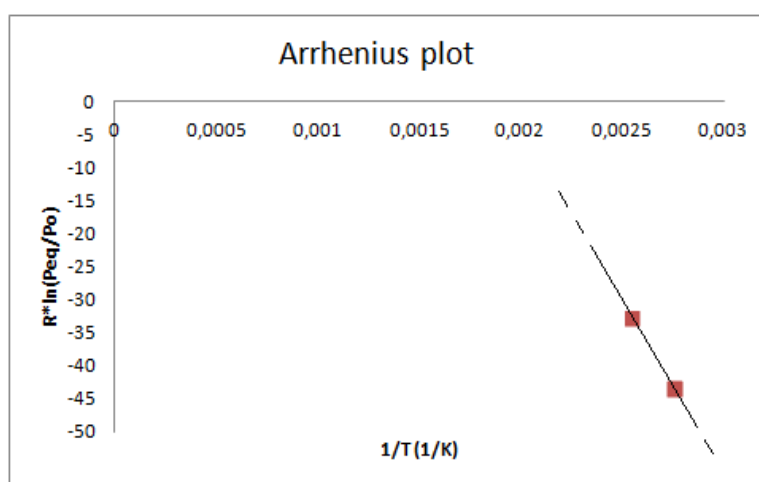


Figure 10-6

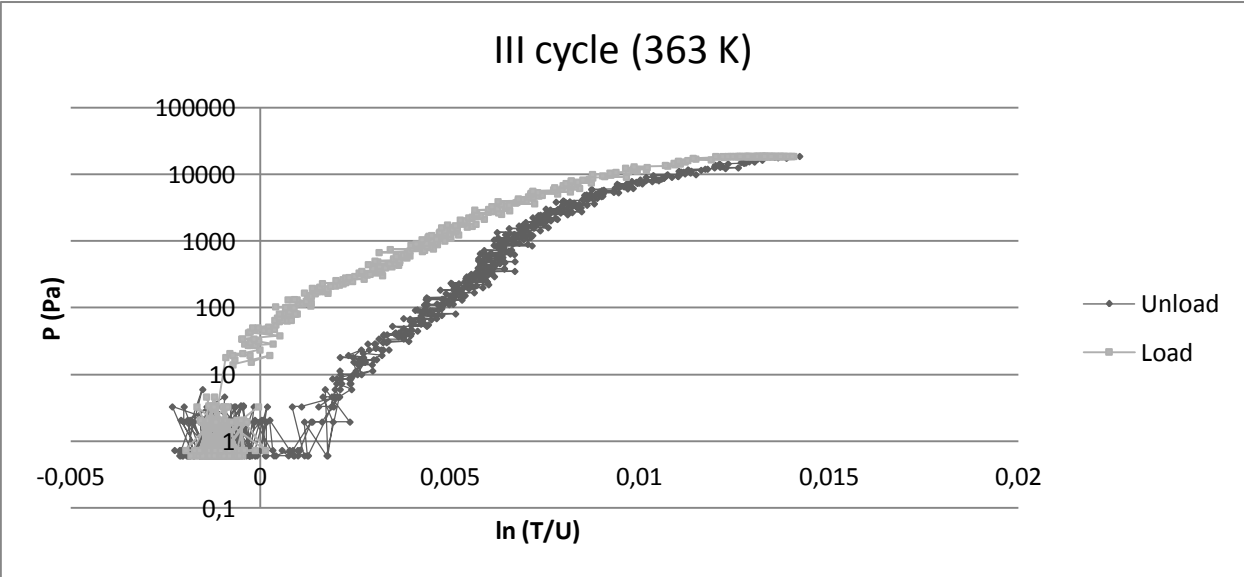
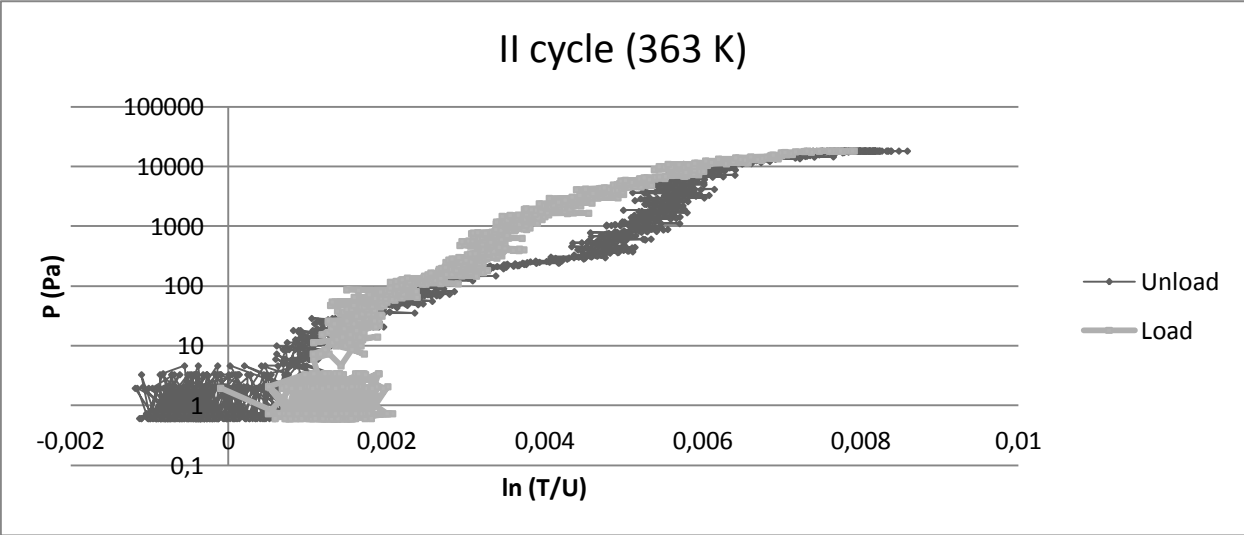
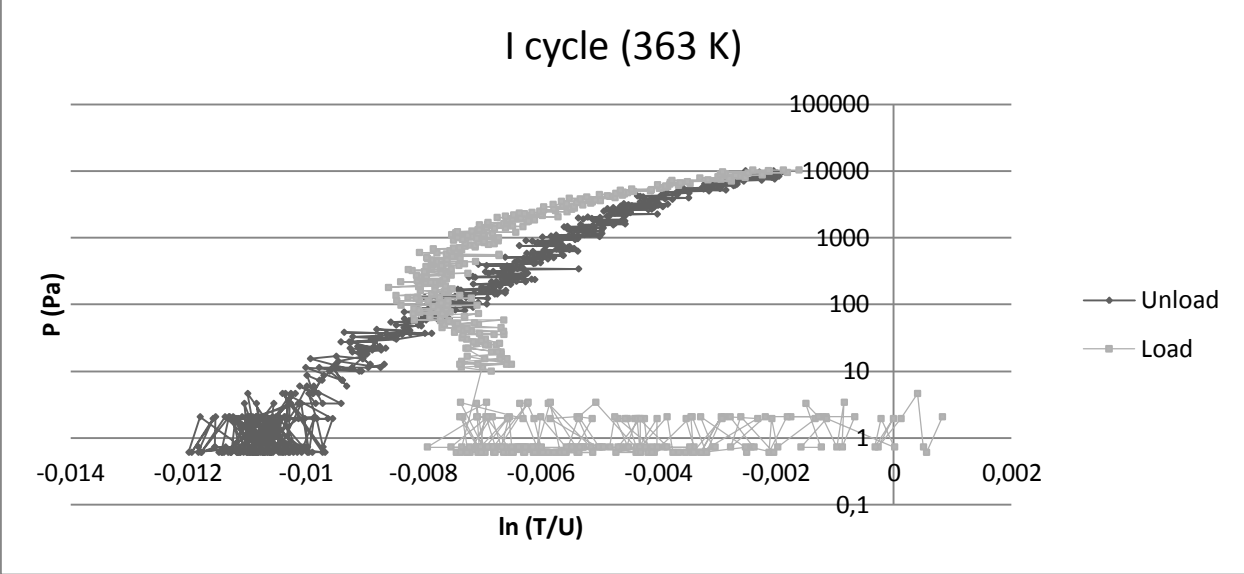
$$\Delta H = -(37 \pm 2) \frac{kJ}{mol}$$

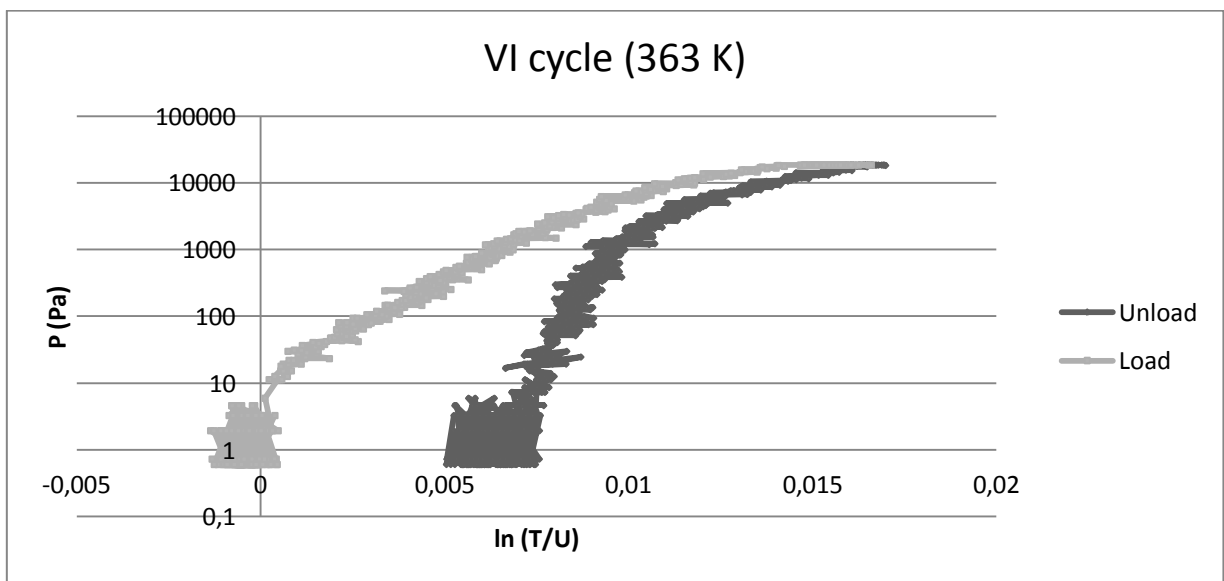
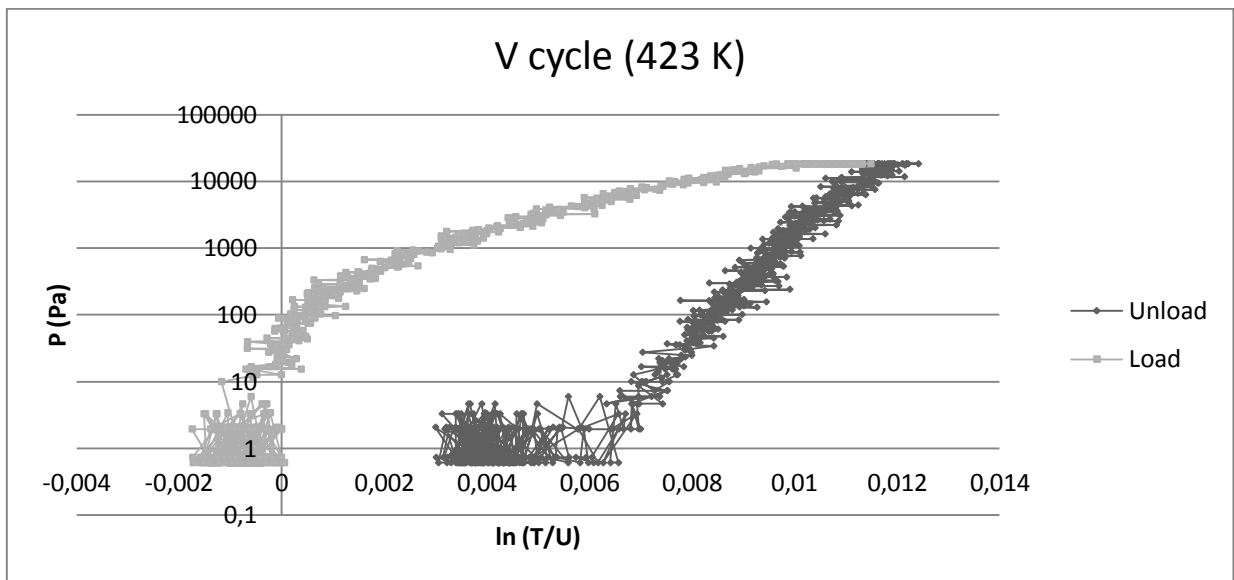
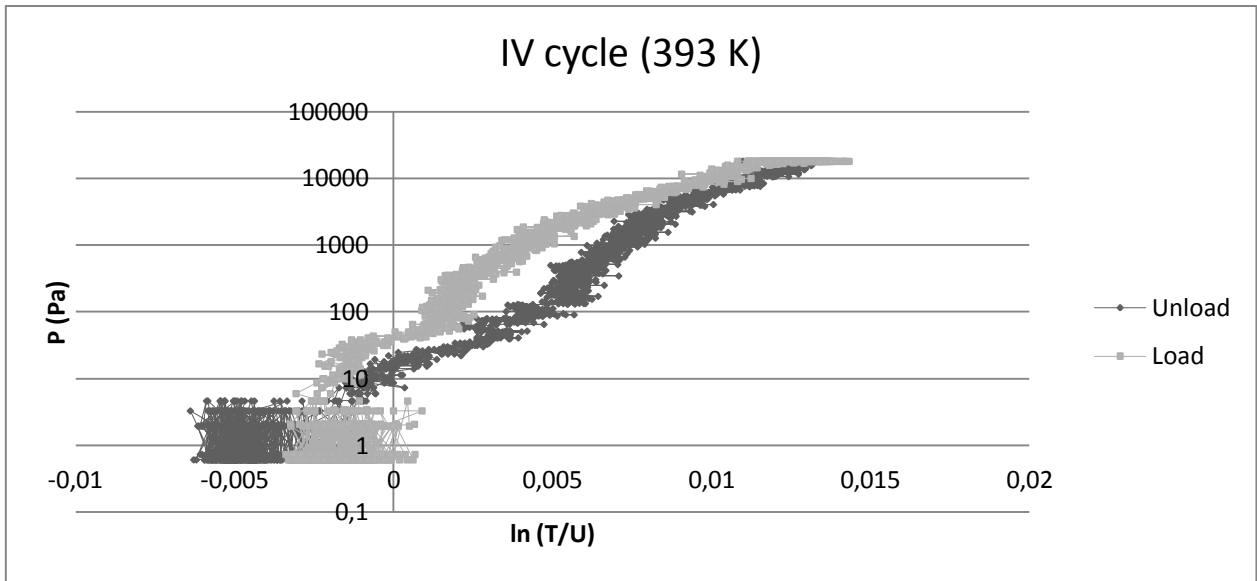
$$\Delta S = (64 \pm 3) \frac{J}{K mol}$$

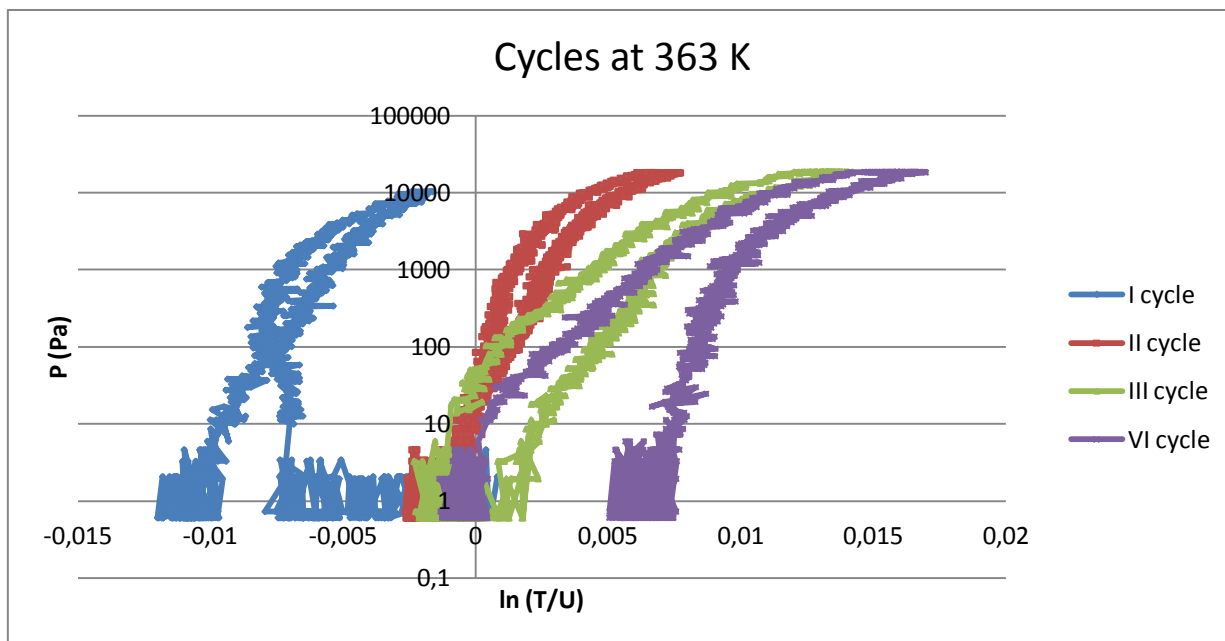
The smaller values of $\ln\left(\frac{T}{Y}\right)$ and formation enthalpy in comparison to the MgPd_101 2 minutes ones are caused by the different nanoparticles number and size. This parameter makes the values of equilibrium pressure higher than in the previously mentioned sample.

MgOPd_100 2 minutes

This sample underwent six measurements: the first three and the last at 363 K, the fourth at 393 K and the fifth at 423 K.



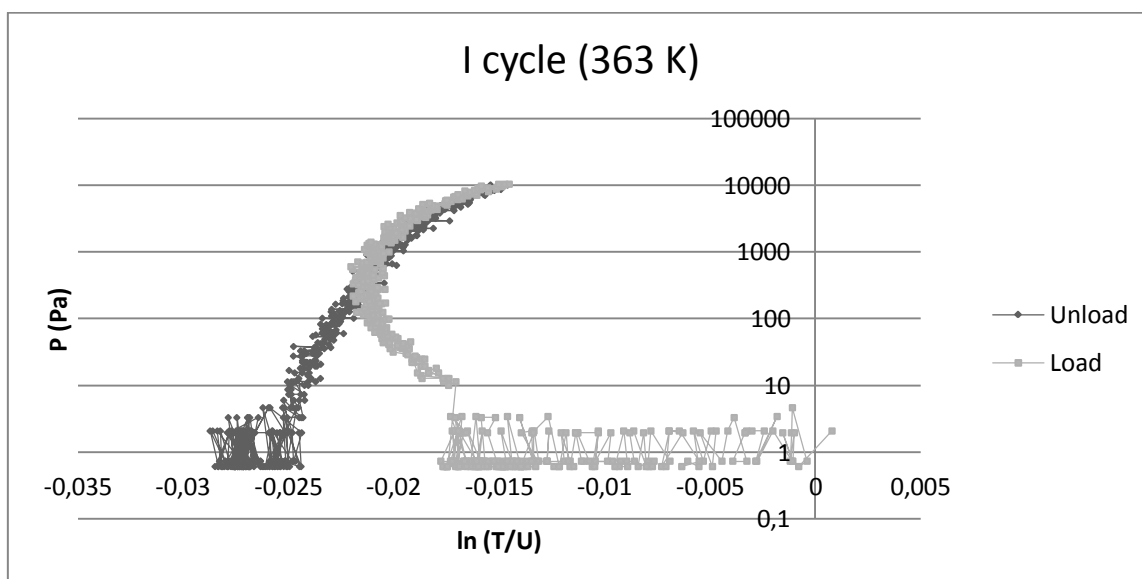


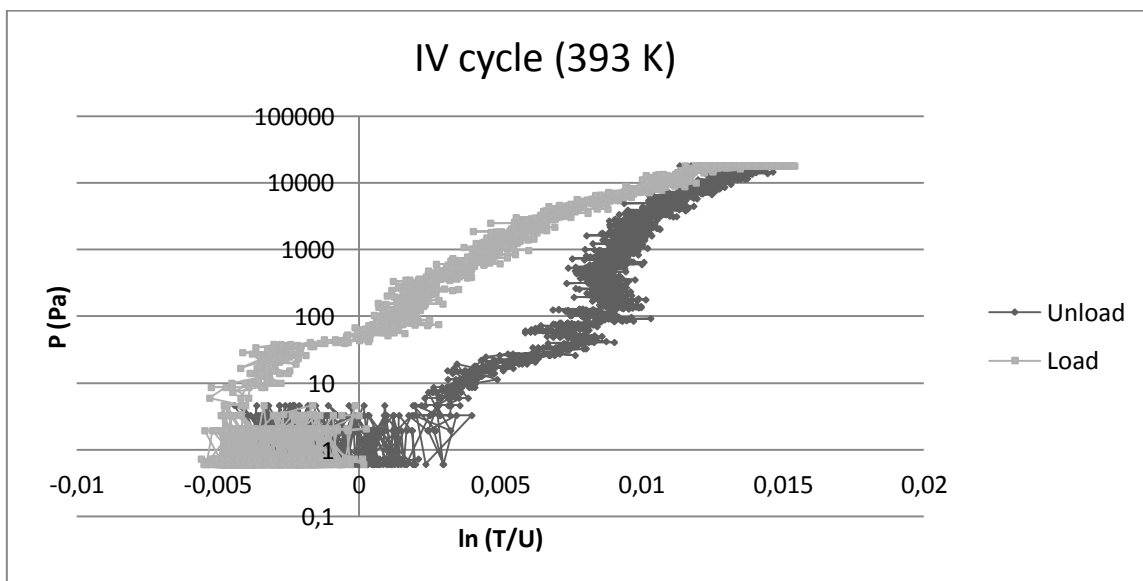
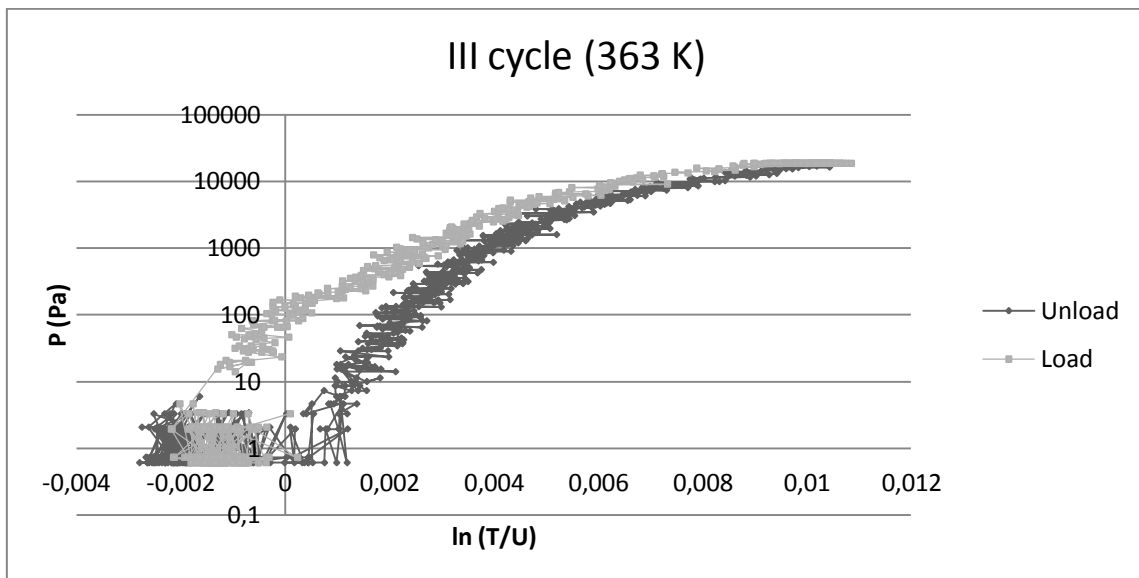
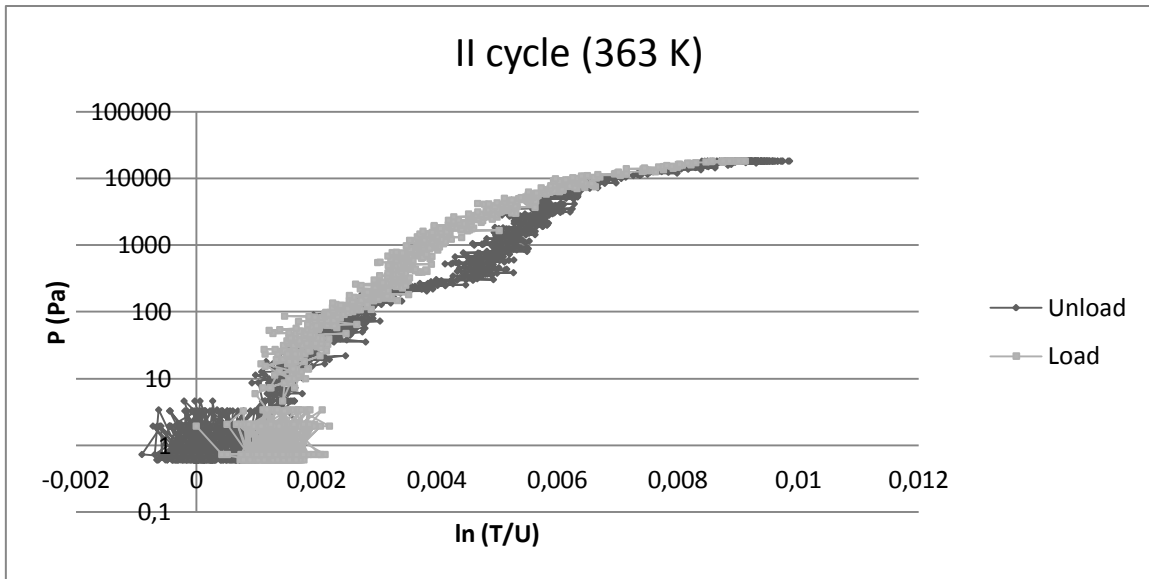


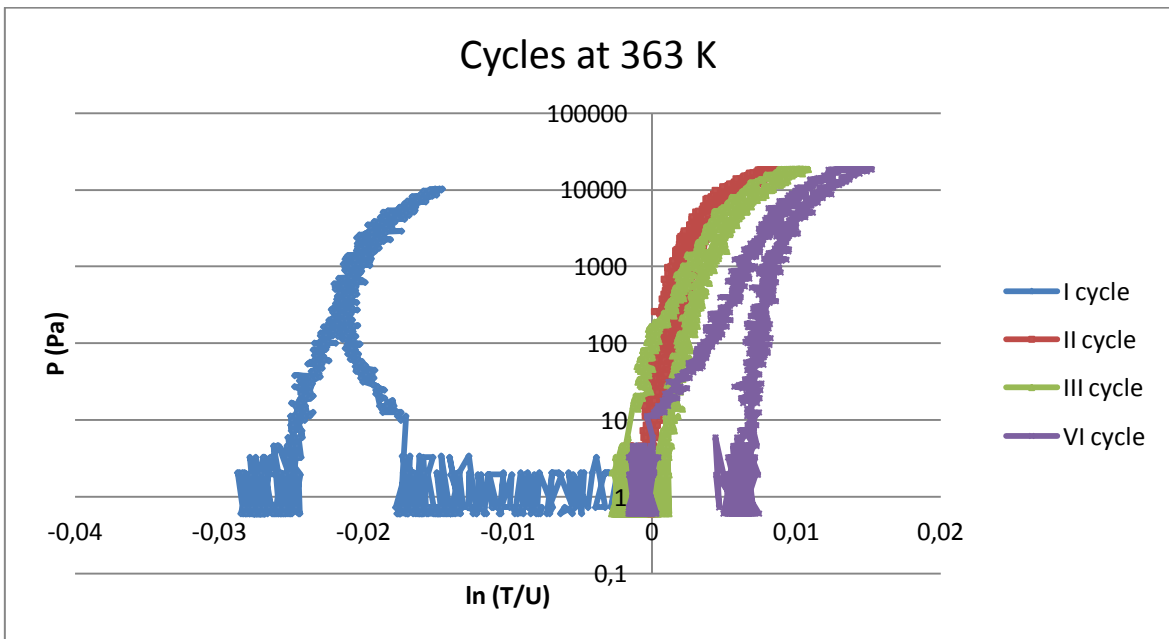
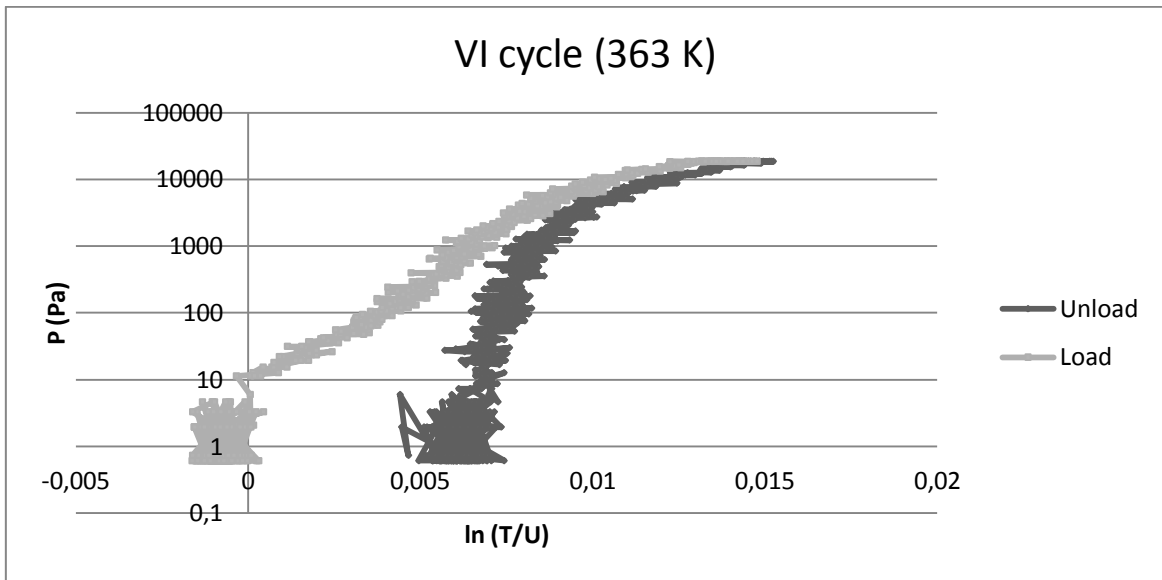
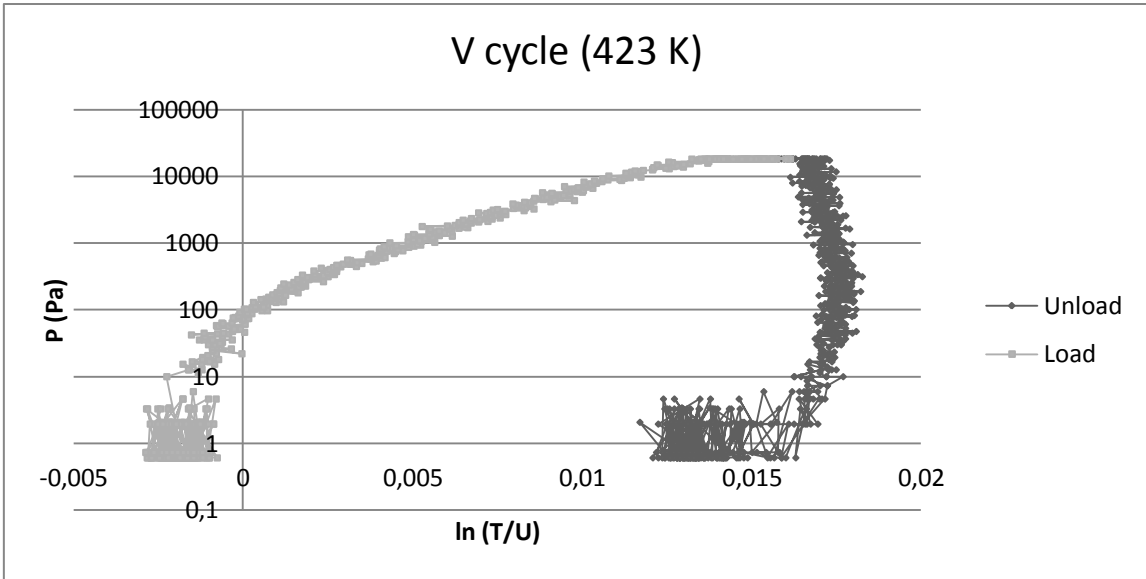
This sample shows a different behaviour respect to MgOPd_99 2 minutes: cycles are clearer and it is possible and it seems that hydrogen entering and exit is almost reversible, as if it is not stored by the metallic core.

MgOPd_100 1 minute

The sample was subjected to the same cycles as the previous one.



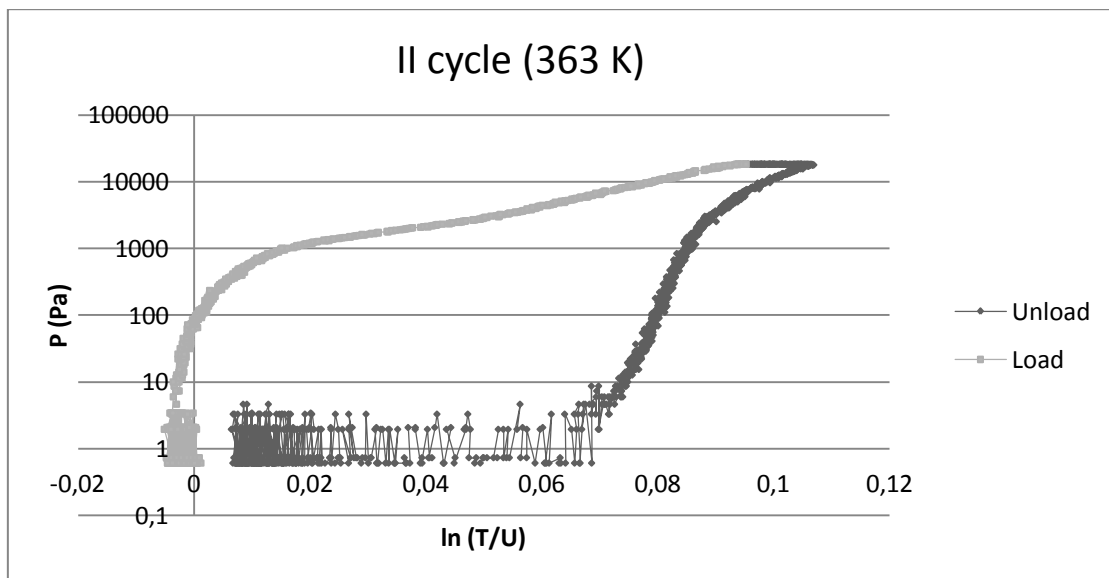
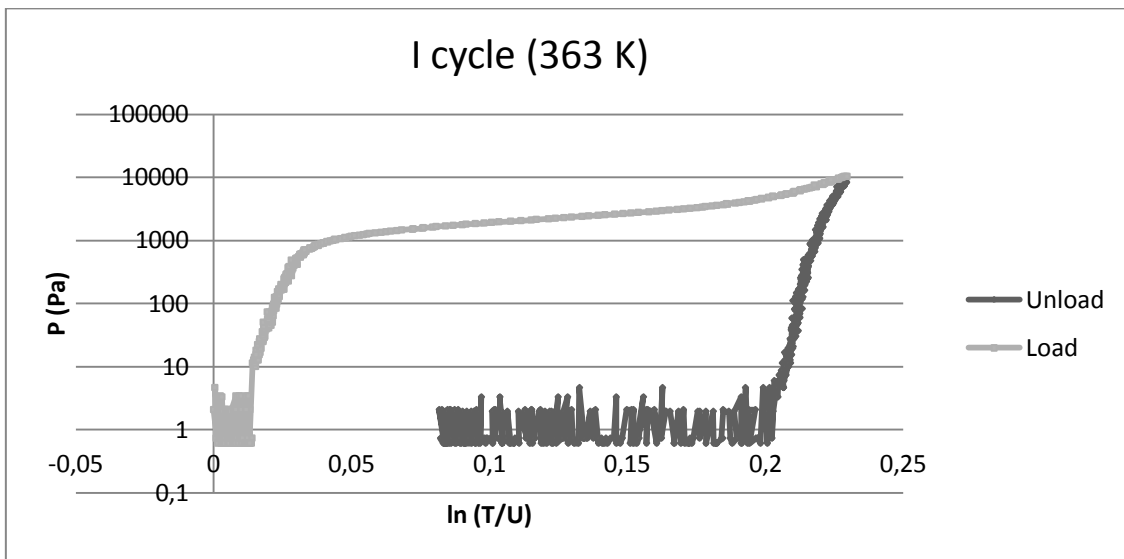


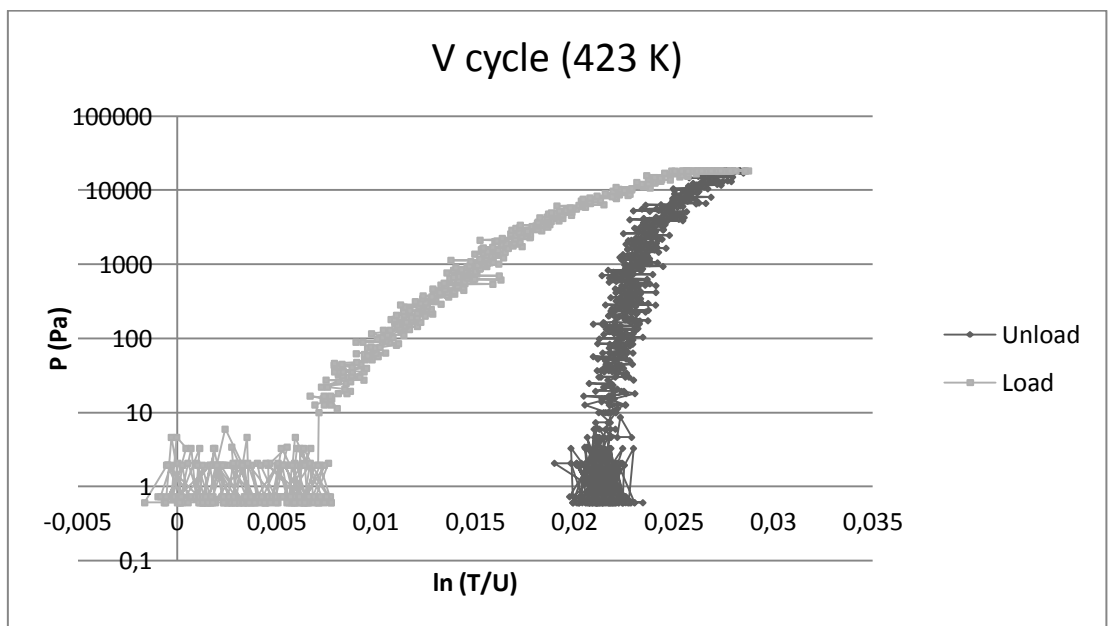
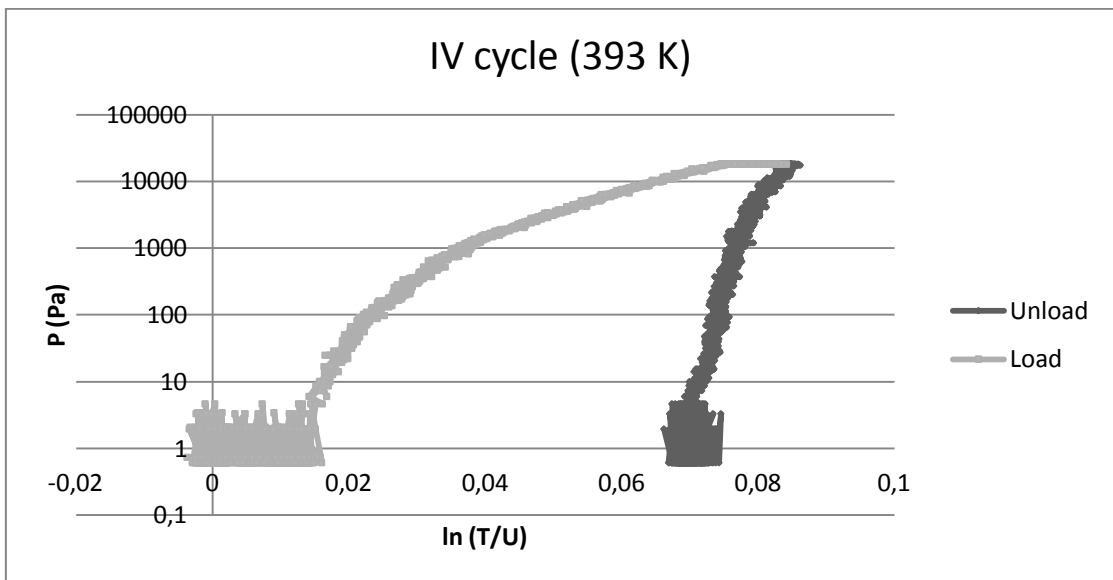
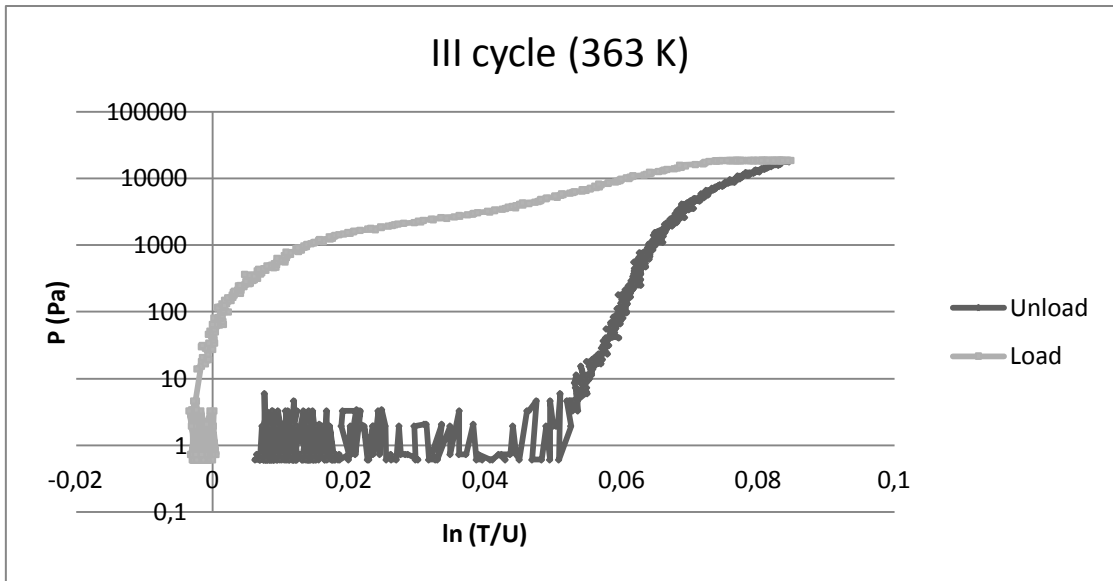


This sample had a behaviour very similar to the previous one, even if hysteresis shapes seem to be narrower.

MgPd₅₁

The sample underwent the same cycles as the previous one.





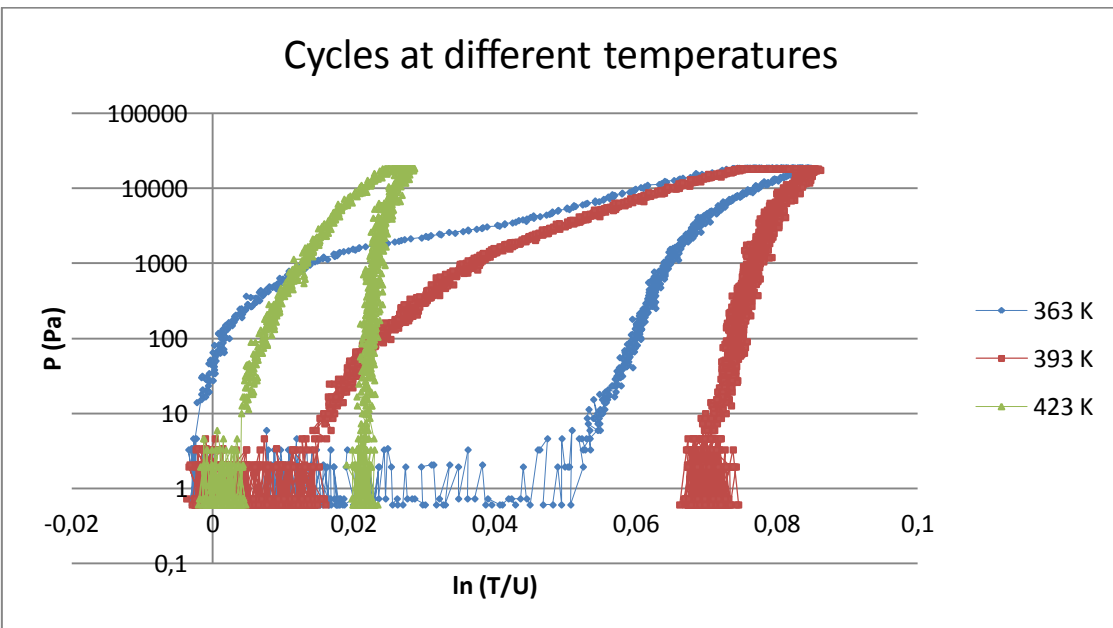
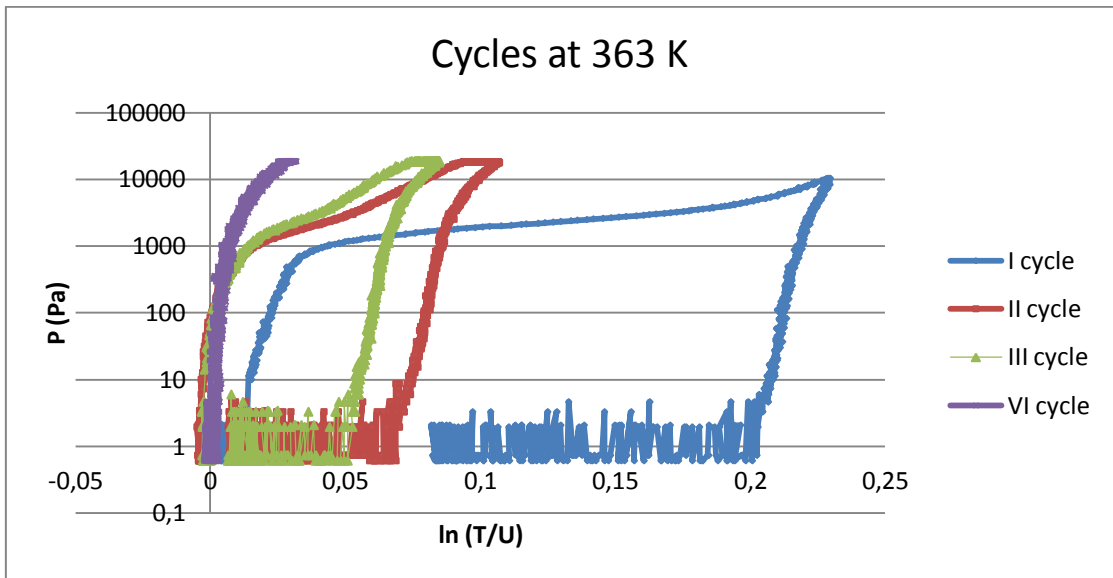
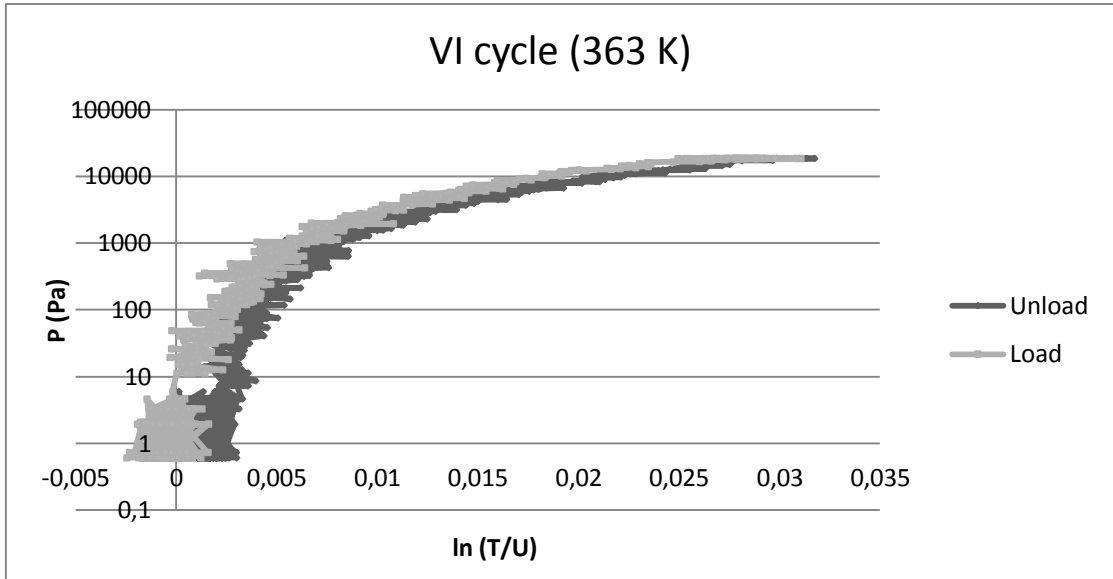


Table 12

P_{eq} (Pa)	T (K)
1670	363
5298	393
--	423

This sample shows clear plateaus even if a certain quality degradation can be observed. Anyway it is possible to draw an Arrhenius plot (Figure 10-7) and to derivate from it the values of formation enthalpy and entropy.

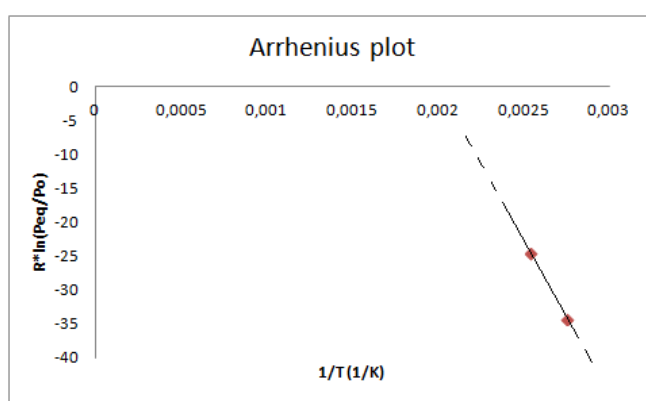


Figure 10-7

$$\Delta H = -(46 \pm 2) \frac{kJ}{mol}$$

$$\Delta S = (92 \pm 3) \frac{J}{K mol}$$

The luminous intensity behaviour was studied for this sample too: it results to be very similar to the one of MgPd 101 2 minutes. The first cycle was not considered also in this case because of its very high initial and final intensity values.

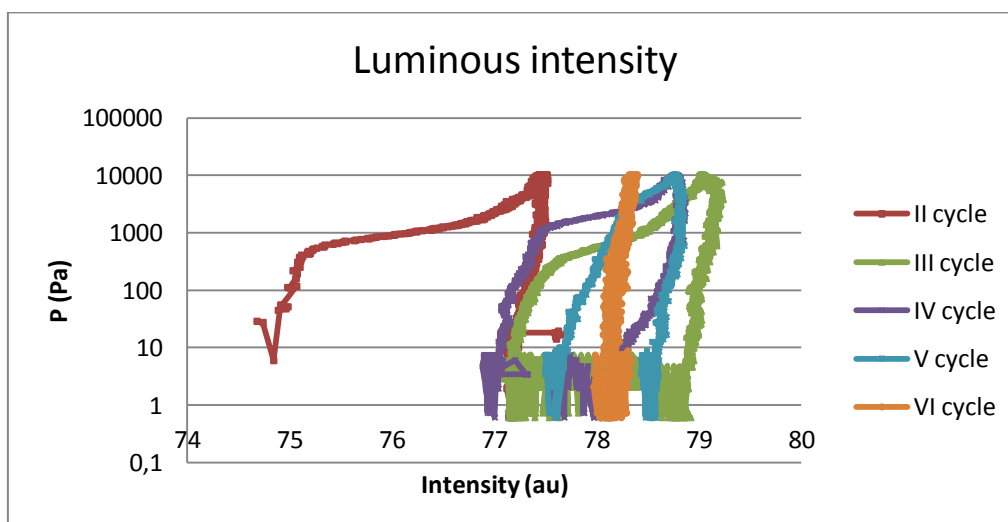


Table 13

Cycle	Average of the first five RAW data (au)	Average of the last five RAW data (au)
II	74,83	77,62
III	77,66	77,28
IV	77,25	77,59
V	77,55	78,49
VI	78,18	78,06

CHAPTER XI. Conclusions

The results showed in this work are contrasting: while the behaviour of MgPd samples and the achievement of the formation of composited structure nanoparticles with a metallic core and an oxide shell can be considered as positive, the behaviour of MgOPd samples represents a substantial failure.

The differences inside each group of samples can be addressed to the deposition time: samples with clearer graphs and higher changes in transmission are the ones with more material.

MgOPd samples did not work properly: no plateaus appeared and changes in optical transmission are very small: this indicates that hydride formation does not take place.

Palladium presence cannot be considered as a cause of the limited gas entering, as much literature says. Moreover, if it had been the limiting diffusion factor, both the kind of samples would have had the same behaviour.

These consideration let think that what create differences is the amount of MgO in the nanoparticles: MgPd surely have an oxidized layer too [30], but its thickness (around 4-5 nm) does not stop the gas entering significantly. Trying to understand better this point, some calculations were performed, taking as reference a periodic density functional theory (DFT) study [39]. According to this model there are some energetic barriers that molecular hydrogen must overcome to diffuse in the material: one relative to molecular dissociation (2.2 eV), one for the H atom passage from the surface to the first atomic plane (1,52 eV), one from the first atomic plane to the second one (1,2 eV) and, then, inside the bulk (1,02 eV). Considering just atomic diffusion, remembering that palladium favors molecular dissociation, there are astonishing differences between the various processes (Table 14). As it can be easily grasped, temperature is a critical parameter.

Being d the interplanar distance, D the diffusion coefficient, D_0 its pre-exponential value estimated for temperatures lower than 1173 K ($150 \text{ cm}^2/\text{s}$), E the energetic barrier, k the Boltzmann constant, τ the typical diffusion time and T the temperature, it is possible to write:

$$D = D_0 e^{-\frac{E}{kT}}$$

$$\tau = \frac{d^2}{2D}$$

Table 14

Diffusion process	T=363 K	T=393 K	T=423 K
From surface to 1 st plane	$\tau=3130$ s	$\tau=77$ s	$\tau=3,2$ s
From 1 st plane to 2 nd plane	$\tau=1,4 \cdot 10^{-1}$ s	$\tau=6,1 \cdot 10^{-3}$ s	$\tau=4,9 \cdot 10^{-4}$ s
Bulk	$\tau=3,6 \cdot 10^{-4}$ s	$\tau=3,0 \cdot 10^{-5}$ s	$\tau=3,6 \cdot 10^{-6}$ s

These calculations demonstrate what is commonly believed about oxidized layers: they inhibit hydrogen diffusion. Even if the most difficult passage is from the surface to the first atomic layer, a phenomenon common to both MgPd and MgOPd samples, it is clear from experiments that the MgO thickness is the most relevant parameter, keeping in mind that the energetic barrier in bulk magnesium is just 0,22 eV [40].

XRD analysis showed that the value of oxygen flux inserted during the evaporation is a critical point to determine the nanoparticles structure. While a flux of $1.25 \cdot 10^{-4}$ torr/s creates a MgO shell whose thickness is about the 32% of the whole radius, increasing it to $2 \cdot 10^{-4}$ torr/s increases this value up to the 64%. Moreover, it is impossible to determine if this relation is something like linear, exponential or whatever. For this reason, even if the flux values of the samples created are more similar to the one of MgOPd_95, even a small deviation from this value determine a great change in MgO thickness. This point is central to try to explain the differences between MgOPd_99 and MgOPd_100: these ones show clearer graphs and higher values of optical transmittance change.

MgOPd_100 samples were prepared with a lower value of oxygen flux in comparison of the MgOPd_99 ones and the data of the microbalance show that the amount of material is larger.

As regards MgPd samples, the results, even if globally positive, display some points of discussion. The presence of clear and complete plateaus in the absorption branch, except for MgPd_101 1 minute and MgPd_51 up at 423 K, corresponds to what was expected and made the estimate of the formation enthalpy possible. Being more rigorous, the equilibrium pressure should be calculated as the geometrical average by the first inflection points of the absorption and desorption branches. Anyway, the lack of a clear desorption plateau only allows the calculations based only on the absorption equilibrium pressure. These should be considered just estimates due to the fact that the method is graphic and that two samples have just two points in the Arrhenius plot. Moreover, the entropies values are of about a order of magnitude lower than values corresponding to the entropy of a gas mole. In any case, it is significant that MgPd_101 1 minute, the sample with the smallest nanoparticles, has the lowest value of formation enthalpy. Finally, in all the samples this value is sharply different from the bulk value, showing the validity of the destabilization model.

The lack of desorption branches is the main problem showed by these samples for various reasons. Firstly, as mentioned before, it makes impossible to determine the formation enthalpy using the real equilibrium pressure. Secondly, it means that the samples take too much time to release hydrogen and it is a critical limit for practical applications. Then, it is linked to and explains the continue reduction of the cycles width. The causes of this phenomenon could be the progressive thickening of the MgO shell that makes the sample more and more transparent cycle after cycle, or the presence of accumulating hydrogen which remains inside the nanoparticles due to the partial desorption. It cannot be excluded that both processes take place. Anyway, these two explanations collide with the fact that both would have caused a continue growth of the equilibrium pressure of the absorption branch, a phenomenon that is not clearly observed. Working at high temperatures makes possible the formation of an alloy between magnesium and palladium: it would limit the gas diffusion.

The fact that the samples do not react after high temperatures treatments can be linked to their almost complete oxidation or to morphological changes. Unfortunately, checking this hypothesis by SEM has been made impossible by the charge effect. A XRD measurement try was also performed, but no information was obtained due to the too low material amount present on the glass.

A sample that did not suffer from these problems and that was analyzed by hydrogenography was made up of nanodots with 30 nm of Mg, 5 nm of Ti and 5 nm of Pd. This sample was grown at KIT (Karlsruher Institut für Technologie) using molecular beam epitaxy (MBE): an alumina mask was deposited on the substrate, the materials deposited and the mask finally removed, as described by Figure 11-1.

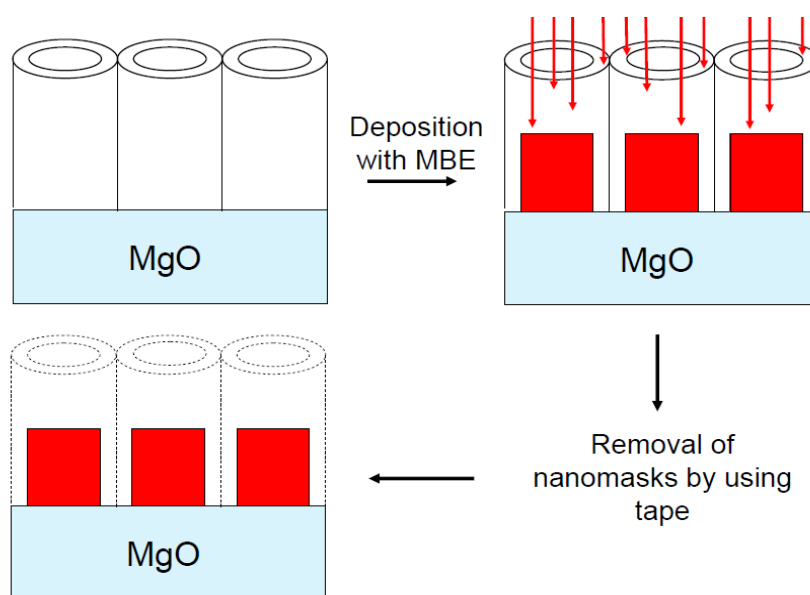


Figure 11-1

SEM images of the sample with (Figure 11-2) the alumina mask and of the mask itself (Figure 11-3).

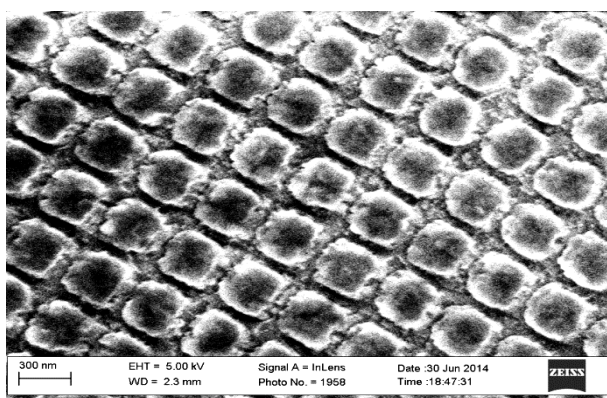


Figure 11-2

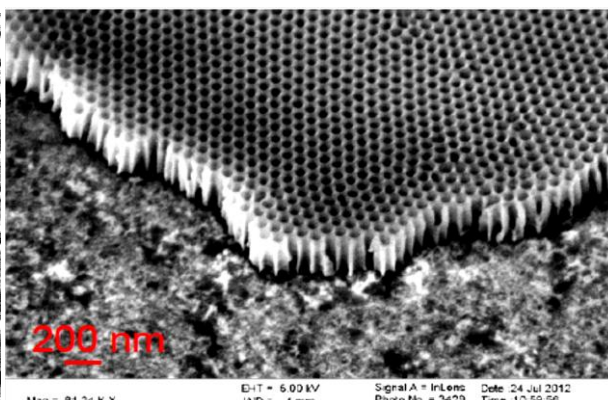
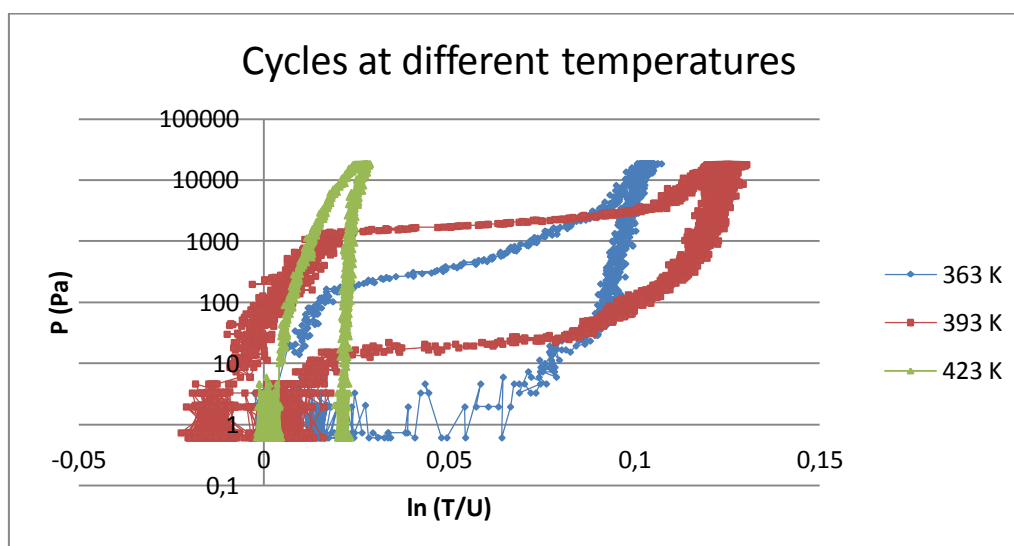


Figure 11-3



In this case the values of enthalpy and entropy calculated by the two different methods are very similar.

The rigorous method gives

$$\Delta H = -(81 \pm 4) \frac{kJ}{mol}$$

$$\Delta S = (157 \pm 8) \frac{J}{K mol}$$

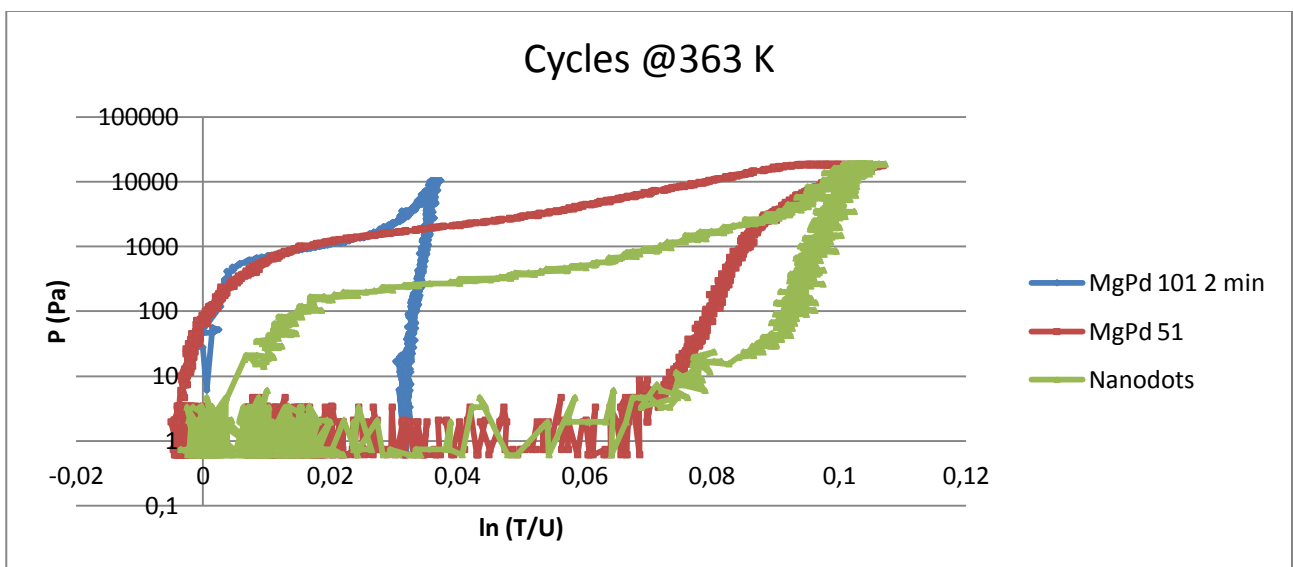
While using just the absorption branch:

$$\Delta H = -(77 \pm 4) \frac{kJ}{mol}$$

$$\Delta S = (163 \pm 8) \frac{J}{K mol}$$

These values are compatible to the ones of bulk magnesium within the errors. The entropy of formation absolute module is higher than for bulk material ($130 J/(K mol)$).

An interesting thing is the comparison between the samples showing plateaus. The sample produced at KIT and MgPd 51 show high $\ln\left(\frac{T}{U}\right)$ values, since transmittance logarithm, according to Lambert-Beer's law, is directly proportional to the material thickness: the nanodots analyzed and MgPd 51 nanoparticles are "big" ones and in both samples the material amount is relatively large. MgPd 101 2 minutes has lower $\ln\left(\frac{T}{U}\right)$ values due to the low quantity of magnesium deposited on the substrate. The most significant information coming from the graph below is the different hysteresis shape and extent on the y-axis. The sample with nanodots is the closer to the ideal case and to the bulk: their large size and the lack of an oxidized layer between magnesium and palladium which would have limited the metal expansion (MBE was performed in ultra-high vacuum conditions) are the reasons of this statement. On the contrary, the nanoparticles synthesized in Bologna surely have an oxidized layer around them, even if it is thinner than in MgOPd samples. This fact, as mentioned before, limits the metal expansion as the gas enters. Probably the core enlarge its volume so that the MgO shell undergoes plastic deformations that make the equilibrium pressure of the absorption branch higher and the one of the desorption branch lower.



These points of discussion stress the good and the bad points of the created samples. MgOPd samples are undoubtedly useless for hydrogen storage, mainly due to the too thick oxidized shell, but their synthesis is one of the most exciting results of this work. Having the experimental setup described before, it proved to be very hard to create nanoparticles with the core-shell structure: it took months of attempts, checks and failures. Anyway, the XRD and TEM analysis proved that this ambitious goal was achieved. MgPd samples worked properly, showing absorption plateaus in one case even at 423 K (MgPd 101 2 minutes). The formation enthalpy estimates, even if the calculations are rough, are lower than the bulk value, considering

the absolute module, verifying the destabilization model. Another positive result is the creation of "pure" magnesium nanoparticles with very small sizes (MgPd 101) respect to the typical hexagonal disks (MgPd 51), a goal achieved changing the kind of glass used as substrate. This point underlines the substrate role in the particles growth and it could be studied in a more rigorous and systematic way in the future. Anyway, an evident limit to the application of this kind of samples for hydrogen storage is represented by desorption, a too slow phenomenon that takes place at too low pressures. Moreover, the limited desorption after a cycle or the progressive oxidization cycle after cycle, reduce the transmittance variation after each hydrogenography measurement, i.e. the amount of entering gas. It would be very useful performing morphological and structural analysis of the samples after a cycle, after more cycles at the same temperature and, finally, after the temperature rise. It is evident that all the samples, after the measurement at 423 K, appear exhaust. Discovering how the sample evolves during hydrogenography would give crucial data to clear these problems.

In conclusion, even if this work did not find something that can bring to a large scale use of magnesium based nanoparticles for hydrogen storage, it represent a step which deserves further investigations towards the final goal of developing efficient light hydrogen storage materials.

References

- [1] U. S. E. I. Administration, «www.eia.gov,» 2010. [Online].
- [2] U. S. D. o. E. National Hydrogen Association, «The Hystory of Hydrogen,» 2010.
- [3] A. Evers, «www.hydrogenambassadors.com/background/worldwide-hydrogen-production-analysis.php,» December 2008. [Online].
- [4] U. o. Leeds, «http://reporter.leeds.ac.uk/press_releases/current/biodisel.htm,» November 2007. [Online].
- [5] Bellona, «www.interstatetravellers.us/Reference-Bibliography/Bellona-HydrogenReport.html,» July 2010. [Online].
- [6] B. Kruse, S. Grinna e C. Butc, «Hydrogen: status og muligneter,» Bellona, 2002.
- [7] W. Ayers, «Photolytic Production of Hydrogen». United States Brevetto 4466869, 1983.
- [8] F. S. e. al., «Chemical and Physical Solution for Hydrogen Storage,» *Argew. Chem. Int.*, pp. 6608 - 6630, 2009.
- [9] Renewableenergyworld.com, «www.renewableenergyworld.com/rea/news/article/2007/06/first-danish-hydrogen-plant-is-operational-48873,» June 2007. [Online].
- [10] S. a. Prewitt, «Effective ionic radii in oxides and fluorides,» *Acta Crystallographica*, vol. B, n. 25, pp. 925-946, 1969.
- [11] [Online]. Available: <http://en.wikipedia.org/wiki/Tritium>, <http://en.wikipedia.org/wiki/Deuterium> and <http://en.wikipedia.org/wiki/Hydrogen>.
- [12] H. a. London, «Wechselwirkung neutraler Atome und homöopolare Bindung nach der Quantenmechanik,» *Zeitschrift für Physik*, n. 44, pp. 455-472, 1927.
- [13] [Online]. Available: <http://encyclopedia.airliquide.com/Encyclopedia.asp?GasID=36>.
- [14] [Online]. Available: <http://www.gly.uga.edu/railsback/Fundamentals/ElementalAbundanceTableP.pdf>.
- [15] [Online]. Available: <http://en.wikipedia.org/wiki/Magnesium>.
- [16] A. R. O. a. A. O. L. Q. Zhu, «Novel stable compounds in the Mg–O system under,» *Physical Chemistry Chemical Physics*, vol. 15, pp. 7697-7700, 2013.
- [17] [Online]. Available: http://en.wikipedia.org/wiki/Magnesium_oxide.
- [18] M. W. George, «Platinum-group metals,» U.S. Geological Survey, 2007.

- [19] [Online]. Available: <http://en.wikipedia.org/wiki/Palladium>.
- [20] D. a. Meier, *Chemical Physics Letters*, vol. 160, n. 71, 1989.
- [21] J. C. a. J. Hillard, *Journal of Chemical Physics*, vol. 31, p. 688, 1959.
- [22] J. K. a. H. Weidersich, *J. Coll. Interface Sci*, vol. 61, p. 351, 1977.
- [23] H. S. a. H. Komiyama, «Migration-coalescence of nanoparticles during deposition of Au, Ag, Cu, and GaAs on amorphous SiO₂,» *Journal of Nanoparticle Research*, n. 1, p. 7–30, 1999..
- [24] D. McMullan, «SCANNING ELECTRON MICROSCOPY 1928 - 1965,» Cincinnati, 1993.
- [25] E. Ruska, The Early Development of Electron Lenses and Electron Microscopy.
- [26] C. e. al., «A Simple Scanning Electron Microscope,» *Rev. Sci. Inst.*, vol. 40, n. 2, p. 241–246, 1969.
- [27] J. C. Meyer, C. O. Girit, M. F. Crommie e A. Zettl, «Imaging and dynamics of light atoms and molecules on graphene,» *Nature*, vol. 454, n. 7202, p. 319–322, 2008.
- [28] C. Kittel, *Introduzione alla fisica dello stato solido*, CEA, 2008.
- [29] «The MAUD program,» [Online]. Available: <http://www.ing.unitn.it/~maud/>.
- [30] M. C. S. B. P. L. P. F. Venturi, «Self-assembly of gas-phase synthesized Magnesium nanoparticles on room temperature substrates,» *Nanotechnology*.
- [31] J. Y. J. S. a. X. D. K. Niu, «One-step synthesis of MgO hollow nanospheres with blue emission,» *Nanotechnology*, 5 July 2010.
- [32] A. D. S. a. E. O. Kirkendall, *Trans. AIME*, vol. 171, p. 130, 1947.
- [33] G. B. Gibbs, *Oxid. Met.*, vol. 16, p. 147, 1981.
- [34] Y. Yin, «Formation of Hollow Nanocrystals Through the Nanoscale Kirkendall Effect,» *Science*, vol. 304, p. 711, 2004.
- [35] V. S. a. W. Wallace, «The hyperstoichiometric ZrMn_{1+x}Fe_{1+y}-H₂ system II: Hysteresis effect,» *Journal of the Less Common Metals*, vol. 91, p. 239–249, 1983.
- [36] R. S. a. A. Khachaturyanb, «Thermodynamics of open two-phase systems with coherent interfaces: Application to metal–hydrogen systems,» *Acta Materialia*, vol. 54, p. 313–323, 2006.
- [37] T. B. F. a. J. Clewley, «Hysteresis in metal hydrides,» *Journal of the Less Common Metals*, vol. 83, p. 127–141, 1982.
- [38] H. K. B. a. P. Peguin, «A Theory of the Hysteretic Contribution to Internal Friction; Thermomechanical Unpinning of Dislocations,» *Journal of Applied Physics*, vol. 39, p. 4428, 1968.

- [39] J. Z. Y. W. Q. L. K. C. X. B. G. Wua, «Adsorption and dissociation of hydrogen on MgO surface: A first-principles study,» *Journal of Alloys and Compounds*, vol. 490, pp. 788-793, 2009.
- [40] [Online]. Available: <http://theochem.org/bragasetur/papers/MgH.pdf>.
- [42] [Online]. Available: <http://en.wikipedia.org/wiki/Magnesium>.
- [43] [Online]. Available: <http://en.wikipedia.org/wiki/Magnesium>.
- [44] [Online]. Available: http://en.wikipedia.org/wiki/Magnesium_oxide.
- [45] [Online]. Available: <http://en.wikipedia.org/wiki/Palladium>.
- [46] V. S. a. W. Wallace, «The hyperstoichiometric $ZrMn_{1+x}Fe_{1+y}-H_2$ system II: Hysteresis effect,» *Journal of the Less Common Metals*, vol. 91, p. 239–249, 1983.

Acknowledgments

Firstly, I want to thank Prof. Luca Pasquini who gave me the opportunity to work on this interesting field, helping me with advices, attention and material to study. I cannot forget the contribution given to me scientifically and humanly by Dr. Marco Calizzi, who turned from a colleague to a friend. I also thank Maurizio for his companionship and all other people in Bologna Physics Department who made me happy to work in the laboratory.

I must also remind the people I met and I worked with in Delft, especially Prof. Bernard Dam. In the Netherlands I spent an interesting period of my life that I will always remember as a fundamental step for my human and professional growth.

I thank Alan Molinari and Prof. Dr. Ing. Horst Hahn of KIT – Universität des Landes Baden-Württemberg und nationales Großforschungszentrum in der Helmholtz-Gemeinschaft for the possibility of studying their nanodots.

I would like to remember Dr. Valentina Bello and Prof. Giovanni Mattei for the very useful TEM analysis.

Then I hug and thank all my family, starting from my parents Antonino and Lia, who have always supported me, not only financially, then my grandpa, my uncle, my aunt and my cousin Giovanna. Their love and care made the hardship of this experience easier.

I want to thank the friends that have been and will be next to me, without them I would have been a worse person but maybe a better scientist.

Thanks to the one who has made everything special.